

# The Dynamics of Viscous Fibers

**Satyananda Panda**

Vom Fachbereich Mathematik  
der Technischen Universität Kaiserslautern  
zur Verleihung des akademischen Grades  
Doktor der Naturwissenschaften  
(Doctor rerum naturalium, Dr. rer. nat.)  
genehmigte Dissertation

Referent: Prof. Dr. Axel Klar  
Koreferent: Prof. Dr. Andreas Unterreiter

Tag der Disputation: 21.03.2006

D 386

## Acknowledgments

I would like to express my sincere gratitude to Prof. Dr. Axel Klar for his support, guidance and encouragement. I am highly indebted to Prof. em. Dr. Helmut Neunzert for giving me the opportunity of doing my Ph.D. in Kaiserslautern. I extend my thanks to Prof. Dr. Andreas Unterreiter for being my co-referee.

I am very grateful to Dr. Raimund Wegener for his interest in my work, continuous support and many helpful and valuable discussions. I am particularly indebted to Dr. Thomas Götz for the useful hints and advises for the overall presentation of this thesis. I would like to express my sincere appreciation to Dr. Robert Feßler for introducing me into the topic of viscous fibers. Moreover, I am grateful to Dr. Dietmar Hietel for fruitful discussions about my numerical studies. Dr. Nicole Marheineke has been a friend great to work with, who generously helped in reading the manuscript. Special thanks go to Dr. Sudarshan Tiwari, Aleksander Grm and Steffen Blomeier for their friendship, understanding and encouragement.

This research project was financially supported by Fraunhofer ITWM, Department Transport Processes. This scholarship gave the work a very practical direction, that I believe is beneficial.

Both staff and students within the Department of Mathematics at the Technical University of Kaiserslautern and the Department Transport Processes at the Fraunhofer ITWM provided a friendly and supportive environment. Especially, I would like to mention Dr. Falk Tribsch whose always cheerfully given help with administrative matters I appreciated very much.

Finally, I would like to acknowledge the support and love of my family. The encouragement and understanding of my parents has been crucial for the completion of my Ph.D. My wife Snigdha deserves my deepest thanks, for all she has done for me during these years.

# Contents

<b>1</b>	<b>Introduction</b>	<b>1</b>
1.1	Problem description . . . . .	1
1.2	Literature review and objectives . . . . .	3
1.3	Outline of the thesis . . . . .	4
<b>2</b>	<b>Mathematical Modeling</b>	<b>7</b>
2.1	Introduction . . . . .	7
2.2	Fiber spinning: Free boundary value problem . . . . .	8
2.3	Non-dimensionalization . . . . .	10
2.3.1	Scaling . . . . .	10
2.3.2	Model equations in non-dimensional form . . . . .	11
2.3.3	Identification of a small parameter . . . . .	12
2.4	Model equations in general coordinates . . . . .	12
2.4.1	Concept . . . . .	12
2.4.2	Transformation of observables . . . . .	13
2.4.3	Transformation of the geometry . . . . .	15
2.4.4	Transformation of the free boundary value problem . . . . .	15
2.5	Scaled curvilinear coordinates . . . . .	18
2.5.1	Concept . . . . .	18
2.5.2	Fiber problem: Scaled curvilinear coordinate system . . . . .	20
2.5.3	Integration over cross-sections in curvilinear coordinates . . . . .	25

2.5.4	Integrated equations . . . . .	27
2.6	Asymptotic analysis . . . . .	27
2.6.1	Family of problems . . . . .	28
2.6.2	Asymptotic expansions . . . . .	29
2.6.3	Lateral problem . . . . .	32
2.6.4	Constraints, initial and boundary conditions . . . . .	35
2.7	Final asymptotic results . . . . .	37
2.7.1	Asymptotic model equations in dimensional form . . . . .	38
<b>3</b>	<b>Numerical Simulation of the Unsteady Fiber Model</b>	<b>41</b>
3.1	Asymptotic fiber model . . . . .	41
3.2	Straight fiber (Special case) . . . . .	43
3.2.1	Numerical scheme for the straight fiber problem . . . . .	45
3.2.2	Simulation results and discussion . . . . .	51
3.2.3	Industrial application of the straight fiber model . . . . .	54
3.2.4	Convergence tests . . . . .	56
3.3	Curved fiber (2D center-line) . . . . .	58
3.3.1	Numerical scheme for the curved fiber . . . . .	58
3.3.2	Validation of the numerical scheme . . . . .	63
3.3.3	Simulation results and discussion . . . . .	67
3.4	Curved fiber (3D center-line) . . . . .	70
3.4.1	Simulation results and discussion . . . . .	71
3.5	Summary . . . . .	72
<b>4</b>	<b>Numerical Simulation of the Steady State Fiber Model</b>	<b>73</b>
4.1	Steady state fiber model . . . . .	74
4.2	Numerical procedure . . . . .	75
4.2.1	Comparison of the simulation results . . . . .	78
4.3	Projection approach . . . . .	81
4.4	Summary . . . . .	83

---

<b>5</b>	<b>Application</b>	<b>85</b>
5.1	Introduction . . . . .	85
5.2	Industrial data . . . . .	86
5.3	Simulation results . . . . .	87
<b>6</b>	<b>Conclusions</b>	<b>91</b>
	<b>Appendix</b>	<b>93</b>
	<b>Bibliography</b>	<b>95</b>



# Chapter 1

## Introduction

### 1.1 Problem description

The present thesis aims to study the industrial process of glass wools and glass fibers. Glass wool that is produced by a centrifugal spinning process is mostly used for the thermal insulation in homes and buildings, and it is of increasing industrial importance. In the centrifugal spinning process, centrifugal forces press hot molten glass through small nozzles of a rapidly rotating cylindrical drum. Thereby thin fibers are formed that break into pieces due to the surrounding air streams. They are collected by gravity on a conveyor belt in the form of a web. A schematic drawing of the production process is given in Fig. 1.1, while Fig. 1.2 visualizes a real production facility. The centrifugal spinning is a complex process. A model that can accurately predict the shape and dynamics of the fibers using the internal variables like cross-sectional area and fluid velocity would be of considerable benefit to industry. In this thesis we do not study the complete production process. Instead we only focus on the first steps, during which the glass fibers emerge from the spinneret. Thus, we do not consider any subsequent breakings of the fibers when they are falling down to the conveyor belt.

One of the most obvious observations in this process is that the fiber geometry is slender, i.e. the ratio between radius and length is small. The geometry is not known in advance except that the fibers are curved due to rotational forces. We describe the fiber spinning process by three-dimensional free boundary value problem. The equations are the Navier-Stokes equations with free surface boundary conditions. These equations are difficult in general, but the slenderness of the fluid geometry enables the simplification of the full three-dimensional mathematical model by means of asymptotic analysis. Thereby, fiber dynamics can be predicted by a simple system of one-dimensional equations.

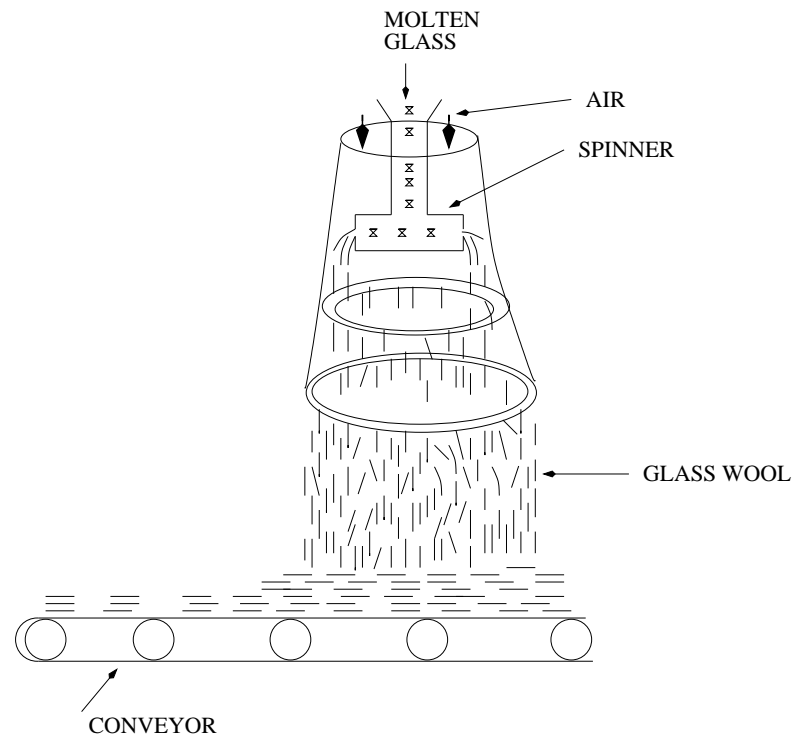


Figure 1.1: A schematic diagram of the centrifugal spinning process.



Figure 1.2: Glass wool production in a centrifugal spinning process.



## 1.2 Literature review and objectives

We begin by briefly reviewing some of the models and techniques that have been developed for related problems. There exists a large amount of literature on the flow of straight, slender viscous fibers, mostly devoted to the fiber draw-down process, the production of endless fibers. In this process nozzles are attached to a spinneret and mechanical drawing is used to form the fibers from the melt. Finally, the fibers solidify and are taken up by a winder. On the other hand, as described above, the glass wool is manufactured in a centrifugal process without the use of a nozzle extruder. However, the mathematical model concerning the manufacture of endless glass fibers and glass wool is belonging to the same class of motions which can be described as a uniaxial, extensional or elongational flow. The important differences in the production of fibers in the draw-down and centrifugal spinning process are the way in which the heat is applied in the spinneret and the boundary conditions at the end of the fiber.

Mathematical models of the draw-down flows are typically based on a quasi-one-dimensional approximation due to slenderness of the geometry. By assuming that diameter of the filament is small compared to its length, a one-dimensional approach can be directly used, e.g. [23, 32] for the modeling of the draw-down flow. There are two other possibilities for the construction of one-dimensional equations. They can either be derived from the assumption of a purely extensional flow, i.e. by means of a systematic asymptotic reduction of the underlying equations of motion and free surface conditions, or they can be derived systematically by the use of regular asymptotic expansions. Many authors, e.g. [2, 27] have derived 1D-approximations for the straight fiber from the uniaxial flow assumptions in the context of viscoelastic jets and fibers as well as for spinning a molten thread line. The construction of 1D-equations by using regular asymptotic expansions for the extension and twist of a viscous non-axisymmetric fiber can be found in [11]. The analysis in this work is restricted to viscous effects only. This work has later been generalized to include the effects of inertia, gravity [10] and surface tension [6]. There are numerous other research works on straight fibers in connection with stability and breakup. For this purpose we refer the reader to [19, 28] and a recent review [14].

Fewer papers also examine viscous fibers with a curved center-line. For example, the derivation of the one-dimensional model for the description of capillary and bending disturbances is given in [4, 5, 15]. Moreover, two-dimensional sheets with curved center-lines falling under gravity are studied in [12, 33], while an asymptotic derivation and its discussion for curved fibers in the context of a Stokes flow problem is addressed in [22]. Many recent studies have focused on the study of inviscid [7] and viscous [8] liquid jets created from a rotational orifice. In their study of the prilling process in the manufacture of fertilizers, one-dimensional model equations were derived from

the assumption that the flow is uniaxial and the center-line of the jet is steady at the leading order. Furthermore, a linear stability analysis of the derived inviscid model is performed in [35]. Considering a fiber of a fixed length in the framework of a steady-state solution, the evolution equations for cross-sectional area and velocity are studied in [8] with a time dependent boundary condition. Although this work is quite similar to our present problem, the investigation of the full evolution process of a viscous fiber emerging from a rotating device as a free boundary value problem is still open.

Thus, the main objective of this thesis is the derivation of an one-dimensional asymptotic model from the three-dimensional Navier-Stokes equations with free surface boundary conditions. Thereby, we follow the spirit of [10] and [11] for straight fibers and apply the concept of the regular asymptotic expansions on our curved liquid fiber with an unsteady center-line emerging from a rotating orifice. Additionally, we develop numerical schemes for the simulation of the steady and unsteady processes.

### 1.3 Outline of the thesis

In Chapter 2 we begin with the introduction of the fiber spinning process as a full three-dimensional boundary value problem. The model equations are the Navier-Stokes equations with free surface boundary conditions and the inflow condition. Taking into account that the curvature of the fiber is not small, the model equations are described in general coordinates. Scaled curvilinear coordinates with respect to the fiber center-line are introduced. The equations are then analyzed asymptotically and thereby an one-dimensional fiber model is derived.

The unsteady process of the derived asymptotic model is discussed in Chapter 3. We first develop a numerical scheme based on a finite volume method to analyze the unsteady case for a straight fiber, which is a special case of our problem. An industrial application of the model is also presented. The developed numerical scheme is then extended to the numerical simulation of the evolution of the fiber under the influence of rotational and gravitational forces. In particular, to validate the numerical simulation results, a comparison is made with analytical results in the inviscid limit.

In Chapter 4 we numerically analyze the steady-state fiber model. A numerical scheme based on the finite volume method is also developed to simulate the steady-state model. In particular, the simulation results of the unsteady and steady state problems are compared. Further, a projection approach is presented for suitable numerical solutions of the steady-state model equations by means of a finite difference method.

Then in Chapter 5, the derived asymptotic model, in particular its steady-state version, is used to predict the shape of the fiber center-line and its internal variables like cross-sectional area, fluid velocity and tension based on industrial data.

Finally, some conclusions from this work are given in Chapter 6. An outlook on possible extensions of this model is presented as subject of future work.



# Chapter 2

## Mathematical Modeling

### 2.1 Introduction

During the production process of glass wool, hot molten material from a furnace is transferred into a rotating device, and fibers are produced as centrifugal forces extrude the material through many small holes. Common observations in this process are:

- the fiber geometry is slender, i.e. the ratio between the typical thickness and the typical length is small,
- the free surface of the fiber is not known in advance,
- the fiber is curved due to the rotational forces.

We describe this process by a full three-dimensional free boundary value problem. For the mathematical model a single three-dimensional viscous isothermal fiber is investigated. We model the medium as an incompressible Newtonian fluid. We take gravity and rotational forces into account, but neglect all other forces such as surface tension and air resistance. Even when these assumptions are made, the equations for the free boundary value problem are difficult in general. But, the slenderness of the fluid geometry enables the simplification of the full three-dimensional mathematical model by means of asymptotic analysis. Thereby we predict the fiber dynamics with a simple and tractable system of equations. Thus, the primary aim of this chapter is to derive a one-dimensional asymptotic model from the three-dimensional theory.

A brief outline of this chapter is as follows. In Section 2.2 we introduce the full three-dimensional boundary value problem. The model equations are the Navier-Stokes equations with free surface boundary conditions and inflow condition. In Section 2.3 the non-dimensionalization procedure of the fiber problem is presented. Taking into

consideration that the curvature of the fiber can not be neglected, we describe the model equations in general coordinates in Section 2.4. Scaled curvilinear coordinates with respect to the fiber center-line are introduced in Section 2.5. In Section 2.6 we analyze the full three-dimensional model equations asymptotically and derive thereby the one-dimensional fiber model. Finally, we draw conclusions from the whole chapter in Section 2.7.

## 2.2 Fiber spinning: Free boundary value problem

In order to avoid the use of unnecessarily many symbols referring to the same object we denote the dimensional variables with superscript  $*$  and the dimensionless ones without. A brief overview of the various mathematical conventions used throughout this work is given in Appendix.

The free boundary value problem is described by the incompressible Navier-Stokes equations with free surface and inflow boundary conditions. Let  $\Omega^*(t^*) \subset \mathbb{R}^3$  be the domain of interest and  $\partial\Omega^*(t^*) = \Gamma_{fr}^*(t^*) \cup \Gamma_{in}^*$  with  $\Gamma_{fr}^*(t^*) \cap \Gamma_{in}^* = \emptyset$ . Here  $\Gamma_{fr}^*(t^*)$  and  $\Gamma_{in}^*$  are the free surface and the inflow boundary of the fiber, respectively. We initialize the process time at  $t^* = 0$ , i.e. throughout this work  $t^* \in \mathbb{R}^+$ . Then we have the following set of equations:

*Conservation of mass and momentum,  $\mathbf{r}^* \in \Omega^*(t^*)$*

$$\nabla \cdot \mathbf{v}^*(\mathbf{r}^*, t^*) = 0 \quad (2.1)$$

$$\rho(\partial_{t^*} \mathbf{v}^*(\mathbf{r}^*, t^*) + \nabla \cdot (\mathbf{v}^* \otimes \mathbf{v}^*)(\mathbf{r}^*, t^*)) = \nabla \cdot \mathbf{S}^{*T}(\mathbf{r}^*, t^*) + \mathbf{f}^*(\mathbf{r}^*, t^*) \quad (2.2)$$

*Constitutive law*

$$\mathbf{S}^* = -p^* \mathbf{I} + \mu(\nabla \mathbf{v}^* + (\nabla \mathbf{v}^*)^T) \quad (2.3)$$

*Kinematic and dynamic boundary conditions,  $\mathbf{r}^* \in \Gamma_{fr}^*(t^*)$*

$$(\mathbf{v}^* \cdot \mathbf{n}^*)(\mathbf{r}^*, t^*) = w^*(\mathbf{r}^*, t^*) \quad (2.4)$$

$$(\mathbf{S}^* \cdot \mathbf{n}^*)(\mathbf{r}^*, t^*) = \mathbf{0} \quad (2.5)$$

*Inflow boundary condition,  $\mathbf{r}^* \in \Gamma_{in}^*$*

$$\mathbf{v}^*(\mathbf{r}^*, t^*) = \mathbf{v}_{in}^*(\mathbf{r}^*) \quad (2.6)$$

*Initial condition*

$$\Omega^*(0) = \emptyset \quad (2.7)$$

The symbols  $\mathbf{v}^*$ ,  $\rho$  and  $\mathbf{S}^*$  denote the fluid velocity, the constant density and the stress tensor. Here,  $\mathbf{f}^*$  represents the body forces that contain the force of gravity and the rotational forces due to the rotation of the spinning device,  $p^*$  and  $\mu$  are the pressure and the coefficient of constant viscosity. The  $\mathbf{n}^*$  stands for the unit outward normal vector of the free surface and  $w^*$  is the speed of the free surface.

**Assumption 2.1** We assume that the inflow boundary  $\Gamma_{in}^*$  is a time-independent plane. In other words, we consider a planar cross-sectional shape of the nozzle.

**Remark 2.1** In order to simplify the following asymptotic analysis of the three-dimensional model in Eqs. (2.1)-(2.7), we have excluded surface tension. As a result we retain the homogenous dynamic boundary condition Eq. (2.5). To study the surface tension effect in the model, the boundary condition Eq. (2.5) can be modified in the following way

$$(\mathbf{S}^* \cdot \mathbf{n}^*)(\mathbf{r}^*, t^*) = -\sigma \varkappa \mathbf{n}^*(\mathbf{r}^*, t^*), \quad (2.8)$$

where  $\sigma$  is the constant coefficient of the surface tension and  $\varkappa$  the mean curvature of the free surface. The stated pressure  $p^*$  in Eq. (2.3) is the hydrodynamic pressure considered relatively with respect to the constant atmospheric pressure  $p_0^*$ .

**Remark 2.2** The given fiber problem is addressed with the zero initial condition Eq. (2.7). This initial condition states that in the starting phase of the spinning process the length of the fiber is very small, even smaller than the length of the nozzle. Thus, in the starting phase the fiber can not be described as a slender body. However, in this work we are interested in the phase when the fiber has grown up to a certain minimum length and slender body theory is applicable.

**Remark 2.3** The body forces  $\mathbf{f}^*$  used in Eq. (2.2) are discussed in more detail later in Section 2.7. The reason behind expressing the stress tensor  $\mathbf{S}^*$  in a separate Eq. (2.3) is explained in Section 2.5 (Theorem 2.2).

**Remark 2.4** If the free surface is given implicitly by a function or explicitly in a parameterized form, then we are able to calculate the normal vector and surface speed. In detail:

- If we describe the free surface implicitly by a function  $H^*(\cdot, t^*): \mathbb{R}^3 \mapsto \mathbb{R}$ , with  $H^*(\mathbf{r}^*, t^*) < 0$  for  $\mathbf{r}^* \in \Omega^*(t^*)$  and  $H^*(\mathbf{r}^*, t^*) > 0$  for  $\mathbf{r}^* \notin \Omega^*(t^*)$ , i.e.

$$\Gamma_{fr}^*(t^*) = \{\mathbf{r}^* \in \mathbb{R}^3 \setminus \Gamma_{in}^* : H^*(\mathbf{r}^*, t^*) = 0\}$$

then for  $\mathbf{r}^* \in \Gamma_{fr}^*(t^*)$  the normal vector and surface speed are given by

$$\mathbf{n}^*(\mathbf{r}^*, t^*) = \frac{\nabla H^*}{\|\nabla H^*\|}(\mathbf{r}^*, t^*) \quad \text{and} \quad w^*(\mathbf{r}^*, t^*) = -\frac{\partial_{t^*} H^*}{\|\nabla H^*\|}(\mathbf{r}^*, t^*). \quad (2.9)$$

We assume that  $H^*$  is at least of class  $\mathcal{C}^1$ . In this case, the kinematic boundary condition Eq. (2.4) can be written in the following way

$$\partial_{t^*} H^*(\mathbf{r}^*, t^*) + (\mathbf{v}^* \cdot \nabla H^*)(\mathbf{r}^*, t^*) = 0 \quad \text{for} \quad \mathbf{r}^* \in \Gamma_{fr}^*(t^*).$$

- If the free surface is given in a parameterized form by a function  $\zeta^*(\cdot, t^*): \mathcal{U} \subset \mathbb{R}^2 \mapsto \Gamma_{fr}^*(t^*)$ , then for any  $(\vartheta, \varphi) \in \mathcal{U}$ , the normal vector and surface speed are given by

$$\begin{aligned} \mathbf{n}^*(\zeta^*(\vartheta, \varphi, t^*), t^*) &= \frac{\partial_{\vartheta} \zeta^* \times \partial_{\varphi} \zeta^*}{\|\partial_{\vartheta} \zeta^* \times \partial_{\varphi} \zeta^*\|}(\vartheta, \varphi, t^*) \quad \text{and} \\ w^*(\zeta^*(\vartheta, \varphi, t^*), t^*) &= \partial_{t^*} \zeta^*(\vartheta, \varphi, t^*) \cdot \mathbf{n}^*(\zeta^*(\vartheta, \varphi, t^*), t^*). \end{aligned} \quad (2.10)$$

We consider that  $\zeta^*$  is a bijective mapping and at least of class  $\mathcal{C}^1$ . In this case the kinematic condition Eq. (2.4) can be rewritten in the following way

$$(\mathbf{v}(\zeta^*(\vartheta, \varphi, t^*), t^*) - \partial_{t^*} \zeta^*(\vartheta, \varphi, t^*)) \cdot (\partial_{\vartheta} \zeta^* \times \partial_{\varphi} \zeta^*)(\vartheta, \varphi, t^*) = 0.$$

For the asymptotic analysis of slender body theory, the implicit description of the free surface is used by many authors, e.g. [10, 11]. In the present work, we deal with an explicit representation for technical reasons.

## 2.3 Non-dimensionalization

### 2.3.1 Scaling

We non-dimensionalize the variables by a typical fiber length in the process  $L_0$ , a typical velocity  $V$  and by the given constant fluid density  $\rho$ . We particularly choose  $V$  as the mean velocity at the nozzle, i.e.

$$V = -\frac{\int_{\Gamma_{in}^*} \mathbf{v}_{in}^* \cdot \mathbf{n}^* d\mathcal{A}}{\int_{\Gamma_{in}^*} d\mathcal{A}} \quad (2.11)$$

The negative sign is due to the direction of normal vector at the nozzle. Then, we obtain:



Space-time variables:

$$\mathbf{r}^* = L_0 \mathbf{r} \qquad t^* = (L_0/V)t$$

Geometry:

$$\mathbf{n}^*(L_0 \mathbf{r}, (L_0/V)t) = \mathbf{n}(\mathbf{r}, t) \qquad w^*(L_0 \mathbf{r}, (L_0/V)t) = Vw(\mathbf{r}, t)$$

Observables:

$$\begin{aligned} \mathbf{v}^*(L_0 \mathbf{r}, (L_0/V)t) &= V\mathbf{v}(\mathbf{r}, t) & p^*(L_0 \mathbf{r}, (L_0/V)t) &= \rho V^2 p(\mathbf{r}, t) \\ \mathbf{S}^*(L_0 \mathbf{r}, (L_0/V)t) &= \rho V^2 \mathbf{S}(\mathbf{r}, t) & \mathbf{f}^*(L_0 \mathbf{r}, (L_0/V)t) &= (\rho V^2/L_0) \mathbf{f}(\mathbf{r}, t) \end{aligned}$$

Fiber domain:

$$\begin{aligned} \Omega^*((L_0/V)t) &= L_0 \Omega(t) \\ \Gamma_{fr}^*((L_0/V)t) &= L_0 \Gamma_{fr}(t) & \Gamma_{in}^* &= L_0 \Gamma_{in} \end{aligned}$$

The important dimensionless parameter is the Reynolds number  $\text{Re} = \rho L_0 V / \mu$  that characterizes the relation between inertial and viscous forces.

### 2.3.2 Model equations in non-dimensional form

After using the above transformation relations the model equations for  $t \in \mathbb{R}^+$  in non-dimensional form read:

*Conservation of mass and momentum,  $\mathbf{r} \in \Omega(t)$*

$$\nabla \cdot \mathbf{v}(\mathbf{r}, t) = 0 \tag{2.12}$$

$$\partial_t \mathbf{v}(\mathbf{r}, t) + \nabla \cdot (\mathbf{v} \otimes \mathbf{v})(\mathbf{r}, t) = \nabla \cdot \mathbf{S}^T(\mathbf{r}, t) + \mathbf{f}(\mathbf{r}, t) \tag{2.13}$$

*Constitutive law*

$$\mathbf{S} = -p\mathbf{I} + \frac{1}{\text{Re}}(\nabla \mathbf{v} + (\nabla \mathbf{v})^T) \tag{2.14}$$

*Kinematic and dynamic boundary conditions,  $\mathbf{r} \in \Gamma_{fr}(t)$*

$$(\mathbf{v} \cdot \mathbf{n})(\mathbf{r}, t) = w(\mathbf{r}, t) \tag{2.15}$$

$$(\mathbf{S} \cdot \mathbf{n})(\mathbf{r}, t) = \mathbf{0} \tag{2.16}$$

*Inflow boundary condition,  $\mathbf{r} \in \Gamma_{in}$*

$$\mathbf{v}(\mathbf{r}, t) = \mathbf{v}_{in}(\mathbf{r}) \tag{2.17}$$

*Initial condition*

$$\Omega(0) = \emptyset \tag{2.18}$$

### 2.3.3 Identification of a small parameter

Consideration of the slender fiber geometry allows the identification of the slenderness parameter  $\epsilon$

$$\epsilon = |\Gamma_{in}|^{1/2} = \frac{|\Gamma_{in}^*|^{1/2}}{L_0}, \quad (2.19)$$

where  $|\Gamma_{in}| = \int_{\Gamma_{in}} d\mathcal{A}$  is the measure of the inflow boundary  $\Gamma_{in}$ . In the following we search for an asymptotic solution of our problem for small  $\epsilon$ .

Finally, Eq. (2.11) reads in the dimensionless form

$$-\frac{\int_{\Gamma_{in}} \mathbf{v}_{in} \cdot \mathbf{n} d\mathcal{A}}{\int_{\Gamma_{in}} d\mathcal{A}} = 1. \quad (2.20)$$

## 2.4 Model equations in general coordinates

By modeling a fiber that is emerging from a rotating device, it is natural to assume that its curvature is not negligibly small. To describe the motion of the curved slender fiber efficiently, we rewrite therefore the free boundary value problem in a scaled curvilinear coordinate system associated with the fixed parameter  $\epsilon$  and analyze the problem asymptotically. In order to do this, we first transform the non-dimensional fiber system (2.12)-(2.18) in general coordinates. In Section 2.5 the scaled curvilinear coordinates will be then treated as a particular special case.

The balance laws in general time-independent coordinates are well known in literature, e.g. [29]. Whenever the general coordinates depend on time, special care is needed to formulate the balance laws. Many research papers, e.g. [26] and [36], are devoted to the derivation of the contravariant form of the Navier-Stokes equations in time-dependent general coordinates. In the present work, we follow a concept for the coordinate transformation that is exemplified in [1] for the transformation from Lagrange to Euler coordinates. More precisely, we formulate the conservation laws by incorporating the velocity vectors in both, the Cartesian and the general coordinate system. More details are given in the following.

### 2.4.1 Concept

A time-dependent coordinate transformation for any  $t \in \mathbb{R}^+$  is defined by the function

$$\check{\mathbf{r}}(\cdot, t): \hat{\Omega}(t) \subset \mathbb{R}^3 \mapsto \Omega(t) \subset \mathbb{R}^3, \quad (\mathbf{x}, t) \mapsto \check{\mathbf{r}}(\mathbf{x}, t).$$

We suppose that  $\check{\mathbf{r}}$  is of class  $\mathcal{C}^2$  and  $\check{\mathbf{r}}(\cdot, t)$  is bijective. We denote its inverse map by  $\check{\mathbf{x}}$ , i.e.

$$\check{\mathbf{r}}(\check{\mathbf{x}}(\mathbf{r}, t), t) = \mathbf{r} \quad \text{and} \quad \check{\mathbf{x}}(\check{\mathbf{r}}(\mathbf{x}, t), t) = \mathbf{x}.$$

We denote the coordinate transformation matrix as

$$\mathbf{F}(\mathbf{x}, t) = \nabla_{\mathbf{x}} \check{\mathbf{r}}(\mathbf{x}, t), \quad (2.21)$$

its functional determinant as

$$J(\mathbf{x}, t) = \det(\mathbf{F}(\mathbf{x}, t)) \quad (2.22)$$

and its inverse matrix as

$$\mathbf{G}(\mathbf{x}, t) = \mathbf{F}^{-1}(\mathbf{x}, t) = \nabla_{\mathbf{r}} \check{\mathbf{x}}(\check{\mathbf{r}}(\mathbf{x}, t), t). \quad (2.23)$$

We further introduce

$$\tilde{\mathbf{q}}(\mathbf{x}, t) = \partial_t \check{\mathbf{r}}(\mathbf{x}, t) \quad \text{or} \quad \mathbf{q}(\mathbf{r}, t) = \tilde{\mathbf{q}}(\check{\mathbf{x}}(\mathbf{r}, t), t) \quad (2.24)$$

as the velocity of the coordinates.

We generally use the notation of Eq. (2.24) for the transformation of scalar, vector and tensor fields, i.e.

$$\tilde{f}(\mathbf{x}, t) = f(\check{\mathbf{r}}(\mathbf{x}, t), t) \quad \text{and} \quad f(\mathbf{r}, t) = \tilde{f}(\check{\mathbf{x}}(\mathbf{r}, t), t). \quad (2.25)$$

In the next two sections we introduce special transformations for the fields of mass density, volume force density, velocity and stress as well as for the geometric quantities of normal vector and surface speed.

## 2.4.2 Transformation of observables

### 2.4.2.1 Mass density and volume force density

Due to scaling and the assumption of incompressibility the mass density in the spatial coordinates is 1. We define in the general coordinates

$$\hat{\rho}(\mathbf{x}, t) = J(\mathbf{x}, t). \quad (2.26)$$

This definition (2.26) guarantees that for  $\mathcal{B} \subset \hat{\Omega}(t)$

$$\int_{\mathcal{B}} \hat{\rho}(\mathbf{x}, t) d\mathbf{x} = \int_{\mathcal{B}} J(\mathbf{x}, t) d\mathbf{x} = \int_{\check{\mathbf{r}}(\mathcal{B}, t)} d\mathbf{r}.$$

The integration of  $\hat{\rho}$  over the domain  $\mathcal{B}$  in the general coordinates gives the mass in the spatial image  $\check{\mathbf{r}}(\mathcal{B}, t)$  of this domain. Similarly, the volume force density is defined as

$$\hat{\mathbf{f}}(\mathbf{x}, t) = J(\mathbf{x}, t) \tilde{\mathbf{f}}(\mathbf{x}, t). \quad (2.27)$$

### 2.4.2.2 Velocity

Let  $\mathbf{v}(\mathbf{r}, t)$  be the velocity in the space point  $\mathbf{r}$  at time  $t$ . Using  $\tilde{\mathbf{q}}$  and  $\tilde{\mathbf{v}}$  given by Eqs. (2.24) and (2.25), we define with respect to the general coordinates the "intrinsic" velocity

$$\hat{\mathbf{v}}(\mathbf{x}, t) = (\tilde{\mathbf{v}}(\mathbf{x}, t) - \tilde{\mathbf{q}}(\mathbf{x}, t)) \cdot \mathbf{G}(\mathbf{x}, t). \quad (2.28)$$

This definition (2.28) is motivated by the following considerations. The velocity field  $\mathbf{v}(\mathbf{r}, t)$  in the space point  $\mathbf{r}$  at time  $t$  is realized as tangent vector to a space curve parameterized by time, let us say  $\mathbf{\Upsilon}(t)$ . Then we define

$$\mathbf{v}(\mathbf{r}, t) = \partial_t \mathbf{\Upsilon}(t) \quad \text{with} \quad \mathbf{r} = \mathbf{\Upsilon}(t).$$

The corresponding curve  $\hat{\mathbf{\Upsilon}}(t)$  in the general coordinates satisfies  $\mathbf{\Upsilon}(t) = \check{\mathbf{r}}(\hat{\mathbf{\Upsilon}}(t), t)$ . Then

$$\partial_t \mathbf{\Upsilon}(t) = \partial_t \hat{\mathbf{\Upsilon}}(t) \cdot \mathbf{F}(\hat{\mathbf{\Upsilon}}(t), t) + \tilde{\mathbf{q}}(\hat{\mathbf{\Upsilon}}(t), t).$$

We introduce

$$\hat{\mathbf{v}}(\mathbf{x}, t) = \partial_t \hat{\mathbf{\Upsilon}}(t) \quad \text{with} \quad \mathbf{x} = \hat{\mathbf{\Upsilon}}(t)$$

as the velocity field in the general coordinates in the position  $\mathbf{x}$  at time  $t$ . Thus, we get

$$\tilde{\mathbf{v}}(\mathbf{x}, t) = \mathbf{v}(\check{\mathbf{r}}(\mathbf{x}, t), t) = \hat{\mathbf{v}}(\mathbf{x}, t) \cdot \mathbf{F}(\mathbf{x}, t) + \tilde{\mathbf{q}}(\mathbf{x}, t).$$

Thus, the definition (2.28) guarantees that  $\hat{\mathbf{v}}$  is tangent to the transformed space curve.

### 2.4.2.3 Stress tensor

Let  $\mathbf{S}(\mathbf{r}, t)$  be the stress tensor in the space point  $\mathbf{r}$  at time  $t$ . Using  $\tilde{\mathbf{S}}$  given by Eq. (2.25), we define

$$\hat{\mathbf{S}}(\mathbf{x}, t) = J(\mathbf{x}, t) \tilde{\mathbf{S}}(\mathbf{x}, t) \cdot \mathbf{G}(\mathbf{x}, t). \quad (2.29)$$

This definition (2.29) makes sure that for a surface  $\mathcal{S}$  in the general coordinates with normal vector  $\hat{\mathbf{n}}$  and the spatial image  $\check{\mathbf{r}}(\mathcal{S}, t)$  with normal vector  $\mathbf{n}$ , the following relation holds

$$\int_{\mathcal{S}} (\hat{\mathbf{S}} \cdot \hat{\mathbf{n}})(\mathbf{x}, t) d\mathcal{A} = \int_{\check{\mathbf{r}}(\mathcal{S}, t)} (\mathbf{S} \cdot \mathbf{n})(\mathbf{r}, t) d\mathcal{A}.$$

For the proof of this relation we refer to [1].

### 2.4.3 Transformation of the geometry

Let  $\mathbf{n}(\mathbf{r}, t)$  be the normal vector to the free surface in the space point  $\mathbf{r}$  at time  $t$ . Using  $\tilde{\mathbf{n}}$  given by Eq. (2.25), we define

$$\hat{\mathbf{n}}(\mathbf{x}, t) = \frac{\mathbf{F} \cdot \tilde{\mathbf{n}}}{\|\mathbf{F} \cdot \tilde{\mathbf{n}}\|}(\mathbf{x}, t). \quad (2.30)$$

Let  $w(\mathbf{r}, t)$  be the speed of the free surface in the space point  $\mathbf{r}$  at time  $t$ . Using  $\tilde{\mathbf{q}}$ ,  $\tilde{w}$  and  $\tilde{\mathbf{n}}$  given by Eqs. (2.24) and (2.25), we define

$$\hat{w}(\mathbf{x}, t) = \frac{(\tilde{w} - \tilde{\mathbf{q}} \cdot \tilde{\mathbf{n}})}{\|\mathbf{F} \cdot \tilde{\mathbf{n}}\|}(\mathbf{x}, t). \quad (2.31)$$

The motivation for the definitions in Eqs. (2.30) and (2.31) are due to the following reasons. If the free surface is given implicitly by  $H(\mathbf{r}, t) = 0$ , according to Remark 2.4, then the normal vector and the surface speed read

$$\mathbf{n}(\mathbf{r}, t) = \frac{\nabla_{\mathbf{r}} H}{\|\nabla_{\mathbf{r}} H\|}(\mathbf{r}, t) \quad \text{and} \quad w(\mathbf{r}, t) = -\frac{\partial_t H}{\|\nabla_{\mathbf{r}} H\|}(\mathbf{r}, t).$$

As a consequence of the transformation relation in Eq. (2.25), we have

$$\begin{aligned} \nabla_{\mathbf{x}} \tilde{H}(\mathbf{x}, t) &= \mathbf{F}(\mathbf{x}, t) \cdot \nabla_{\mathbf{r}} H(\mathbf{r}, t)|_{\mathbf{r}=\check{\mathbf{r}}(\mathbf{x}, t)} \quad \text{and} \\ \partial_t \tilde{H}(\mathbf{x}, t) &= \partial_t H(\mathbf{r}, t) + \mathbf{q}(\mathbf{r}, t) \cdot \nabla_{\mathbf{r}} H(\mathbf{r}, t)|_{\mathbf{r}=\check{\mathbf{r}}(\mathbf{x}, t)}. \end{aligned}$$

By using these equations one can easily prove that

$$\hat{\mathbf{n}}(\mathbf{x}, t) = \frac{\nabla_{\mathbf{x}} \tilde{H}}{\|\nabla_{\mathbf{x}} \tilde{H}\|}(\mathbf{x}, t) \quad \text{and} \quad \hat{w}(\mathbf{x}, t) = -\frac{\partial_t \tilde{H}}{\|\nabla_{\mathbf{x}} \tilde{H}\|}(\mathbf{x}, t),$$

i.e.  $\hat{\mathbf{n}}$  and  $\hat{w}$  are the normal vector and surface speed of the transformed geometry.

### 2.4.4 Transformation of the free boundary value problem

In this section the transformation of the free boundary value problem in general coordinates is presented. For the transformation stated in Theorem 2.1 the following lemma is needed. Although especially the first part of the lemma is well known in literature, e.g. [1, 20], we prefer to give here a short proof for the better understanding.

**Lemma 2.1** Let the functions  $J$ ,  $\mathbf{G}$ , and  $\mathbf{q}$  be given as in Eqs. (2.22)- (2.24). Then the following relations hold

$$\partial_t J = J \nabla_{\mathbf{r}} \cdot \mathbf{q}|_{\mathbf{r}=\check{\mathbf{r}}(\mathbf{x}, t)} \quad (2.32)$$

$$\nabla_{\mathbf{x}} \cdot (J \mathbf{G}^T) = \mathbf{0}. \quad (2.33)$$

**Proof.** For the proof we use the following relation: Let  $\mathbf{Lin}$  denote the set of linear transformations  $\mathbf{A} : \mathbb{R}^3 \mapsto \mathbb{R}^3$  (set of real valued second order tensors) with determinant  $\det : \mathbf{Lin} \mapsto \mathbb{R}$ ,  $\mathbf{A} \mapsto \det(\mathbf{A})$ . Then by means of Fréchet derivative, we have

$$\partial_{\mathbf{A}} \det(\mathbf{A})(\mathbf{B}) = (\det \mathbf{A}) \mathbf{A}^{-T} : \mathbf{B} \quad (2.34)$$

for every  $\mathbf{B} \in \mathbf{Lin}$ . The relation (2.34) is proved for example in [1]. Consequently, we obtain

$$\begin{aligned} \partial_t J &= J \mathbf{F}^{-T} : \partial_t \mathbf{F} = J \mathbf{G}^T : \nabla_{\mathbf{x}} \tilde{\mathbf{q}} = J \operatorname{tr}(\mathbf{G} \cdot \nabla_{\mathbf{x}} \tilde{\mathbf{q}}) \\ &= J \operatorname{tr}(\nabla_{\mathbf{r}} \tilde{\mathbf{x}}|_{\mathbf{r}=\tilde{\mathbf{r}}(\mathbf{x},t)} \cdot \nabla_{\mathbf{x}} \tilde{\mathbf{q}}) = J \operatorname{tr}(\nabla_{\mathbf{r}} \mathbf{q})|_{\mathbf{r}=\tilde{\mathbf{r}}(\mathbf{x},t)} = J \nabla_{\mathbf{r}} \cdot \mathbf{q}|_{\mathbf{r}=\tilde{\mathbf{r}}(\mathbf{x},t)}. \end{aligned}$$

This yields Eq. (2.32).

Again with Eq. (2.34), we have

$$\nabla_{\mathbf{x}} \cdot (J \mathbf{G}^T) = \mathbf{G} \cdot \nabla_{\mathbf{x}} J + J \nabla_{\mathbf{x}} \cdot \mathbf{G}^T = J \mathbf{G} \cdot \nabla_{\mathbf{x}} \mathbf{F} : \mathbf{G}^T + J \nabla_{\mathbf{x}} \cdot \mathbf{G}^T$$

and

$$\nabla_{\mathbf{x}} \mathbf{F} : \mathbf{G}^T = \nabla_{\mathbf{x}} \nabla_{\mathbf{x}} \tilde{\mathbf{r}} : \mathbf{G}^T = \nabla_{\mathbf{x}} \cdot (\nabla_{\mathbf{x}} \tilde{\mathbf{r}} \cdot \mathbf{G}) - \nabla_{\mathbf{x}} \tilde{\mathbf{r}} \cdot (\nabla_{\mathbf{x}} \cdot \mathbf{G}^T) = -\mathbf{F} \cdot (\nabla_{\mathbf{x}} \cdot \mathbf{G}^T)$$

which results in Eq. (2.33).  $\square$

**Theorem 2.1** The governing equations of the problem in the general coordinates are:

*Conservation of mass and momentum,  $\mathbf{x} \in \hat{\Omega}(t)$*

$$\partial_t J(\mathbf{x}, t) + \nabla_{\mathbf{x}} \cdot (J \hat{\mathbf{v}})(\mathbf{x}, t) = 0 \quad (2.35)$$

$$\partial_t (J \tilde{\mathbf{v}})(\mathbf{x}, t) + \nabla_{\mathbf{x}} \cdot (J \hat{\mathbf{v}} \otimes \tilde{\mathbf{v}})(\mathbf{x}, t) = \nabla_{\mathbf{x}} \cdot \hat{\mathbf{S}}^T(\mathbf{x}, t) + \hat{\mathbf{f}}(\mathbf{x}, t) \quad (2.36)$$

*Coupling condition*

$$\hat{\mathbf{v}} = (\tilde{\mathbf{v}} - \tilde{\mathbf{q}}) \cdot \mathbf{G} \quad (2.37)$$

*Constitutive law*

$$\hat{\mathbf{S}} = J \left( -\tilde{p} \mathbf{I} + \frac{1}{\operatorname{Re}} ((\mathbf{G} \cdot \nabla \tilde{\mathbf{v}}) + (\mathbf{G} \cdot \nabla \tilde{\mathbf{v}})^T) \right) \cdot \mathbf{G} \quad (2.38)$$

*Kinematic and dynamic boundary conditions,  $\mathbf{x} \in \hat{\Gamma}_{fr}(t)$*

$$(\hat{\mathbf{v}} \cdot \hat{\mathbf{n}})(\mathbf{x}, t) = \hat{w}(\mathbf{x}, t) \quad (2.39)$$

$$(\hat{\mathbf{S}} \cdot \hat{\mathbf{n}})(\mathbf{x}, t) = \mathbf{0} \quad (2.40)$$

*Inflow boundary condition,  $\mathbf{x} \in \hat{\Gamma}_{in}$*

$$\tilde{\mathbf{v}}(\mathbf{x}, t) = \tilde{\mathbf{v}}_{in}(\mathbf{x}) \quad (2.41)$$

*Initial condition*

$$\hat{\Omega}(0) = \emptyset \quad (2.42)$$

**Proof.** We lead the proof with the help of Lemma 2.1 and on the basis of the definitions of the respective fields.

$$\partial_t J = J(\nabla_{\mathbf{r}} \cdot \mathbf{q})|_{\mathbf{r}=\check{\mathbf{r}}(\mathbf{x},t)}$$

and by using Eq. (2.28), we have

$$\nabla_{\mathbf{x}} \cdot (J\hat{\mathbf{v}}) = \nabla_{\mathbf{x}} \cdot (J(\tilde{\mathbf{v}} - \tilde{\mathbf{q}}) \cdot \mathbf{G}) = J \nabla_{\mathbf{r}} \cdot (\mathbf{v} - \mathbf{q})|_{\mathbf{r}=\check{\mathbf{r}}(\mathbf{x},t)}.$$

This gives Eq. (2.35).

After similar calculations, we obtain

$$\partial_t(J\tilde{\mathbf{v}}) = J(\partial_t \mathbf{v} + \nabla_{\mathbf{r}} \cdot (\mathbf{q} \otimes \mathbf{v}))|_{\mathbf{r}=\check{\mathbf{r}}(\mathbf{x},t)},$$

and

$$\nabla_{\mathbf{x}} \cdot (J\hat{\mathbf{v}} \otimes \tilde{\mathbf{v}}) = J(\nabla_{\mathbf{r}} \cdot ((\mathbf{v} - \mathbf{q}) \otimes \mathbf{v}))|_{\mathbf{r}=\check{\mathbf{r}}(\mathbf{x},t)}.$$

The first part of the above calculation can also be easily concluded from the Reynolds transport theorem [16].

The stress relation gives

$$\nabla_{\mathbf{x}} \cdot \hat{\mathbf{S}}^T = \nabla_{\mathbf{x}} \cdot (J \tilde{\mathbf{S}} \cdot \mathbf{G})^T = J \nabla_{\mathbf{r}} \cdot \mathbf{S}^T|_{\mathbf{r}=\check{\mathbf{r}}(\mathbf{x},t)}.$$

The outer volume force density simply reads by definition

$$\hat{\mathbf{f}} = J\mathbf{f}|_{\mathbf{r}=\check{\mathbf{r}}(\mathbf{x},t)}.$$

These relations yields Eq. (2.36).

The coupling condition Eq. (2.37) is the definition of  $\hat{\mathbf{v}}$ . The proof of Eqs. (2.39) and (2.40) follows directly from the definitions of the respective quantities. The inflow boundary condition Eq. (2.41) is just a consequence of the fact that the velocity is defined at the new position. The transformation of the constitutive law Eq. (2.38) can be concluded from the definition of the field given in Eq. (2.25) and the chain rule.  $\square$

**Remark 2.5** If the coordinate transformation is given by  $\partial_t \check{\mathbf{r}} = \tilde{\mathbf{v}}$  with  $\check{\mathbf{r}}(\mathbf{x}, 0) = \mathbf{x}$ , then we have  $\tilde{\mathbf{q}} = \tilde{\mathbf{v}}$  and therefore  $\hat{\mathbf{v}} = \mathbf{0}$ . In this special case, Eqs. (2.35)-(2.42) are the free boundary value problem in Lagrangian coordinates.

**Remark 2.6** The "intrinsic" velocity in the general coordinates  $\hat{\mathbf{v}}(\mathbf{x}, t)$  describes the convection in the mass and momentum equations Eq. (2.35) and (2.36), whereas  $\tilde{\mathbf{v}}(\mathbf{x}, t) = \mathbf{v}(\check{\mathbf{r}}(\mathbf{x}, t), t)$  is associated with the momentum, i.e. the transported quantity.

## 2.5 Scaled curvilinear coordinates

In the previous section, the governing equations and the free surface conditions were described in a time-dependent general coordinate system. In this section, we will now introduce a curve in the fiber domain  $\Omega(t)$  that can be interpreted as the center-line. We will construct scaled curvilinear coordinates with respect to this curve. We will follow the general procedure given in the previous section and write the equations of motion and free surface conditions with respect to the scaled curvilinear coordinates.

### 2.5.1 Concept

Let  $\gamma(s, t)$  be a three-dimensional time-dependent arc-length parameterized curve in the domain  $\Omega(t) \subset \mathbb{R}^3$  with arc-length  $s \in \mathbb{R}_0^+$ . In the following sections the domain  $\Omega(t)$  will be interpreted as the fiber domain. By assuming  $\gamma \in \mathcal{C}^3$ , we introduce the curvature  $\kappa = \|\partial_{ss}\gamma\|$ . Moreover, with the technical assumption that  $\kappa \neq 0$ , the torsion of the curve is given by

$$\lambda = \frac{1}{\kappa^2} \partial_s \gamma \cdot (\partial_{ss}\gamma \times \partial_{sss}\gamma).$$

The tangent, normal and binormal vectors with respect to the curve  $\gamma$  are

$$\boldsymbol{\tau} = \partial_s \gamma, \quad \boldsymbol{\eta} = \frac{1}{\kappa} \partial_{ss}\gamma \quad \text{and} \quad \mathbf{b} = \boldsymbol{\tau} \times \boldsymbol{\eta} \quad (2.43)$$

and they are related with the following formulas,

$$\begin{aligned} \partial_s \boldsymbol{\tau} &= \kappa \boldsymbol{\eta} \\ \partial_s \boldsymbol{\eta} &= -\kappa \boldsymbol{\tau} + \lambda \mathbf{b} \\ \partial_s \mathbf{b} &= -\lambda \boldsymbol{\eta}. \end{aligned} \quad (2.44)$$

These so-called Serret-Frenet formulae are stated for example in [13]. Now, we conveniently transform the normal and binormal vectors in the following way [3]

$$\begin{aligned} \boldsymbol{\eta}_1 &= \cos(\phi) \boldsymbol{\eta} - \sin(\phi) \mathbf{b} \\ \boldsymbol{\eta}_2 &= \sin(\phi) \boldsymbol{\eta} + \cos(\phi) \mathbf{b} \end{aligned} \quad (2.45)$$

with the torsion angle

$$\phi(s, t) = \int_0^s \lambda(s', t) ds'.$$

Using this transformation in Eq. (2.44) leads to

$$\begin{aligned} \partial_s \boldsymbol{\tau} &= \kappa \cos(\phi) \boldsymbol{\eta}_1 + \kappa \sin(\phi) \boldsymbol{\eta}_2 \\ \partial_s \boldsymbol{\eta}_1 &= -\kappa \cos(\phi) \boldsymbol{\tau} \\ \partial_s \boldsymbol{\eta}_2 &= -\kappa \sin(\phi) \boldsymbol{\tau}. \end{aligned} \quad (2.46)$$



We now introduce scaled curvilinear coordinates depending on the curve  $\gamma$ .

The specific coordinate transformation map with respect to a given curve  $\gamma$  and for a fixed  $\epsilon \in \mathbb{R}^+$  is defined by

$$\check{\mathbf{r}}_{\gamma, \epsilon}(\mathbf{x}, t) = \gamma(s, t) + \epsilon x_1 \boldsymbol{\eta}_1(s, t) + \epsilon x_2 \boldsymbol{\eta}_2(s, t) \quad \text{with } s = x_3. \quad (2.47)$$

In the following sections  $\epsilon$  will be interpreted as the slenderness parameter given in Eq. (2.19). For brevity we write  $\check{\mathbf{r}}$  instead of  $\check{\mathbf{r}}_{\gamma, \epsilon}$ . Assuming that  $\check{\mathbf{r}}$  is a bijective map, the corresponding coordinates are called scaled curvilinear coordinates with respect to  $\gamma$  and  $\epsilon$ . A sample sketch of the scaled curvilinear coordinates is given in Fig. 2.1.

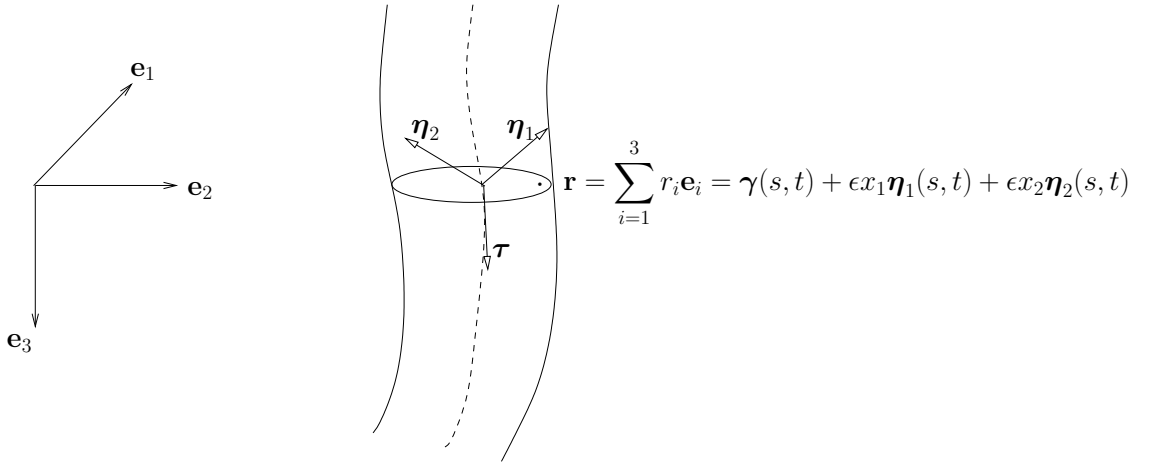


Figure 2.1: Sketch of the scaled curvilinear coordinates

The map (2.47) deserves a few comments. Firstly, the map  $\check{\mathbf{r}}$  only depends on the curve  $\gamma$  and the slenderness parameter  $\epsilon$ . In case  $\epsilon = 1$ , the scaled curvilinear coordinates reduce to un-scaled ones. Secondly, the quantities  $\mathbf{F}$ ,  $J$  and  $\mathbf{G}$  that are defined in Eqs. (2.21)-(2.23) depend also only on the curve  $\gamma$  and the parameter  $\epsilon$ .

**Convention 2.1** In the following we use the generalized Einstein summation convention: Latin and Greek indices take their values in the sets  $\{1, 2, 3\}$  and  $\{1, 2\}$  respectively.

We recall relation (2.46) and rewrite it using the Einstein summation convention

$$\begin{aligned} \partial_s \boldsymbol{\tau} &= (\partial_\alpha h) \boldsymbol{\eta}_\alpha \\ \partial_s \boldsymbol{\eta}_\alpha &= -(\partial_\alpha h) \boldsymbol{\tau}, \end{aligned} \quad (2.48)$$

where

$$h(\mathbf{x}, t) = x_1 \kappa \cos(\phi) + x_2 \kappa \sin(\phi).$$

Additionally, we note that  $x_\alpha \partial_\alpha h = h$ .

We study now this special coordinate transformation using the canonical basis in  $\mathbb{R}^3$ ,

$$\mathbf{e}_1 = (1, 0, 0), \quad \mathbf{e}_2 = (0, 1, 0), \quad \mathbf{e}_3 = (0, 0, 1).$$

We write the matrix  $\mathbf{F}$  of Eq. (2.21) in the following way

$$\mathbf{F} = \mathbf{e}_i \otimes \mathbf{f}_i, \quad \text{where } \mathbf{f}_i = \partial_i \check{\mathbf{r}}. \quad (2.49)$$

The  $\mathbf{f}_i$  are the "row vectors" of  $\mathbf{F}$  that are given by

$$\mathbf{f}_1 = \epsilon \boldsymbol{\eta}_1, \quad \mathbf{f}_2 = \epsilon \boldsymbol{\eta}_2, \quad \mathbf{f}_3 = (1 - \epsilon h) \boldsymbol{\tau}. \quad (2.50)$$

Thus, the determinant of  $\mathbf{F}$  reads

$$J = \epsilon^2 (1 - \epsilon h). \quad (2.51)$$

Similarly, the inverse  $\mathbf{G}$  of Eq. (2.23) is given by

$$\mathbf{G} = \mathbf{g}_i \otimes \mathbf{e}_i, \quad (2.52)$$

where  $\mathbf{g}_i$  are the "column vectors" of  $\mathbf{G}$ . They are equal to

$$\mathbf{g}_1 = \frac{1}{\epsilon} \boldsymbol{\eta}_1, \quad \mathbf{g}_2 = \frac{1}{\epsilon} \boldsymbol{\eta}_2, \quad \mathbf{g}_3 = \frac{1}{(1 - \epsilon h)} \boldsymbol{\tau}. \quad (2.53)$$

Consequently,  $\mathbf{F}$  and  $\mathbf{G}$  consist of  $\boldsymbol{\eta}_1$ ,  $\boldsymbol{\eta}_2$  and  $\boldsymbol{\tau}$  in a simple way. This is one of the reasons why to introduce  $\boldsymbol{\eta}_1$ ,  $\boldsymbol{\eta}_2$  instead of  $\boldsymbol{\eta}$  and  $\mathbf{b}$ .

## 2.5.2 Fiber problem: Scaled curvilinear coordinate system

Before giving the fiber problem in the scaled curvilinear coordinates, we make the following assumptions on the fiber domain and its cross-sections.

**Assumption 2.2** Presupposing the existence of an arc-length parameterized and time-dependent curve  $\boldsymbol{\gamma}: [0, L(t)] \times \mathbb{R}^+ \mapsto \Omega(t)$ , we assume the following:

- The coordinate transformation map (2.47) is a bijective mapping, i.e. scaled curvilinear coordinates exist, see Fig.2.2.
- The fiber domain is given by the "fiber length"  $L(t)$  and the radius function  $R \in \mathcal{C}^1$ ,  $R(\cdot, t): [0, 2\pi) \times [0, L(t)] \mapsto \mathbb{R}^+$  (periodic in  $[0, 2\pi)$ ) in such a way that

$$\Omega(t) = \check{\mathbf{r}}(\hat{\Omega}(t), t) \text{ and}$$

$$\hat{\Omega}(t) = \{ \mathbf{x} = (x_1, x_2, s) \in \mathbb{R}^3 : (x_1, x_2) \in \mathcal{A}(s, t), s \in [0, L(t)] \}.$$

with "cross-section"  $\mathcal{A}(s, t)$  described by

$$\mathcal{A}(s, t) = \{ (x_1, x_2) \in \mathbb{R}^2 : x_1 = \varrho \cos(\psi), x_2 = \varrho \sin(\psi), \\ \varrho \in [0, R(\psi, s, t)], \psi \in [0, 2\pi) \}.$$

- The curve  $\gamma$  can be chosen as center-line, i.e.

$$\int_{\mathcal{A}(s,t)} x_1 dx_1 dx_2 = \int_{\mathcal{A}(s,t)} x_2 dx_1 dx_2 = 0.$$

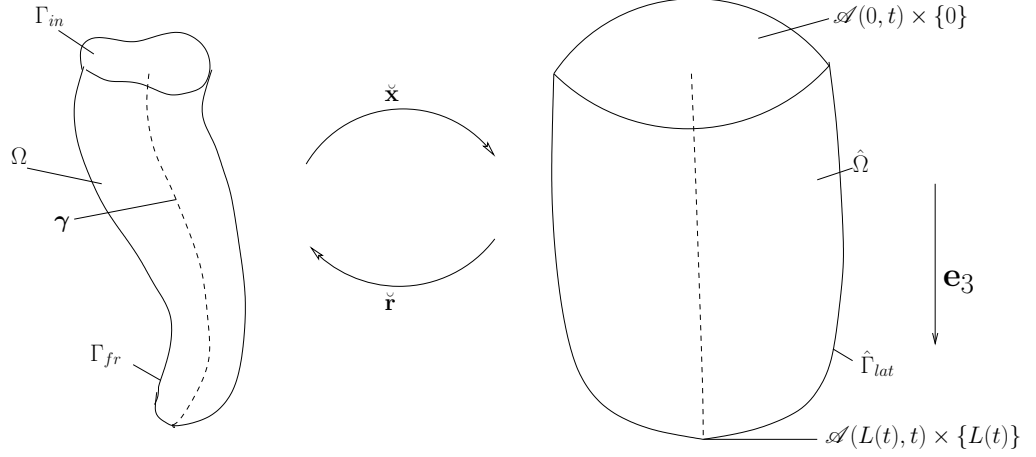


Figure 2.2: Sketch of the fiber domain. Left: In space coordinates, Right: In scaled curvilinear coordinates

As a consequence of Assumption 2.2,  $\gamma(0,t) = \gamma_0$  describes the center of the time-independent planar inflow boundary  $\Gamma_{in}$ , and  $\partial_s \gamma(0,t) = \tau_0$  is the normal of  $\Gamma_{in}$  in negative direction.

**Remark 2.7** With Assumption 2.2, the whole fiber domain can be completely described by three quantities: the fiber length  $L$ , the curve  $\gamma$  and the radius function  $R$ . In the following we refer to both  $\Omega$  (in the spatial coordinates) and  $\hat{\Omega}$  (in the scaled curvilinear coordinates) as fiber domain.

As a further consequence of Assumption 2.2, the lateral surface of the fiber in the scaled curvilinear coordinate that we denote by  $\hat{\Gamma}_{lat}(t)$  is introduced in a parameterized form as follows. For any  $t \in \mathbb{R}^+$ , we define the bijective mapping  $\boldsymbol{\xi}(\cdot, t): [0, 2\pi) \times [0, L(t)) \mapsto \hat{\Gamma}_{lat}(t) \subset \mathbb{R}^3$  by

$$\boldsymbol{\xi}(\psi, s, t) = (R(\psi, s, t) \cos(\psi), R(\psi, s, t) \sin(\psi), s). \quad (2.54)$$

Following Remark 2.4, we can calculate the normal vector  $\hat{\mathbf{n}}$  and the surface speed  $\hat{w}$  as

$$\hat{\mathbf{n}}(\boldsymbol{\xi}, t) = \frac{\partial_\psi \boldsymbol{\xi} \times \partial_s \boldsymbol{\xi}}{\|\partial_\psi \boldsymbol{\xi} \times \partial_s \boldsymbol{\xi}\|} \quad \text{and} \quad \hat{w}(\boldsymbol{\xi}, t) = \partial_t \boldsymbol{\xi} \cdot \hat{\mathbf{n}}(\boldsymbol{\xi}, t). \quad (2.55)$$

Note that here and in the following we use the sloppy notations  $\boldsymbol{\xi} = \boldsymbol{\xi}(\psi, s, t)$  and  $R = R(\psi, s, t)$ .

Under the coordinate transformation of Eq. (2.47), the inflow boundary  $\Gamma_{in}$  is given by

$$\Gamma_{in} = \check{\mathbf{r}}(\mathcal{A}(0, t), 0, t).$$

The inflow cross-section and the inflow velocity in the scaled curvilinear coordinates fulfill

$$|\mathcal{A}(0, t)| = 1 \quad \text{and} \quad \int_{\mathcal{A}(0, t)} \tilde{\mathbf{v}}_{in} \cdot \boldsymbol{\tau}_0 dx_1 dx_2 = 1. \quad (2.56)$$

These relations are a direct consequence of the corresponding relations in Eqs. (2.19) and (2.20) stated in the spatial coordinates.

We now follow the general transformation law given in Section 2.4 and write the free boundary value problem with respect to the scaled curvilinear coordinates introduced in Eq. (2.47).

**Theorem 2.2** The governing equations of the problem in the scaled curvilinear coordinates are:

*Conservation of mass and momentum,  $\mathbf{x} \in \hat{\Omega}(t)$*

$$\partial_t J(\mathbf{x}, t) + \nabla \cdot (J\hat{\mathbf{v}})(\mathbf{x}, t) = 0 \quad (2.57)$$

$$\partial_t (J\tilde{\mathbf{v}})(\mathbf{x}, t) + \nabla \cdot (J\hat{\mathbf{v}} \otimes \tilde{\mathbf{v}})(\mathbf{x}, t) = \nabla \cdot \hat{\mathbf{S}}^T(\mathbf{x}, t) + \hat{\mathbf{f}}(\mathbf{x}, t) \quad (2.58)$$

*Coupling condition*

$$\hat{\mathbf{v}}(\mathbf{x}, t) = ((\tilde{\mathbf{v}} - \tilde{\mathbf{q}}) \cdot \mathbf{G})(\mathbf{x}, t) \quad (2.59)$$

*Constitutive law*

$$\begin{aligned} \hat{\mathbf{S}} = & -\bar{p}[\epsilon(1 - \epsilon h)(\boldsymbol{\eta}_\alpha \otimes \mathbf{e}_\alpha) + \epsilon^2(\boldsymbol{\tau} \otimes \mathbf{e}_3)] \\ & + \frac{1}{\text{Re}}[\epsilon(1 - \epsilon h)(\partial_\alpha(\hat{\mathbf{v}} \cdot \mathbf{e}_\beta) + \partial_\beta(\hat{\mathbf{v}} \cdot \mathbf{e}_\alpha))(\boldsymbol{\eta}_\alpha \otimes \mathbf{e}_\beta) \\ & + (\epsilon(1 - \epsilon h)\partial_\alpha(\hat{\mathbf{v}} \cdot \mathbf{e}_3) + \frac{\epsilon^3}{(1 - \epsilon h)}\partial_s(\hat{\mathbf{v}} \cdot \mathbf{e}_\alpha))(\boldsymbol{\eta}_\alpha \otimes \mathbf{e}_3) \\ & + (\epsilon^2\partial_s(\hat{\mathbf{v}} \cdot \mathbf{e}_\alpha) + (1 - \epsilon h)^2\partial_\alpha(\hat{\mathbf{v}} \cdot \mathbf{e}_3))(\boldsymbol{\tau} \otimes \mathbf{e}_\alpha) \\ & + (2\epsilon^2\partial_s(\hat{\mathbf{v}} \cdot \mathbf{e}_3) - \frac{2\epsilon^3}{(1 - \epsilon h)}(\partial_t h + (\hat{\mathbf{v}} \cdot \mathbf{e}_\alpha)\partial_\alpha h + (\hat{\mathbf{v}} \cdot \mathbf{e}_3)\partial_s h))(\boldsymbol{\tau} \otimes \mathbf{e}_3)] \end{aligned} \quad (2.60)$$

*Kinematic and dynamic boundary conditions (lateral surface),  $\mathbf{x} \in \hat{\Gamma}_{lat}(t)$*

$$(\hat{\mathbf{v}} \cdot \hat{\mathbf{n}})(\mathbf{x}, t) = \hat{w}(\mathbf{x}, t) \quad (2.61)$$

$$(\hat{\mathbf{S}} \cdot \hat{\mathbf{n}})(\mathbf{x}, t) = \mathbf{0} \quad (2.62)$$

*Kinematic and dynamic boundary conditions (bottom surf.),*  $\mathbf{x} \in \mathcal{A}(L(t), t) \times \{L(t)\}$

$$\frac{dL(t)}{dt} = (\hat{\mathbf{v}} \cdot \mathbf{e}_3)(\mathbf{x}, t) \quad \text{with} \quad L(0) = 0 \quad (2.63)$$

$$(\hat{\mathbf{S}} \cdot \mathbf{e}_3)(\mathbf{x}, t) = \mathbf{0} \quad (2.64)$$

*Inflow boundary condition,*  $\mathbf{x} \in \mathcal{A}(0, t) \times \{0\}$

$$\tilde{\mathbf{v}}(\mathbf{x}, t) = \tilde{\mathbf{v}}_{in}(\mathbf{x}) \quad (2.65)$$

*Arc-length parameterization*

$$\|\partial_s \gamma\| = 1 \quad (2.66)$$

*Initial position and direction*

$$\gamma(0, t) = \gamma_0 \quad \text{and} \quad \partial_s \gamma(0, t) = \boldsymbol{\tau}_0 \quad (2.67)$$

*Center-line condition*

$$\int_{\mathcal{A}(s,t)} x_1 dx_1 dx_2 = \int_{\mathcal{A}(s,t)} x_2 dx_1 dx_2 = 0. \quad (2.68)$$

**Proof.** The proof of the theorem is the direct consequence of Theorem 2.1. The boundary conditions at the bottom surface of the fiber Eqs. (2.63) and (2.64) result from the fact that the normal vector at  $\mathcal{A}(L(t), t)$  is  $\mathbf{e}_3$ . For the completion of the proof we only need to calculate the stress tensor. We outline the steps that are required to yield the results.

By using the velocities relations in Eq. (2.59), we write

$$\nabla \tilde{\mathbf{v}} = \nabla(\hat{\mathbf{v}} \cdot \mathbf{F} + \tilde{\mathbf{q}}) = \nabla \hat{\mathbf{v}} \cdot \mathbf{F} + \nabla \mathbf{F}^T \cdot \hat{\mathbf{v}} + \nabla \tilde{\mathbf{q}}. \quad (2.69)$$

Applying Eq. (2.69), we rewrite the stress tensor  $\hat{\mathbf{S}}$  given in Eq. (2.38) in the following way

$$\begin{aligned} \hat{\mathbf{S}} = J[-\tilde{p} \mathbf{I} \cdot \mathbf{G} + \frac{1}{\text{Re}} \{ & ((\mathbf{G} \cdot \nabla \hat{\mathbf{v}} \cdot \mathbf{F}) + (\mathbf{G} \cdot \nabla \hat{\mathbf{v}} \cdot \mathbf{F})^T) \cdot \mathbf{G} \\ & + ((\mathbf{G} \cdot \nabla \mathbf{F}^T \cdot \hat{\mathbf{v}}) + (\mathbf{G} \cdot \nabla \mathbf{F}^T \cdot \hat{\mathbf{v}})^T) \cdot \mathbf{G} + ((\mathbf{G} \cdot \nabla \tilde{\mathbf{q}}) + (\mathbf{G} \cdot \nabla \tilde{\mathbf{q}})^T) \cdot \mathbf{G} \}], \end{aligned} \quad (2.70)$$

where the velocity of the coordinates  $\tilde{\mathbf{q}}$  is

$$\tilde{\mathbf{q}} = \partial_t \check{\mathbf{r}} = \partial_t \gamma + \epsilon x_\alpha \partial_t \boldsymbol{\eta}_\alpha. \quad (2.71)$$

For the final computation of the stress tensor, we draw the reader's attention to the typical steps of the calculation procedure. Starting with

$$\nabla \mathbf{F}^T = \mathbf{e}_i \otimes \partial_i \mathbf{f}_j \otimes \mathbf{e}_j. \quad (2.72)$$

We split the terms of Eq. (2.72) in the following way

$$\nabla \mathbf{F}^T = \mathbf{e}_\alpha \otimes \partial_\alpha \mathbf{f}_\beta \otimes \mathbf{e}_\beta + \mathbf{e}_\alpha \otimes \partial_\alpha \mathbf{f}_3 \otimes \mathbf{e}_3 + \mathbf{e}_3 \otimes \partial_s \mathbf{f}_\beta \otimes \mathbf{e}_\beta + \mathbf{e}_3 \otimes \partial_s \mathbf{f}_3 \otimes \mathbf{e}_3.$$

By using Eqs. (2.48) and (2.50), we get

$$\begin{aligned} \nabla \mathbf{F}^T &= -\epsilon \partial_\alpha h(\mathbf{e}_\alpha \otimes \boldsymbol{\tau} \otimes \mathbf{e}_3) - \epsilon \partial_\alpha h(\mathbf{e}_3 \otimes \boldsymbol{\tau} \otimes \mathbf{e}_\beta) \\ &\quad - \epsilon \partial_s h(\mathbf{e}_3 \otimes \boldsymbol{\tau} \otimes \mathbf{e}_3) + (1 - \epsilon h) \partial_\alpha h(\mathbf{e}_3 \otimes \boldsymbol{\eta}_\alpha \otimes \mathbf{e}_3). \end{aligned}$$

With similar arguments and Eqs. (2.48) and (2.71), we have

$$\nabla \tilde{\mathbf{q}} = \epsilon (\mathbf{e}_\alpha \otimes \partial_t \boldsymbol{\eta}_\alpha) - \epsilon \partial_t h(\mathbf{e}_3 \otimes \boldsymbol{\tau}) + (1 - \epsilon h) (\mathbf{e}_3 \otimes \partial_t \boldsymbol{\tau})$$

and

$$\begin{aligned} \nabla \hat{\mathbf{v}} \cdot \mathbf{F} &= (\mathbf{e}_i \otimes \partial_i \hat{\mathbf{v}}) \cdot (\mathbf{e}_j \otimes \mathbf{f}_j) \\ &= \epsilon \partial_\alpha (\hat{\mathbf{v}} \cdot \mathbf{e}_\beta) (\mathbf{e}_\alpha \otimes \boldsymbol{\eta}_\beta) + (1 - \epsilon h) \partial_\alpha (\hat{\mathbf{v}} \cdot \mathbf{e}_3) (\mathbf{e}_\alpha \otimes \boldsymbol{\tau}) \\ &\quad + \epsilon \partial_s (\hat{\mathbf{v}} \cdot \mathbf{e}_\beta) (\mathbf{e}_3 \otimes \boldsymbol{\eta}_\beta) + (1 - \epsilon h) \partial_s (\hat{\mathbf{v}} \cdot \mathbf{e}_3) (\mathbf{e}_3 \otimes \boldsymbol{\tau}). \end{aligned}$$

The calculation of all terms of  $\hat{\mathbf{S}}$  need a lot of steps. However, all steps follow the same procedure which is described above. Thus, we omit technical details and just present the outcome of the relevant terms.

By using the definition of  $\mathbf{G}$  given in Eq. (2.52), the computation of the pressure term is straight forward,

$$-\tilde{p}(\mathbf{I} \cdot \mathbf{G}) = -\tilde{p} \left[ \frac{1}{\epsilon} (\boldsymbol{\eta}_\alpha \otimes \mathbf{e}_\alpha) + \frac{1}{(1 - \epsilon h)} (\boldsymbol{\tau} \otimes \mathbf{e}_3) \right]. \quad (2.73)$$

The results for the others terms are

$$\begin{aligned} &((\mathbf{G} \cdot \nabla \hat{\mathbf{v}} \cdot \mathbf{F}) + (\mathbf{G} \cdot \nabla \hat{\mathbf{v}} \cdot \mathbf{F})^T) \cdot \mathbf{G} \\ &= \frac{1}{\epsilon} (\partial_\alpha (\hat{\mathbf{v}} \cdot \mathbf{e}_\beta) + \partial_\beta (\hat{\mathbf{v}} \cdot \mathbf{e}_\alpha)) (\boldsymbol{\eta}_\alpha \otimes \mathbf{e}_\beta) \\ &\quad + \left( \frac{1}{\epsilon} \partial_\alpha (\hat{\mathbf{v}} \cdot \mathbf{e}_3) + \frac{\epsilon}{(1 - \epsilon h)^2} \partial_s (\hat{\mathbf{v}} \cdot \mathbf{e}_\alpha) \right) (\boldsymbol{\eta}_\alpha \otimes \mathbf{e}_3) \\ &\quad + \left( \frac{1}{(1 - \epsilon h)} \partial_s (\hat{\mathbf{v}} \cdot \mathbf{e}_\alpha) + \frac{(1 - \epsilon h)}{\epsilon^2} \partial_\alpha (\hat{\mathbf{v}} \cdot \mathbf{e}_3) \right) (\boldsymbol{\tau} \otimes \mathbf{e}_\alpha) \\ &\quad + \frac{2}{(1 - \epsilon h)} \partial_s (\hat{\mathbf{v}} \cdot \mathbf{e}_3) (\boldsymbol{\tau} \otimes \mathbf{e}_3) \end{aligned} \quad (2.74)$$

and

$$\begin{aligned} & ((\mathbf{G} \cdot \nabla \mathbf{F}^T \cdot \hat{\mathbf{v}}) + (\mathbf{G} \cdot \nabla \mathbf{F}^T \cdot \hat{\mathbf{v}})^T) \cdot \mathbf{G} \\ &= -\frac{2\epsilon}{(1-\epsilon h)^2} ((\hat{\mathbf{v}} \cdot \mathbf{e}_\alpha) \partial_\alpha h + (\hat{\mathbf{v}} \cdot \mathbf{e}_3) \partial_s h) (\boldsymbol{\tau} \otimes \mathbf{e}_3). \end{aligned} \quad (2.75)$$

Due to the fact that  $\partial_t(\boldsymbol{\tau} \otimes \boldsymbol{\tau} + \boldsymbol{\eta}_\alpha \otimes \boldsymbol{\eta}_\alpha) = \mathbf{0}$ , we get

$$((\mathbf{G} \cdot \nabla \tilde{\mathbf{q}}) + (\mathbf{G} \cdot \nabla \tilde{\mathbf{q}})^T) \cdot \mathbf{G} = -\frac{2\epsilon \partial_t h}{(1-\epsilon h)^2} (\boldsymbol{\tau} \otimes \mathbf{e}_3). \quad (2.76)$$

Finally, Eq. (2.60) follows from Eqs. (2.73)-(2.76) and  $J$  given in Eq. (2.51).

Equations (2.66)-(2.68) are the consequence of Assumption 2.2.  $\square$

**Remark 2.8** Note that the unknowns of the fiber problem described by Eqs. (2.57)-(2.68) in the scaled curvilinear coordinate system are  $\hat{\mathbf{v}}, \tilde{\mathbf{v}}, \tilde{p}, \hat{\mathbf{n}}, \hat{w}, \boldsymbol{\gamma}$  and  $L$ . The quantities  $\mathbf{F}, J$  and  $\mathbf{G}$  are associated with the curve  $\boldsymbol{\gamma}$  according to Eqs. (2.49), (2.51) and (2.52).

### 2.5.3 Integration over cross-sections in curvilinear coordinates

For later application, we state special rules for the integration over the cross-sections and its boundary curves. For the formulation we consider scalar, vector or tensor valued functions  $f$  that are differentiable and integrable on  $\mathcal{A}$ . Define

$$\begin{aligned} \langle f \rangle_{\mathcal{A}(s,t)} &= \int_{\mathcal{A}(s,t)} f(x_1, x_2, s, t) dx_1 dx_2 \\ \langle f \rangle_{\partial \mathcal{A}(s,t)} &= \int_{\partial \mathcal{A}(s,t)} \frac{f}{\sqrt{\hat{n}_1^2 + \hat{n}_2^2}} dl, \end{aligned}$$

where  $\hat{\mathbf{n}} = (\hat{n}_1, \hat{n}_2, \hat{n}_3)$  is the unit normal vector to the free surface.

**Theorem 2.3** If  $f$  is a differentiable and integrable function on  $\mathcal{A}$ , then

$$\partial_s \langle f \rangle_{\mathcal{A}(s,t)} = \langle \partial_s f \rangle_{\mathcal{A}(s,t)} - \langle f \hat{n}_3 \rangle_{\partial \mathcal{A}(s,t)} \quad (2.77)$$

and

$$\partial_t \langle f \rangle_{\mathcal{A}(s,t)} = \langle \partial_t f \rangle_{\mathcal{A}(s,t)} + \langle f \hat{w} \rangle_{\partial \mathcal{A}(s,t)}. \quad (2.78)$$

This theorem is already stated in [11] in connection with the asymptotic derivation of a straight fiber. Nevertheless, under our assumptions of a parameterized surface the proof is simple calculus.

**Proof:** Note that the normal vector at the front surfaces, i.e.  $\mathcal{A}(0, t)$  and  $\mathcal{A}(L(t), t)$  are  $-\mathbf{e}_3$  and  $\mathbf{e}_3$ . For the lateral surface of the fiber we consider the parameterization  $\boldsymbol{\xi}$  given in Eq. (2.54).

By using Eq. (2.54), the tangent vectors associated to the coordinates line are

$$\begin{aligned}\partial_\psi \boldsymbol{\xi} &= (-R \sin(\psi) + \partial_\psi R \cos(\psi), R \cos(\psi) + \partial_\psi R \sin(\psi), 0), \\ \partial_s \boldsymbol{\xi} &= (\partial_s R \cos(\psi), \partial_s R \sin(\psi), 1).\end{aligned}$$

The unit normal vector to the free surface introduced in Eq. (2.55) is now given by

$$\hat{\mathbf{n}}(\boldsymbol{\xi}, t) = \frac{\partial_\psi \boldsymbol{\xi} \times \partial_s \boldsymbol{\xi}}{\|\partial_\psi \boldsymbol{\xi} \times \partial_s \boldsymbol{\xi}\|},$$

where

$$\partial_\psi \boldsymbol{\xi} \times \partial_s \boldsymbol{\xi} = (R \cos(\psi) + \partial_\psi R \sin(\psi), R \sin(\psi) - \partial_\psi R \cos(\psi), -R \partial_s R)$$

and

$$\|\partial_\psi \boldsymbol{\xi} \times \partial_s \boldsymbol{\xi}\| = \sqrt{R^2 + (\partial_\psi R)^2 + (R \partial_s R)^2}.$$

The space curve  $\partial \mathcal{A}(s, t)$  for fixed  $t$  and  $s$  belonging to the cross-section  $\mathcal{A}(s, t)$  is parameterized by  $\boldsymbol{\xi}(\cdot, s, t)$ . For the computation of the associated line integral we need

$$\|\partial_\psi \boldsymbol{\xi}\| = \sqrt{R^2 + (\partial_\psi R)^2}.$$

Now, Eq. (2.77) follows directly from the parameterization:

$$\begin{aligned}& \partial_s \left( \int_{\mathcal{A}(s,t)} f dx_1 dx_2 \right) \\ &= \int_0^{2\pi} \partial_s \left( \int_0^{R(\psi, s, t)} f(\varrho \cos(\psi), \varrho \sin(\psi), s) \varrho d\varrho \right) d\psi \\ &= \int_0^{2\pi} \int_0^{R(\psi, s, t)} \partial_s f(\varrho \cos(\psi), \varrho \sin(\psi), s) \varrho d\varrho d\psi \\ &\quad + \int_0^{2\pi} f(R(\psi, s, t) \cos(\psi), R(\psi, s, t) \sin(\psi), s) R(\psi, s, t) \partial_s R(\psi, s, t) d\psi \\ &= \int_{\mathcal{A}(s,t)} \partial_s f dx_1 dx_2 - \int_{\partial \mathcal{A}(s,t)} f \frac{\hat{n}_3}{\sqrt{\hat{n}_1^2 + \hat{n}_2^2}} dl.\end{aligned}$$

Using similar arguments and

$$\hat{w}(\boldsymbol{\xi}, t) = \partial_t \boldsymbol{\xi} \cdot \hat{\mathbf{n}}(\boldsymbol{\xi}, t) = \frac{R \partial_t R}{\sqrt{R^2 + (\partial_\psi R)^2 + (R \partial_s R)^2}},$$

Eq. (2.78) results also directly from the parameterization.  $\square$



**Corollary 2.1** Let  $\mathbf{m}$  and  $\mathbf{M}$  be arbitrary vector and tensor fields that have the same properties as  $f$  in Theorem 2.3, then

$$\langle \nabla \cdot \mathbf{m} \rangle_{\mathcal{A}(s,t)} = \partial_s \langle \mathbf{m} \cdot \mathbf{e}_3 \rangle_{\mathcal{A}(s,t)} + \langle \mathbf{m} \cdot \hat{\mathbf{n}} \rangle_{\partial\mathcal{A}(s,t)} \quad (2.79)$$

$$\langle \nabla \cdot \mathbf{M}^T \rangle_{\mathcal{A}(s,t)} = \partial_s \langle \mathbf{M} \cdot \mathbf{e}_3 \rangle_{\mathcal{A}(s,t)} + \langle \mathbf{M} \cdot \hat{\mathbf{n}} \rangle_{\partial\mathcal{A}(s,t)}. \quad (2.80)$$

**Proof.** The proof results from Gauss Theorem and Theorem 2.3.  $\square$

### 2.5.4 Integrated equations

In the following we integrate the mass and momentum equations over the cross-sections. By using the free surface boundary conditions we are able to derive equations that have already the form of one-dimensional conservation laws. These will play the crucial role in the asymptotic analysis of the one-dimensional fiber model in Section 2.6.

**Theorem 2.4** Suppose the system (2.57)-(2.68) has a solution, then the following relations hold

$$\partial_t \langle J \rangle_{\mathcal{A}(s,t)} + \partial_s \langle J(\hat{\mathbf{v}} \cdot \mathbf{e}_3) \rangle_{\mathcal{A}(s,t)} = 0 \quad (2.81)$$

and

$$\partial_t \langle J\tilde{\mathbf{v}} \rangle_{\mathcal{A}(s,t)} + \partial_s \langle J(\hat{\mathbf{v}} \cdot \mathbf{e}_3)\tilde{\mathbf{v}} \rangle_{\mathcal{A}(s,t)} = \partial_s \langle \hat{\mathbf{S}} \cdot \mathbf{e}_3 \rangle_{\mathcal{A}(s,t)} + \langle \hat{\mathbf{f}} \rangle_{\mathcal{A}(s,t)}. \quad (2.82)$$

**Proof:** The proof follows directly from integration of Eqs. (2.57) and (2.58) over the cross-sections and the free boundary conditions Eqs. (2.61) and (2.62) under regard of Theorem 2.3 and Corollary 2.1.  $\square$

## 2.6 Asymptotic analysis

In this section we state a family of three-dimensional fiber systems corresponding to the slenderness parameter  $\epsilon$ , cf. Eq. (2.19). We use a regular asymptotic expansion for the free boundary value problem. In particular, we generalize the asymptotic method of [11] to derive the one-dimensional model for the curved fiber. Its closure is thereby deduced from the integrated Eqs. (2.81) and (2.82).

### 2.6.1 Family of problems

To carry out the asymptotic analysis of the given fiber problem we first embed our problem with fixed slenderness parameter  $\epsilon = \epsilon_0$  in a family of self-similar problems corresponding to parameters  $\epsilon < \epsilon_0$ , see Fig. 2.6.1. For this family we choose a fixed inflow domain in the scaled coordinates, i.e.  $\mathcal{A}_\epsilon(0, t) = \mathcal{A}(0, t)$  as well as a fixed inflow velocity  $\tilde{\mathbf{v}}_{in}$ . Additionally, we assume the initial position and initial direction of the center-line to be fixed. We rewrite here once more the full set of equations with the index  $\epsilon$  for all variables depending on the slenderness parameter  $\epsilon$ .

*Conservation of mass and momentum,  $\mathbf{x} \in \hat{\Omega}_\epsilon(t)$*

$$\partial_t J_\epsilon(\mathbf{x}, t) + \nabla \cdot (J_\epsilon \hat{\mathbf{v}}_\epsilon)(\mathbf{x}, t) = 0 \quad (2.83)$$

$$\partial_t (J_\epsilon \tilde{\mathbf{v}}_\epsilon)(\mathbf{x}, t) + \nabla \cdot (J_\epsilon \hat{\mathbf{v}}_\epsilon \otimes \tilde{\mathbf{v}}_\epsilon)(\mathbf{x}, t) = \nabla \cdot \hat{\mathbf{S}}_\epsilon^T(\mathbf{x}, t) + \hat{\mathbf{f}}_\epsilon(\mathbf{x}, t) \quad (2.84)$$

*Coupling condition*

$$\hat{\mathbf{v}}_\epsilon(\mathbf{x}, t) = ((\tilde{\mathbf{v}}_\epsilon - \tilde{\mathbf{q}}_\epsilon) \cdot \mathbf{G}_\epsilon)(\mathbf{x}, t) \quad (2.85)$$

*Constitutive law*

$$\begin{aligned} \hat{\mathbf{S}}_\epsilon = & -\tilde{p}_\epsilon [\epsilon(1 - \epsilon h_\epsilon)(\boldsymbol{\eta}_{\alpha, \epsilon} \otimes \mathbf{e}_\alpha) + \epsilon^2(\boldsymbol{\tau}_\epsilon \otimes \mathbf{e}_3)] \\ & + \frac{1}{\text{Re}} [\epsilon(1 - \epsilon h_\epsilon) (\partial_\alpha(\hat{\mathbf{v}}_\epsilon \cdot \mathbf{e}_\beta) + \partial_\beta(\hat{\mathbf{v}}_\epsilon \cdot \mathbf{e}_\alpha)) (\boldsymbol{\eta}_{\alpha, \epsilon} \otimes \mathbf{e}_\beta) \\ & + (\epsilon(1 - \epsilon h_\epsilon) \partial_\alpha(\hat{\mathbf{v}}_\epsilon \cdot \mathbf{e}_3) + \frac{\epsilon^3}{(1 - \epsilon h_\epsilon)} \partial_s(\hat{\mathbf{v}}_\epsilon \cdot \mathbf{e}_\alpha)) (\boldsymbol{\eta}_{\alpha, \epsilon} \otimes \mathbf{e}_3) \\ & + (\epsilon^2 \partial_s(\hat{\mathbf{v}}_\epsilon \cdot \mathbf{e}_\alpha) + (1 - \epsilon h_\epsilon)^2 \partial_\alpha(\hat{\mathbf{v}}_\epsilon \cdot \mathbf{e}_3)) (\boldsymbol{\tau}_\epsilon \otimes \mathbf{e}_\alpha) \\ & + (2 \epsilon^2 \partial_s(\hat{\mathbf{v}}_\epsilon \cdot \mathbf{e}_3) - \frac{2 \epsilon^3}{(1 - \epsilon h_\epsilon)} (\partial_t h_\epsilon + (\hat{\mathbf{v}}_\epsilon \cdot \mathbf{e}_\alpha) \partial_\alpha h_\epsilon + (\hat{\mathbf{v}}_\epsilon \cdot \mathbf{e}_3) \partial_s h_\epsilon)) (\boldsymbol{\tau}_\epsilon \otimes \mathbf{e}_3)] \end{aligned} \quad (2.86)$$

*Kinematic and dynamic boundary conditions (lateral surface),  $\mathbf{x} \in \hat{\Gamma}_{lat, \epsilon}(t)$*

$$(\hat{\mathbf{v}}_\epsilon \cdot \hat{\mathbf{n}}_\epsilon)(\mathbf{x}, t) = \hat{w}_\epsilon(\mathbf{x}, t) \quad (2.87)$$

$$(\hat{\mathbf{S}}_\epsilon \cdot \hat{\mathbf{n}}_\epsilon)(\mathbf{x}, t) = \mathbf{0} \quad (2.88)$$

*Kinematic and dynamic boundary conditions (bottom surf.),  $\mathbf{x} \in \mathcal{A}_\epsilon(L_\epsilon(t), t) \times \{L_\epsilon(t)\}$*

$$\frac{dL_\epsilon(t)}{dt} = (\hat{\mathbf{v}}_\epsilon \cdot \mathbf{e}_3)(\mathbf{x}, t) \quad \text{with} \quad L_\epsilon(0) = 0 \quad (2.89)$$

$$(\hat{\mathbf{S}}_\epsilon \cdot \mathbf{e}_3)(\mathbf{x}, t) = \mathbf{0} \quad (2.90)$$

Inflow boundary condition,  $\mathbf{x} \in \mathcal{A}(0, t) \times \{0\}$

$$\tilde{\mathbf{v}}_\epsilon(\mathbf{x}, t) = \tilde{\mathbf{v}}_{in}(\mathbf{x}) \quad (2.91)$$

Arc-length parameterization

$$\|\partial_s \gamma_\epsilon\| = 1 \quad (2.92)$$

Initial position and direction

$$\gamma_\epsilon(0, t) = \gamma_0 \quad \text{and} \quad \partial_s \gamma_\epsilon(0, t) = \boldsymbol{\tau}_0 \quad (2.93)$$

Center-line condition

$$\int_{\mathcal{A}_\epsilon(s, t)} x_1 dx_1 dx_2 = \int_{\mathcal{A}_\epsilon(s, t)} x_2 dx_1 dx_2 = 0. \quad (2.94)$$

## 2.6.2 Asymptotic expansions

The unknowns in the family of problems of Eqs. (2.83)-(2.94) are the quantities associated with the geometry and the field variables that have to be expanded. In general, the asymptotic expansion of the equations of the free boundary value problem is a difficult task in the sense that the domain (geometry) itself depends on the small parameter  $\epsilon$ . However, we overcome this problem in the following way. We extend all field quantities on the domain  $\cup_{\epsilon < \epsilon_0} \hat{\Omega}_\epsilon$  and assume that their restrictions on  $\hat{\Omega}_\epsilon$  are solutions of the respective  $\epsilon$ -problem.

By Remark 2.7, we are able to describe the fiber domain by three quantities: the fiber length  $L_\epsilon$ , the center-line curve  $\gamma_\epsilon$  and the radius function  $R_\epsilon$ . We assume that these three quantities have regular power series expansions in  $\epsilon$ , i.e.

$$\begin{aligned} L_\epsilon(t) &= L^{(0)}(t) + \epsilon L^{(1)}(t) + o(\epsilon^2) \\ \gamma_\epsilon(s, t) &= \gamma^{(0)}(s, t) + \epsilon \gamma^{(1)}(s, t) + o(\epsilon^2) \\ R_\epsilon(\psi, s, t) &= R^{(0)}(\psi, s, t) + \epsilon R^{(1)}(\psi, s, t) + o(\epsilon^2) \end{aligned}$$

for  $s \in [0, \max_{\epsilon < \epsilon_0} L_\epsilon(t))$ , and  $\psi \in [0, 2\pi)$ .

Based on the assumption of the regular expansions for  $L_\epsilon$ ,  $\gamma_\epsilon$  and  $R_\epsilon$ , the parameterized free surface  $\boldsymbol{\xi}_\epsilon$  and the quantities associated with  $\gamma_\epsilon$ , i.e.  $\boldsymbol{\tau}_\epsilon, \boldsymbol{\eta}_{\alpha, \epsilon}, h_\epsilon, J_\epsilon$  and  $\tilde{\mathbf{q}}_\epsilon$ , can be also expanded in regular power.

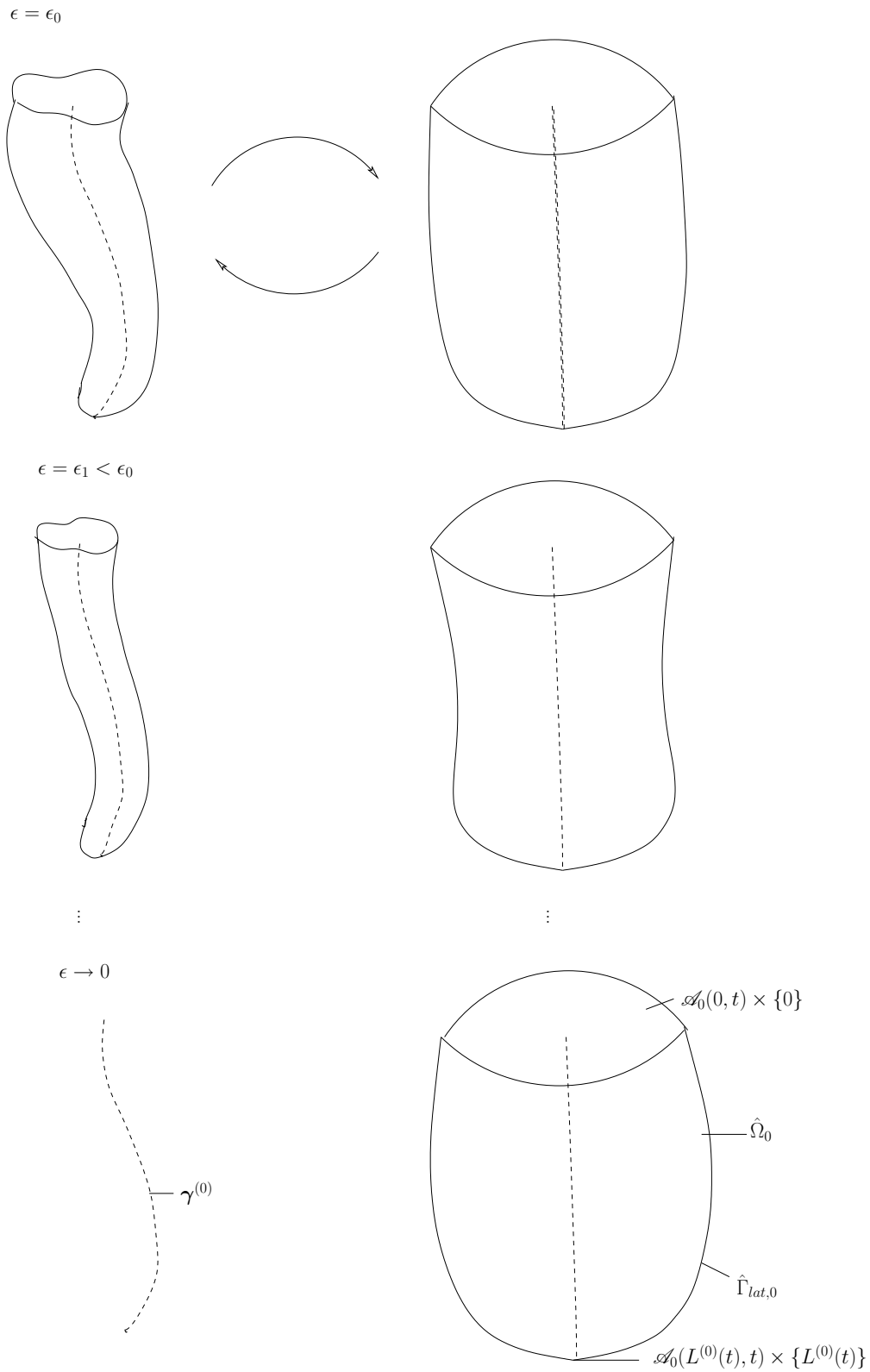


Figure 2.3: Sketch of the family of problems. Left: Real thinning procedure for  $\epsilon \rightarrow 0$ , Right: Scaled problems.

To complete the asymptotics, we expand also the field variables  $\tilde{\mathbf{v}}_\epsilon$  and  $\tilde{p}_\epsilon$  – to be more precise their extended versions – as regular power series in  $\epsilon$ , i.e.

$$\begin{aligned}\tilde{\mathbf{v}}_\epsilon(\mathbf{x}, t) &= \tilde{\mathbf{v}}^{(0)}(\mathbf{x}, t) + \epsilon \tilde{\mathbf{v}}^{(1)}(\mathbf{x}, t) + o(\epsilon^2) \\ \tilde{p}_\epsilon(\mathbf{x}, t) &= \tilde{p}^{(0)}(\mathbf{x}, t) + \epsilon \tilde{p}^{(1)}(\mathbf{x}, t) + o(\epsilon^2)\end{aligned}$$

for  $\mathbf{x} \in \cup_{\epsilon < \epsilon_0} \hat{\Omega}_\epsilon(t)$ .

The regularity assumptions for  $\tilde{\mathbf{v}}_\epsilon$  and  $\tilde{\mathbf{q}}_\epsilon$  and Eq. (2.85) lead to a regular expansion for  $\hat{\mathbf{v}}_\epsilon$ . But in this case, it must start from the  $\epsilon^{-1}$  term, since the lowest order term of  $\mathbf{G}_\epsilon$  is of order  $\epsilon^{-1}$ , i.e.

$$\hat{\mathbf{v}}_\epsilon(\mathbf{x}, t) = \epsilon^{-1} \hat{\mathbf{v}}^{(-1)}(\mathbf{x}, t) + \hat{\mathbf{v}}^{(0)}(\mathbf{x}, t) + \epsilon \hat{\mathbf{v}}^{(1)}(\mathbf{x}, t) + o(\epsilon^2)$$

for  $\mathbf{x} \in \cup_{\epsilon < \epsilon_0} \hat{\Omega}_\epsilon(t)$ . Because of  $\mathbf{G}_\epsilon$  we have,

$$\hat{v}_3^{(-1)} = (\hat{\mathbf{v}}^{(-1)} \cdot \mathbf{e}_3) = 0. \quad (2.95)$$

Furthermore, also the other components  $\hat{v}_1^{(-1)}$  and  $\hat{v}_2^{(-1)}$  will vanish as we will see later.

Before analyzing the family of problems asymptotically, we first consider the asymptotic expansions of the boundary conditions. By using the relations given in Eq. (2.55) for the normal vector and surface speed, the expansions of Eqs. (2.87) and (2.88) are as follows,

$$\begin{aligned}0 &= (\hat{\mathbf{v}}^{(-1)}(\boldsymbol{\xi}^{(0)}, t) + \epsilon (\hat{\mathbf{v}}^{(0)}(\boldsymbol{\xi}^{(0)}, t) + \boldsymbol{\xi}^{(1)} \cdot \nabla \hat{\mathbf{v}}^{(-1)}(\boldsymbol{\xi}^{(0)}, t) - \partial_t \boldsymbol{\xi}^{(0)})) \cdot (\partial_\psi \boldsymbol{\xi}^{(0)} \times \partial_s \boldsymbol{\xi}^{(0)}) \\ &\quad + \epsilon \hat{\mathbf{v}}^{(-1)}(\boldsymbol{\xi}^{(0)}, t) \cdot (\partial_\psi \boldsymbol{\xi}^{(0)} \times \partial_s \boldsymbol{\xi}^{(1)} + \partial_\psi \boldsymbol{\xi}^{(1)} \times \partial_s \boldsymbol{\xi}^{(0)}) + o(\epsilon^2)\end{aligned} \quad (2.96)$$

and

$$\begin{aligned}\mathbf{0} &= (\hat{\mathbf{S}}^{(0)}(\boldsymbol{\xi}^{(0)}, t) + \epsilon (\hat{\mathbf{S}}^{(1)}(\boldsymbol{\xi}^{(0)}, t) + \boldsymbol{\xi}^{(1)} \cdot \nabla \hat{\mathbf{S}}^{(0)}(\boldsymbol{\xi}^{(0)}, t))) \cdot (\partial_\psi \boldsymbol{\xi}^{(0)} \times \partial_s \boldsymbol{\xi}^{(0)}) \\ &\quad + \epsilon \hat{\mathbf{S}}^{(0)}(\boldsymbol{\xi}^{(0)}, t) \cdot (\partial_\psi \boldsymbol{\xi}^{(0)} \times \partial_s \boldsymbol{\xi}^{(1)} + \partial_\psi \boldsymbol{\xi}^{(1)} \times \partial_s \boldsymbol{\xi}^{(0)}) + o(\epsilon^2)\end{aligned} \quad (2.97)$$

for  $\psi \in [0, 2\pi)$  and  $s \in [0, L^{(0)}(t))$ .

**Remark 2.9** It makes no sense to look for the asymptotic expansion of the sets  $\hat{\Omega}_\epsilon(t)$ ,  $\hat{\Gamma}_{lat, \epsilon}(t)$  and  $\mathcal{A}_\epsilon(s, t)$ . However, the limit  $\epsilon \rightarrow 0$  exists. In the limit case we denote the fiber domain by  $\hat{\Omega}_0(t)$ , the lateral surface by  $\hat{\Gamma}_{lat, 0}(t)$  and cross-sections by  $\mathcal{A}_0(s, t)$ . The corresponding normal vector and the surface speed are given by

$$\hat{\mathbf{n}}_0(\boldsymbol{\xi}^{(0)}, t) = \frac{\partial_\psi \boldsymbol{\xi}^{(0)} \times \partial_s \boldsymbol{\xi}^{(0)}}{\| \partial_\psi \boldsymbol{\xi}^{(0)} \times \partial_s \boldsymbol{\xi}^{(0)} \|} \quad \text{and} \quad \hat{w}_0(\boldsymbol{\xi}^{(0)}, t) = \boldsymbol{\xi}^{(0)} \cdot \hat{\mathbf{n}}_0(\boldsymbol{\xi}^{(0)}, t).$$

**Assumption 2.3** We assume now that the fields being defined on  $\cup_{\epsilon < \epsilon_0} \hat{\Omega}_\epsilon$  fulfill the conservation laws on  $\hat{\Omega}_0$  with the prescribed constitutive relation.

In the following we work out the expansion of the fields in  $\hat{\Omega}_0$  always.

### 2.6.3 Lateral problem

For the asymptotic analysis of the full set of Eqs. (2.83)- (2.94) we first consider the so-called lateral problem Eqs. (2.83)-(2.88) and (2.94). We will focus on this problem in the 0th and 1st-order and its closure condition. This work will result in the conservation law of the 1D model. The derivation of the appropriate constraints as well as boundary and initial conditions is done in a second step based on the remaining equations of the family problem.

#### 2.6.3.1 0th-order

We calculate the 0th-order stress tensor using Eq. (2.86)

$$\hat{\mathbf{S}}^{(0)} = \frac{1}{\text{Re}} [(\partial_\alpha \hat{v}_\beta^{(-1)} + \partial_\beta \hat{v}_\alpha^{(-1)}) (\boldsymbol{\eta}_\alpha^{(0)} \otimes \mathbf{e}_\beta) + (\partial_\alpha \hat{v}_3^{(0)}) (\boldsymbol{\tau}^{(0)} \otimes \mathbf{e}_\alpha)] \quad (2.98)$$

Using this result of Eq. (2.98) and skipping for the moment the conservation of mass in Eq. (2.83), we obtain from Eqs. (2.84),(2.85),(2.87),(2.88) and (2.94) the leading order equations of the lateral problem.

*Momentum equation,  $\mathbf{x} \in \hat{\Omega}_0(t)$*

$$\left( \partial_{\alpha\beta} \hat{v}_\beta^{(-1)} + \partial_{\beta\alpha} \hat{v}_\alpha^{(-1)} \right) \boldsymbol{\eta}_\alpha^{(0)} + (\partial_{\alpha\alpha} \hat{v}_3^{(0)}) \boldsymbol{\tau}^{(0)} = \mathbf{0} \quad (2.99)$$

*Coupling condition*

$$\tilde{\mathbf{v}}^{(0)} = \hat{v}_\alpha^{(-1)} \boldsymbol{\eta}_\alpha^{(0)} + \hat{v}_3^{(0)} \boldsymbol{\tau}^{(0)} + \partial_t \boldsymbol{\gamma}^{(0)} \quad (2.100)$$

*Kinematic and dynamic boundary conditions,  $\mathbf{x} \in \hat{\Gamma}_{lat,0}(t)$*

$$\hat{v}_\alpha^{(-1)} \hat{n}_{0,\alpha} = 0 \quad (2.101)$$

$$(\partial_\alpha \hat{v}_\beta^{(-1)} + \partial_\beta \hat{v}_\alpha^{(-1)}) \hat{n}_{0,\beta} \boldsymbol{\eta}_\alpha^{(0)} + \partial_\alpha \hat{v}_3^{(0)} \hat{n}_{0,\alpha} \boldsymbol{\tau}^{(0)} = \mathbf{0} \quad (2.102)$$

*Center-line condition*

$$\int_{\mathcal{A}_0(s,t)} x_1 dx_1 dx_2 = \int_{\mathcal{A}_0(s,t)} x_2 dx_1 dx_2 = 0 \quad (2.103)$$

**Proposition 2.1** Any solution of the 0th-order lateral problem Eqs. (2.99)- (2.103) satisfies:

$$\hat{v}_1^{(-1)} = \hat{v}_2^{(-1)} \equiv 0 \quad (2.104)$$

$$\hat{v}_3^{(0)} = \hat{v}_3^{(0)}(s, t). \quad (2.105)$$

**Proof:** After multiplying Eqs. (2.99) and (2.102) with  $\boldsymbol{\tau}^{(0)}$ , we have the following problem for  $\hat{v}_3^{(0)}$ , i.e.

$$\partial_{11}\hat{v}_3^{(0)} + \partial_{22}\hat{v}_3^{(0)} = 0$$

for  $\mathbf{x} \in \hat{\Omega}_0(t)$  and

$$\partial_1\hat{v}_3^{(0)}\hat{n}_{0,1} + \partial_2\hat{v}_3^{(0)}\hat{n}_{0,2} = 0$$

for  $\mathbf{x} \in \hat{\Gamma}_{lat,0}(t)$ .

This problem is solved by a constant  $\hat{v}_3^{(0)}$  for each cross-section. Altogether  $\hat{v}_3^{(0)}$  spatially depends only on  $s$ , i.e.

$$\hat{v}_3^{(0)} = \hat{v}_3^{(0)}(s, t).$$

This yields Eq. (2.105).

Again, by multiplying Eqs. (2.99) and (2.102) with  $\boldsymbol{\eta}_{1,2}^{(0)}$ , we obtain

$$\begin{aligned} 2\partial_{11}\hat{v}_1^{(-1)} + \partial_2(\partial_1\hat{v}_2^{(-1)} + \partial_2\hat{v}_1^{(-1)}) &= 0 \\ \partial_1(\partial_1\hat{v}_2^{(-1)} + \partial_2\hat{v}_1^{(-1)}) + 2\partial_{22}\hat{v}_2^{(-1)} &= 0 \end{aligned} \quad (2.106)$$

for  $\mathbf{x} \in \hat{\Omega}_0(t)$  and

$$\begin{aligned} 2\partial_1\hat{v}_1^{(-1)}\hat{n}_{0,1} + (\partial_1\hat{v}_2^{(-1)} + \partial_2\hat{v}_1^{(-1)})\hat{n}_{0,2} &= 0 \\ (\partial_1\hat{v}_2^{(-1)} + \partial_2\hat{v}_1^{(-1)})\hat{n}_{0,1} + 2\partial_2\hat{v}_2^{(-1)}\hat{n}_{0,2} &= 0 \end{aligned} \quad (2.107)$$

for  $\mathbf{x} \in \hat{\Gamma}_{lat,0}(t)$ .

Equations (2.106) and (2.107) describe a two-dimensional zero-boundary stress Stokes flow problem. The solution of this problem is given by

$$\begin{aligned} \hat{v}_1^{(-1)} &= -c(s, t)x_2 + d_1(s, t) \\ \hat{v}_2^{(-1)} &= c(s, t)x_1 + d_2(s, t), \end{aligned} \quad (2.108)$$

where  $c(s, t)$ ,  $d_1(s, t)$  and  $d_2(s, t)$  are arbitrary constants. To find these constants, we proceed as follows.

By integrating the kinematic condition Eq. (2.101) over the boundary of the cross-section  $\partial\mathcal{A}_0$ , it follows that

$$\int_{\partial\mathcal{A}_0(s,t)} (\hat{v}_1^{(-1)}\hat{n}_{0,1} + \hat{v}_2^{(-1)}\hat{n}_{0,2}) \frac{x_1}{\sqrt{(\hat{n}_{0,1})^2 + (\hat{n}_{0,2})^2}} dl = 0. \quad (2.109)$$

Applying the divergence theorem and using Eq. (2.108), we get

$$\int_{\mathcal{A}_0(s,t)} (\hat{v}_1^{(-1)}) dx_1 dx_2 = 0. \quad (2.110)$$

By using again Eq. (2.108) and the center-line condition Eq. (2.103), we obtain  $d_1 = 0$ . Similarly, one can show that  $d_2 = 0$ .

Again, the kinematic condition at this leading order Eq. (2.101) produces two possibilities: either the constant  $c$  is zero or the free surface is a circular cross-section profile. However, any slight perturbations at the nozzle will destroy the circular cross-section profile of the surface. This leads to the conclusion that  $c$  has to be zero.  $\square$

**Corollary 2.2** As a direct consequence of the Proposition 2.1 we can state for the 0th-order lateral problem

$$\tilde{\mathbf{v}}^{(0)} = \hat{v}_3^{(0)} \boldsymbol{\tau}^{(0)} + \partial_t \boldsymbol{\gamma}^{(0)}. \quad (2.111)$$

$$\hat{\mathbf{S}}^{(0)} = \mathbf{0}. \quad (2.112)$$

Equation (2.111) especially means that  $\tilde{\mathbf{v}}^{(0)} = \tilde{\mathbf{v}}^{(0)}(s, t)$  as well as  $\hat{v}_3^{(0)} = \hat{v}_3^{(0)}(s, t)$  are constant in the cross-sections. Up to now, we did not consider the conservation of mass in the 0th-order. This reads  $\partial_\alpha \hat{\mathbf{v}}_\alpha^{(-1)} = 0$  and is automatically fulfilled.

### 2.6.3.2 1st-order

Applying the results of the 0th-order analysis, the 1st-order stress tensor is given by

$$\hat{\mathbf{S}}^{(1)} = -\tilde{p}^{(0)}(\boldsymbol{\eta}_\alpha^{(0)} \otimes \mathbf{e}_\alpha) + \frac{1}{\text{Re}} [(\partial_\alpha \hat{v}_\beta^{(0)} + \partial_\beta \hat{v}_\alpha^{(0)})(\boldsymbol{\eta}_\alpha^{(0)} \otimes \mathbf{e}_\beta) + \partial_\alpha \hat{v}_3^{(1)}(\boldsymbol{\tau}^{(0)} \otimes \mathbf{e}_\alpha)]. \quad (2.113)$$

Using this and the results of 0th-order we consider Eqs. (2.83),(2.84),(2.87) and (2.88) in the 1st-order. We skip Eq. (2.85) because Eq. (2.111) is already the final result with respect to the coupling of velocities. For technical reasons we again have to take into account the center-line condition for  $\epsilon \rightarrow 0$ . In this sense the first order lateral problem reads on  $\hat{\Omega}_0$

*Conservation of mass and momentum,  $\mathbf{x} \in \hat{\Omega}_0(t)$*

$$\partial_\alpha \hat{v}_\alpha^{(0)} + \partial_s \hat{v}_3^{(0)} = 0 \quad (2.114)$$

$$\left( \partial_{\alpha\beta} \hat{v}_\beta^{(0)} + \partial_{\beta\beta} \hat{v}_\alpha^{(0)} - \text{Re } \partial_\alpha \tilde{p}^{(0)} \right) \boldsymbol{\eta}_\alpha^{(0)} + \partial_{\alpha\alpha} \hat{v}_3^{(1)} \boldsymbol{\tau}^{(0)} = \mathbf{0} \quad (2.115)$$

*Kinematic and dynamic boundary conditions,  $\mathbf{x} \in \hat{\Gamma}_{lat,0}(t)$*

$$\hat{\mathbf{v}}^{(0)} \cdot \hat{\mathbf{n}}_0 = \hat{w}_0 \quad (2.116)$$

$$\left( (\partial_\alpha \hat{v}_\beta^{(0)} + \partial_\beta \hat{v}_\alpha^{(0)}) \hat{n}_{0,\beta} - \text{Re } \tilde{p}^{(0)} \hat{n}_{0,\alpha} \right) \boldsymbol{\eta}_\alpha^{(0)} + \partial_\alpha \hat{v}_3^{(1)} \hat{n}_{0,\alpha} \boldsymbol{\tau}^{(0)} = \mathbf{0} \quad (2.117)$$

*Center-line condition*

$$\int_{\mathcal{A}_0(s,t)} x_1 dx_1 dx_2 = \int_{\mathcal{A}_0(s,t)} x_2 dx_1 dx_2 = 0. \quad (2.118)$$



**Proposition 2.2** Any solution of the 1st-order problem Eqs. (2.114)-(2.118) satisfies

$$\begin{aligned}\hat{v}_1^{(0)} &= \frac{\text{Re}}{2} \tilde{p}^{(0)} x_1 - a(s, t) x_2 \\ \hat{v}_2^{(0)} &= \frac{\text{Re}}{2} \tilde{p}^{(0)} x_2 + a(s, t) x_1 \\ \tilde{p}^{(0)} &= -\frac{1}{\text{Re}} \partial_s \hat{v}_3^{(0)}(s, t) \\ \hat{v}_3^{(1)} &= \hat{v}_3^{(1)}(s, t).\end{aligned}\tag{2.119}$$

The strategy to prove this proposition is similar to the 0th-order problem. Thus, we omit the proof.

**Corollary 2.3** As a direct consequence of the Proposition 2.2 we can state for the stress in 1st-order

$$\hat{\mathbf{S}}^{(1)} = \mathbf{0}.\tag{2.120}$$

### 2.6.3.3 Closure

Now we consider the integrated conservation laws of Eqs. (2.81) and (2.82). In the integrated form of the momentum Eq. (2.82) we do not need to examine all the second order terms from the stress tensor. Instead, we only need to know the stress tensor in the axial direction, i.e.  $\hat{\mathbf{S}}^{(2)} \cdot \mathbf{e}_3$ . By applying the results of the 0th and 1st-order analysis, the 2nd-order stress tensor in the axial direction reads

$$\hat{\mathbf{S}}^{(2)} \cdot \mathbf{e}_3 = \frac{3}{\text{Re}} \partial_3 \hat{v}_3^{(0)} \boldsymbol{\tau}^{(0)}.\tag{2.121}$$

Using Eq. (2.121) and the results of the 0th and 1st-order, the integrated equations (2.81) and (2.82) lead in their lowest non-trivial order directly to the main result of this section:

$$\partial_t | \mathcal{A}_0 | + \partial_s (\hat{v}_3^{(0)} | \mathcal{A}_0 |) = 0\tag{2.122}$$

$$\partial_t (\tilde{\mathbf{v}}^{(0)} | \mathcal{A}_0 |) + \partial_s (\hat{v}_3^{(0)} \tilde{\mathbf{v}}^{(0)} | \mathcal{A}_0 |) = \frac{3}{\text{Re}} \partial_s (\partial_s \hat{v}_3^{(0)} \boldsymbol{\tau}^{(0)} | \mathcal{A}_0 |) + \tilde{\mathbf{f}}^{(0)} | \mathcal{A}_0 |.\tag{2.123}$$

## 2.6.4 Constraints, initial and boundary conditions

The main results for the lateral problem Eqs. (2.122) and (2.123) together with the coupling Eq. (2.111) are already a reasonable set of PDEs. But we still need the constraint with respect to the parameterization of  $\boldsymbol{\gamma}^{(0)}$  as well as appropriate initial and boundary conditions. To derive these conditions we have to consider the remaining

equations of the full problem, i.e. Eqs. (2.89)-(2.93) in the lowest non-trivial order together with the coupling condition Eq. (2.85). To do so, we use the results of the lateral problem, especially the vanishing stress in 0th and 1st-order. This leads to:

*Coupling condition*

$$\tilde{\mathbf{v}}^{(0)}(s, t) = \hat{v}_3^{(0)}(s, t)\boldsymbol{\tau}^{(0)}(s, t) + \partial_t \boldsymbol{\gamma}^{(0)}(s, t) \quad (2.124)$$

*Kinematic and dynamic boundary condition (bottom)*

$$\frac{dL^{(0)}(t)}{dt} = \hat{v}_3^{(0)}(L^{(0)}(t), t) \quad \text{with} \quad L^{(0)}(0) = 0 \quad (2.125)$$

$$\partial_s \hat{v}_3^{(0)}(L(t), t) = 0 \quad (2.126)$$

*Inflow boundary condition*

$$\tilde{\mathbf{v}}^{(0)}(0, t) = \tilde{\mathbf{v}}_{in}(\mathbf{x}) \quad (2.127)$$

*Arc-length parameterization*

$$\| \partial_s \boldsymbol{\gamma}^{(0)} \| = 1 \quad (2.128)$$

*Initial position and direction*

$$\boldsymbol{\gamma}^{(0)}(0, t) = \boldsymbol{\gamma}_0 \quad \text{and} \quad \partial_s \boldsymbol{\gamma}^{(0)}(0, t) = \boldsymbol{\tau}_0 \quad (2.129)$$

**Proposition 2.3** As a consequence of the Eqs. (2.124), (2.127) and (2.129), we have

$$\hat{v}_3^{(0)}(0, t) = 1. \quad (2.130)$$

**Proof.** With Eqs. (2.124) and (2.129), the inflow velocity can be written as

$$\tilde{\mathbf{v}}_{in} = \hat{v}_3^{(0)}(0, t)\boldsymbol{\tau}_0. \quad (2.131)$$

Now, Eq. (2.130) follows from Eq. (2.56).  $\square$

## 2.7 Final asymptotic results

Finally, we summarize the asymptotic results. In order to do this, we define  $u = \hat{v}_3^{(0)}$  and  $A = |\mathcal{A}_0|$ . Moreover, we drop the suffices at the leading order variables. As a consequence of Eqs. (2.122), (2.123), (2.111), (2.128) and (2.125) we get the final asymptotic model for our fiber problem.

*Conservation of mass and momentum,  $s \in [0, L(t)]$*

$$\partial_t A + \partial_s(uA) = 0 \quad (2.132)$$

$$\partial_t(A\tilde{\mathbf{v}}) + \partial_s(uA\tilde{\mathbf{v}}) = \frac{3}{\text{Re}}\partial_s(A\partial_s u\partial_s \boldsymbol{\gamma}) + A\tilde{\mathbf{f}} \quad (2.133)$$

*Coupling condition*

$$\tilde{\mathbf{v}} = u \partial_s \boldsymbol{\gamma} + \partial_t \boldsymbol{\gamma} \quad (2.134)$$

*Arc-length parameterization*

$$\|\partial_s \boldsymbol{\gamma}\| = 1 \quad (2.135)$$

*Evolution of fiber length*

$$\frac{dL(t)}{dt} = u(L(t), t) \quad \text{with} \quad L(0) = 0 \quad (2.136)$$

*Boundary conditions at the nozzle*

$$A(0, t) = 1 \quad \text{and} \quad u(0, t) = 1 \quad (2.137)$$

$$\boldsymbol{\gamma}(0, t) = \boldsymbol{\gamma}_0 \quad \text{and} \quad \partial_s \boldsymbol{\gamma}(0, t) = \boldsymbol{\tau}_0 \quad (2.138)$$

*Boundary condition at the end of the fiber*

$$\partial_s u(L(t), t) = 0 \quad (2.139)$$

The one-dimensional fiber model of Eqs. (2.132)-(2.136) determines the evolution of cross-sectional area  $A(s, t)$ , the intrinsic velocity  $u(s, t)$ , the fiber center-line  $\boldsymbol{\gamma}(s, t)$ , the velocity  $\tilde{\mathbf{v}}(s, t)$  describing the relation between the fluid and the center-line velocity and the fiber length  $L(t)$ . The boundary conditions Eq. (2.137) are deduced from Eq. (2.56) and Proposition 2.3. The fiber position and direction at the nozzle Eq. (2.138) are due to Eq. (2.129). The boundary condition at the end of the fiber Eq. (2.139) is derived from Eq. (2.126).

**Remark 2.10** Our asymptotic result for a Newtonian fluid is consistent with the experimental measurements by Trouton [32] by retaining the factor 3 in Eq. (2.133). In the dimensional form of Eq. (2.133), we retain the factor  $3\mu$  which is the so-called Trouton viscosity.

**Remark 2.11** In the given application problem we have introduced  $\mathbf{f}^*$  as body forces that contain gravitational and rotational forces. Thus, we define the dimensional

$$\mathbf{f}^* = \rho (g \mathbf{e}_g - 2\boldsymbol{\omega} (\mathbf{e}_\omega \times \mathbf{v}^*) - \omega^2 (\mathbf{e}_\omega \times (\mathbf{e}_\omega \times \mathbf{r}^*))) \quad (2.140)$$

as sum of the gravity, coriolis and centrifugal forces. Here,  $\boldsymbol{\omega} = \omega \mathbf{e}_\omega$  denotes the angular velocity of the rotating device and  $\mathbf{g} = g \mathbf{e}_g$  is the acceleration of gravity.

Then, in the asymptotic outcome we have

$$\tilde{\mathbf{f}} = \frac{1}{\text{Fr}^2} \mathbf{e}_g - \frac{2}{\text{Rb}} (\mathbf{e}_\omega \times \tilde{\mathbf{v}}) - \frac{1}{\text{Rb}^2} (\mathbf{e}_\omega \times (\mathbf{e}_\omega \times \boldsymbol{\gamma})),$$

where the typical numbers are

- the dimensionless Froude number  $\text{Fr} = V/\sqrt{gL_0}$  that characterizes the relation between inertial and gravity forces.
- the dimensionless Rossby number  $\text{Rb} = V/L_0\omega$  that characterizes the relation between inertial and rotational forces.

### 2.7.1 Asymptotic model equations in dimensional form

In order to define the asymptotic model equations in the dimensional form, we use the non-dimensional procedure given in the Section 2.3 and introduce additionally  $A^* = |\Gamma_{in}| A$ ,  $\boldsymbol{\gamma}^* = L_0 \boldsymbol{\gamma}$ ,  $s^* = L_0 s$  as well as  $\boldsymbol{\gamma}_0^* = L_0 \boldsymbol{\gamma}_0$ . This yields

*Conservation of mass and momentum,  $s^* \in [0, L^*(t^*)]$*

$$\partial_{t^*} A^* + \partial_{s^*} (u^* A^*) = 0 \quad (2.141)$$

$$\rho (\partial_{t^*} (A^* \tilde{\mathbf{v}}^*) + \partial_{s^*} (u^* A^* \tilde{\mathbf{v}}^*)) = 3\mu \partial_{s^*} (A^* \partial_{s^*} u^* \partial_{s^*} \boldsymbol{\gamma}^*) + A^* \tilde{\mathbf{f}}^* \quad (2.142)$$

*Coupling condition*

$$\tilde{\mathbf{v}}^* = u^* \partial_{s^*} \boldsymbol{\gamma}^* + \partial_{t^*} \boldsymbol{\gamma}^* \quad (2.143)$$

*Arc-length parameterization*

$$\|\partial_{s^*} \boldsymbol{\gamma}^*\| = 1 \quad (2.144)$$

*Evolution of fiber length*

$$\frac{dL^*(t^*)}{dt^*} = u^*(L^*(t^*), t^*) \quad \text{with} \quad L^*(0) = 0 \quad (2.145)$$

*Boundary conditions at the nozzle*

$$A^*(0, t^*) = |\Gamma_{in}| \quad \text{and} \quad u^*(0, t^*) = V \quad (2.146)$$

$$\boldsymbol{\gamma}^*(0, t^*) = \boldsymbol{\gamma}_0^* \quad \text{and} \quad \partial_{s^*} \boldsymbol{\gamma}^*(0, t^*) = \boldsymbol{\tau}_0 \quad (2.147)$$

*Boundary condition at the end of the fiber*

$$\partial_{s^*} u^*(L^*(t^*), t^*) = 0 \quad (2.148)$$

According to Eq. (2.140), the body forces  $\tilde{\mathbf{f}}^*$  in the dimensional form are given by

$$\tilde{\mathbf{f}}^* = \rho \left( g \mathbf{e}_g - 2\omega (\mathbf{e}_\omega \times \tilde{\mathbf{v}}^*) - \omega^2 (\mathbf{e}_\omega \times (\mathbf{e}_\omega \times \boldsymbol{\gamma}^*)) \right) \quad (2.149)$$

Thus, beginning with the full three-dimensional Newtonian viscous free surface boundary value problem, we have derived a one-dimensional model for a slender, Newtonian viscous fiber emerging from the rotating device by the help of slenderness asymptotics. This one-dimensional fiber model is a closed set of nine equations Eqs. (2.141)-(2.145) for the nine variables, i.e.  $A^*$ ,  $u^*$ ,  $\tilde{\mathbf{v}}^*$ ,  $\boldsymbol{\gamma}^*$  and  $L^*$ . The physical effects of inertia, viscosity, gravity and rotation are represented in the fiber model. In the subsequent chapters, we will examine the consequences of the specific one-dimensional model for stationary and time-dependent situations.



# Chapter 3

## Numerical Simulation of the Unsteady Fiber Model

In the previous chapter a one-dimensional model has been derived from the three-dimensional theory with the help of asymptotic method. The present chapter proposes a numerical scheme for the handling of this one-dimensional unsteady fiber model.

It should be mentioned here that the relevant field variables of the one-dimensional asymptotic model depend on time and one space coordinate. Nevertheless, the fiber center-line is a curve in the three-dimensional space. In this chapter, we also look for reduced models, where the center-line is embedded in a two- and one-dimensional space. In this sense we speak about one-, two-, and three-dimensional problem with respect to the center-line of the fiber.

The outline of this chapter is as follows. In the first section we briefly recall the equations of the non-dimensional asymptotic model, that are subject of the analysis. A numerical method for the straight fiber model, which is a special case when the fiber falls only under the gravitational force, is proposed in Section 3.2. An application of the resulting method is then presented. In Section 3.3, the developed numerical scheme is extended to the simulation of fiber dynamics under the influence of rotational forces. Simulation results showing the influence of gravity and rotational forces are presented in Section 3.4. Finally, a summary of the results is given in Section 3.5.

### 3.1 Asymptotic fiber model

The asymptotic fiber model leads to the following system of partial differential equations that describes conservation of mass and momentum

$$\partial_t A(s, t) + \partial_s(uA)(s, t) = 0 \tag{3.1}$$

$$\partial_t(A\tilde{\mathbf{v}})(s, t) + \partial_s(uA\tilde{\mathbf{v}})(s, t) = \frac{3}{\text{Re}}\partial_s(A\partial_s u\partial_s\boldsymbol{\gamma})(s, t) + (\tilde{\mathbf{f}}A)(s, t) \quad (3.2)$$

with the coupling condition

$$\tilde{\mathbf{v}}(s, t) = u(s, t) \partial_s\boldsymbol{\gamma}(s, t) + \partial_t\boldsymbol{\gamma}(s, t) \quad (3.3)$$

and the arc-length constraint

$$\|\partial_s\boldsymbol{\gamma}(s, t)\| = 1. \quad (3.4)$$

Here  $s \in [0, L(t))$  denotes the arc-length parameter and  $t \in \mathbb{R}^+$  is the time variable.

The boundary conditions at the nozzle ( $s = 0$ ) are

$$\begin{aligned} A(0, t) &= A_0, & u(0, t) &= u_0 \\ \boldsymbol{\gamma}(0, t) &= \boldsymbol{\gamma}_0, & \partial_s\boldsymbol{\gamma}(0, t) &= \boldsymbol{\tau}_0 \end{aligned} \quad (3.5)$$

and the end of the fiber ( $s = L(t)$ ) is prescribed to be stress-free, i.e.

$$\partial_s u(L(t), t) = 0. \quad (3.6)$$

Additionally, we have the evolution of the fiber length given by

$$\frac{dL(t)}{dt} = u(L(t), t) \quad \text{and} \quad L(0) = 0. \quad (3.7)$$

The non-dimensional body forces are

$$\tilde{\mathbf{f}}(s, t) = \frac{1}{\text{Fr}^2} \mathbf{e}_g - \frac{2}{\text{Rb}} (\mathbf{e}_\omega \times \tilde{\mathbf{v}}) - \frac{1}{\text{Rb}^2} (\mathbf{e}_\omega \times (\mathbf{e}_\omega \times \boldsymbol{\gamma})). \quad (3.8)$$

The symbols  $A(s, t)$ ,  $u(s, t)$  and  $\boldsymbol{\gamma}(s, t)$  denote the cross-sectional area of the fiber, the fluid velocity and the center-line of the fiber in the position  $s$  at time  $t$ , respectively. Here  $\tilde{\mathbf{f}}(s, t)$  represents the body forces which include the force of gravity and the rotational forces in the position  $s$  at time  $t$ . The velocity  $\tilde{\mathbf{v}}$  describes the relation between the fluid  $u$  and the center-line velocity  $\partial_t\boldsymbol{\gamma}$ . The symbol  $L(t)$  stands for the fiber length at time  $t$ .

Here, two new symbols  $A_0$  and  $u_0$  have been introduced in Eq. (3.5) for later convenience. Throughout this chapter they are simply equal to  $A_0 = 1$  and  $u_0 = 1$ .

For our computational purpose we set the configuration shown in Fig. 3.1 for the rotating device. We consider that the device rotates in the anticlockwise direction along the vector  $\mathbf{e}_2$  and the force of gravitation acts in the downward direction. In this case the vectors  $\mathbf{e}_g$  and  $\mathbf{e}_\omega$  of Eq. (3.8) are equal to  $\mathbf{e}_g = (0, -1, 0)$  and  $\mathbf{e}_\omega = (0, 1, 0)$ . By considering the characteristic length to be the radius of the rotating device and fixing origin at the center of the device, the non-dimensional fiber position at the



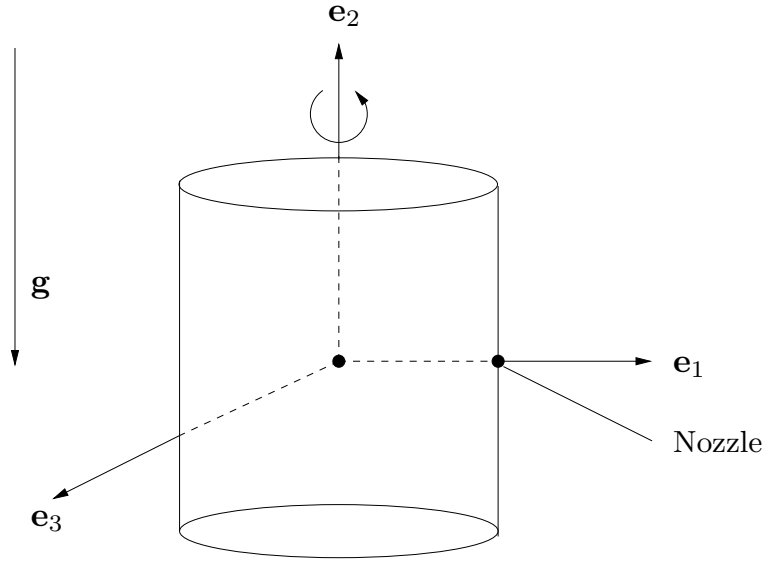


Figure 3.1: Schematic diagram of the device showing the directions of rotation and gravity.

nozzle  $\gamma_0 = (1, 0, 0)$ . For the tangent vector of the center-line at the nozzle we set  $\tau_0 = (1, 0, 0)$ .

The dimensionless parameters in these equations are the Reynolds number  $Re$ , the Froude number  $Fr$  and the Rossby number  $Rb$ , which respectively parameterize viscous, gravity and rotational forces with respect to inertia. The choice of scales and definitions of all non-dimensional parameters is given in Chapter 2. The task is now to solve Eqs. (3.1)-(3.4) with the boundary and initial conditions Eqs. (3.5)-(3.7). We shall do this numerically but in the following section we first study a special case where the fiber moves only under the influence of gravitational force. The influence of rotational forces is discussed in Section 3.3.

## 3.2 Straight fiber (Special case)

Before solving the model Eqs. (3.1)-(3.8), we first analyze numerically a simpler case by neglecting the rotational forces. As a consequence,  $\mathbf{e}_\omega$  of Eq. (3.8) is the zero vector and the fiber will fall under the action of the gravitational force only. Hence,  $\tilde{\mathbf{f}} = (1/Fr^2) \mathbf{e}_g$ . Since gravity acts perpendicular to the direction of the flow (see Fig. 3.1), the three-dimensional problem with respect to the center-line  $\gamma$  has now been reduced to a two-dimensional problem. We simplify the problem even further by assuming  $\mathbf{e}_g = \mathbf{e}_1 = (1, 0, 0)$ . In this case the center-line of the fiber is straight, i.e.  $\partial_s \gamma = \mathbf{e}_1$ . Now, the coupling condition leads to  $\tilde{\mathbf{v}} = u \mathbf{e}_1$ . Thus, finally the model is reduced to one-dimensional one with respect to the center-line  $\gamma$ . Notice, that this

simplified assumptions have no influence on the type of the governing equations. The arc-length constraint (3.4) is automatically satisfied and the coupling condition (3.3) is no more needed.

Using the above mentioned assumptions the non-dimensional asymptotic model for the straight fiber consists of mass and momentum equations and is given by

$$\partial_t A(s, t) + \partial_s(uA)(s, t) = 0, \quad s \in [0, L(t)] \quad (3.9)$$

$$\partial_t(Au)(s, t) + \partial_s(uAu)(s, t) = \frac{3}{\text{Re}} \partial_s(A \partial_s u)(s, t) + \frac{1}{\text{Fr}^2} A(s, t), \quad s \in [0, L(t)] \quad (3.10)$$

The boundary conditions at the nozzle are

$$A(0, t) = A_0, \quad u(0, t) = u_0 \quad (3.11)$$

and at the end of the fiber

$$\partial_s u(L(t), t) = 0, \quad (3.12)$$

$$\text{with } \frac{dL(t)}{dt} = u(L(t), t), \quad L(0) = 0. \quad (3.13)$$

This reduced system described by Eqs. (3.9)-(3.10) has been studied so far by many authors. Ignoring the effect of fluid inertia and gravity, this system has been investigated in [9], with a focus on the production of fibers by a tapering process. In the context of a thermal glass drawing process, this system including the effect of temperature and surface tension has been analyzed in [18]. In this work, the unsteady process is discussed on a fixed length of fiber by varying the inflow boundary condition. Recently a similar problem in connection with the dripping of honey under gravity has been described in [30, 31]. The Stokes and Navier-Stokes equations are solved in this work by using a finite element method. Moreover, the slender drop approximation in Lagrange coordinates is also used and solved numerically in [30]. The last work is very similar to our present simplified problem. However, our approach to tackle this free boundary value problem is different since we will solve the approximated model in a Eulerian formulation by using a finite volume method on a non-uniform grid.

**Remark 3.1** In the framework of the model, the cross-sectional area is always constant at the end of the fiber. This can be seen analytically as follows:

By using Eq. (3.12), the conservation of mass Eq. (3.9) at  $s = L(t)$  yields

$$\partial_t A(L(t), t) + (u \partial_s A)(L(t), t) = 0. \quad (3.14)$$

By using Eq. (3.13), Eq. (3.14) can be re-written as follows

$$\frac{d}{dt} A(L(t), t) = 0, \quad (3.15)$$

or, equivalently, by introducing  $A_{end}(t) := A(L(t), t)$

$$A_{end} = A_0 = 1, \quad (3.16)$$

where  $A_0$  is the non-dimensional cross-sectional area at the nozzle  $s = 0$ .

Equation (3.15) means that the cross section at the end of the fiber is constant. This surprising result is a consequence of the stress-free boundary condition. Therefore, we expect that the consideration of surface tension in the model will produce more reasonable results.

Additionally, the initialization of our problem with  $L(0) = 0$  and  $A_0 = 1$  produces  $A_{end} = 1$ . In contradiction to this results, one should expect in the real spinning process a decreasing cross section along the fiber. Of course numerical simulations of the model in the subsequent sections produce the result  $A_{end} = 1$ . Nevertheless, we will see that for a long fibers, the cross-sectional area is decreasing up to a small boundary layer at the end of the fiber. Moreover, by numerical tests we observe that a change of the initialization, e.g.  $A_{end}(0) = 0$ , will end up in a change of this boundary layer, but do not influences the dynamical behavior of the fiber.

Finally, we want to solve the straight fiber problem numerically. In the following, we will define a numerical scheme for the solution of the problem. Numerical results and convergence analysis are discussed in the subsequent subsections.

### 3.2.1 Numerical scheme for the straight fiber problem

Before proceeding with numerics, let us first introduce some notations. We introduce an auxiliary variable  $v = Au$  and the following vector of the primitive variables

$$\boldsymbol{\psi}_s = (A, v).$$

The index 's' is chosen here to specify the notations of the straight fiber problem. The index 'c' will be used later in the curved fiber problem.

Using the above notations the system of Eqs. (3.9)-(3.10) can be expressed into the vector form as

$$\partial_t \boldsymbol{\psi}_s + \partial_s \mathbf{f}_{si}(\boldsymbol{\psi}_s) - \partial_s \mathbf{f}_{sv}(\boldsymbol{\psi}_s, \partial_s \boldsymbol{\psi}_s) = \mathbf{q}_s(\boldsymbol{\psi}_s), \quad (3.17)$$

where  $\mathbf{f}_{si}$ ,  $\mathbf{f}_{sv}$  and  $\mathbf{q}_s$  are the inviscid and viscous flux functions and the source term, respectively. They are given by

$$\mathbf{f}_{si} = \left( v, \frac{v^2}{A} \right), \quad \mathbf{f}_{sv} = \left( 0, \frac{3}{\text{Re}} A \partial_s \left( \frac{v}{A} \right) \right) \quad \text{and} \quad \mathbf{q}_s = \left( 0, \frac{1}{\text{Fr}^2} A \right).$$

The boundary conditions at the nozzle are

$$\boldsymbol{\psi}_s(0, t) = (\boldsymbol{\psi}_s)_0 = (A_0, A_0 u_0) \quad (3.18)$$

and at the end of the fiber

$$\partial_s \left( \frac{v}{A} \right) (L(t), t) = 0 \quad (3.19)$$

$$\text{with } \frac{dL(t)}{dt} = \left( \frac{v}{A} \right) (L(t), t), \quad L(0) = 0. \quad (3.20)$$

There is a variety of discretization techniques available for developing discrete approximations to a set of governing partial differential equations (PDEs). The finite volume method ([25] and [34]) seems to be a logical choice in this case because it is inherently conservative. A conservative finite volume discretization will guarantee the conservation of mass. However, it will not conserve the momentum due to the presence of dissipative as well as the outer source term. Nevertheless, the given PDE (3.17) is discretized by the finite volume method. The fiber is divided into non-equidistant cells (see Fig. 3.2). The inviscid flux functions are approximated by the explicit upwind scheme. The viscous flux and the source term are approximated in an implicit way. To describe the scheme, we need to introduce the following additional notations.

Let the spatial grid points  $s_i$ ,  $i = 0, \dots, N$  with  $s_0 = 0$  and  $s_{i-1} < s_i$  be spaced non-equidistantly with cell width  $\Delta s_i = s_i - s_{i-1}$  at time level  $t^n$ ,  $n = 0, 1, \dots$ , with a time step  $\Delta t^{n+1} = t^{n+1} - t^n$ . The number of cells  $N$  grows in each time step by one, i.e.  $N(n) = n$ . To setup discrete equations we need an approximation of  $\boldsymbol{\psi}_s(s, t)$  over the cell  $[s_{i-1}, s_i]$ . Let  $(\boldsymbol{\psi}_s)_i^n$  be the cell average of  $\boldsymbol{\psi}_s(s, t)$  in the cell  $[s_{i-1}, s_i]$  at time  $t^n$ , i.e.

$$(\boldsymbol{\psi}_s)_i^n := \frac{1}{\Delta s_i} \int_{s_{i-1}}^{s_i} \boldsymbol{\psi}_s(s, t^n) ds.$$

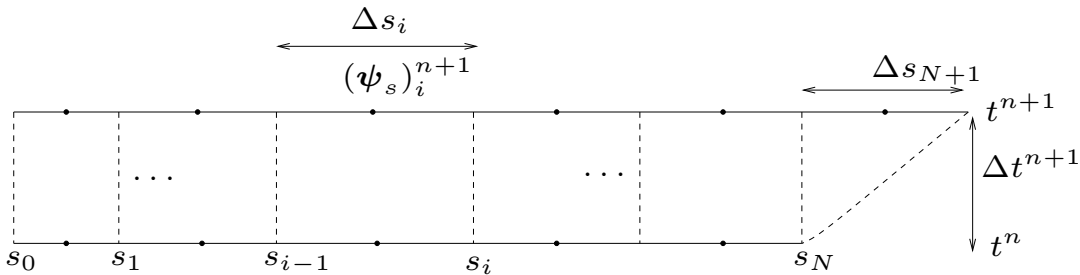


Figure 3.2: Grid type used for the straight fiber. Black dots and dashed vertical lines represent the nodal points and the cell faces.

For the given solutions  $(\boldsymbol{\psi}_s)_i^n$  at time level  $t^n$ , the solutions at the next time level  $t^{n+1}$  are obtained by integrating Eq. (3.17) over the space and time interval  $[s_{i-1}, s_i] \times$

$[t^n, t^{n+1}]$ . This yields the discrete equations. For the nodes,  $i = 1, \dots, N$ , we have

$$\begin{aligned} [(\boldsymbol{\psi}_s)_i^{n+1} - (\boldsymbol{\psi}_s)_i^n] \Delta s_i + [(\mathbf{f}_{si})_i^n - (\mathbf{f}_{si})_{i-1}^n] \Delta t^{n+1} - \\ [(\mathbf{f}_{sv})_i^{n+1} - (\mathbf{f}_{sv})_{i-1}^{n+1}] \Delta t^{n+1} = \Delta s_i \Delta t^{n+1} (\mathbf{q}_s)_i^{n+1}. \end{aligned} \quad (3.21)$$

The discrete flux functions and the source term appearing in Eq. (3.21) are given below.

An upwind approximation of inviscid flux  $\mathbf{f}_{si}$  gives

$$\begin{aligned} (\mathbf{f}_{si})_i^n &:= \frac{1}{\Delta t^{n+1}} \int_{t^n}^{t^{n+1}} \mathbf{f}_{si}(\boldsymbol{\psi}_s)(s_i, t) dt \\ &\simeq \mathbf{f}_{si}(\boldsymbol{\psi}_s)(s_{i-1/2}, t^n) = \left( v_i^n, \frac{(v_i^n)^2}{A_i^n} \right). \end{aligned} \quad (3.22)$$

The implicit approximation of viscous flux function  $\mathbf{f}_{sv}$  yields,

$$\begin{aligned} (\mathbf{f}_{sv})_i^{n+1} &:= \frac{1}{\Delta t^{n+1}} \int_{t^n}^{t^{n+1}} \mathbf{f}_{sv}(\boldsymbol{\psi}_s, \partial_s \boldsymbol{\psi}_s)(s_i, t) dt \\ &\simeq \mathbf{f}_{sv}(\boldsymbol{\psi}_s, \partial_s \boldsymbol{\psi}_s)(s_i, t^{n+1}) = \left( 0, \frac{3}{\text{Re}} A \partial_s \left( \frac{v}{A} \right) \right) (s_i, t^{n+1}) \end{aligned} \quad (3.23)$$

with

$$A(s_i, t^{n+1}) = \frac{1}{\Delta s_i + \Delta s_{i+1}} (\Delta s_{i+1} A_i^{n+1} + \Delta s_i A_{i+1}^{n+1}) \quad (3.24)$$

and

$$\partial_s \left( \frac{v}{A} \right) (s_i, t^{n+1}) = \frac{\left( \frac{v}{A} \right)_{i+1}^{n+1} - \left( \frac{v}{A} \right)_i^{n+1}}{\frac{\Delta s_{i+1}}{2} + \frac{\Delta s_i}{2}}.$$

Since the cell lengths are non-uniform, the values of  $A$  at the cell faces Eq. (3.24) are derived by weighted average of the two neighboring cell lengths. Furthermore, the first node  $i = 1$ , is a boundary node and therefore the approximation of viscous flux at  $s_0$  needs special attention. By using Eq. (3.18), the approximate value of  $\mathbf{f}_{sv}$  at  $s_0$  can be given by

$$(\mathbf{f}_{sv})_0^{n+1} = \mathbf{f}_{sv}(\boldsymbol{\psi}_s, \partial_s \boldsymbol{\psi}_s)(s_0, t^{n+1}) = \left( 0, \frac{3}{\text{Re}} A \partial_s \left( \frac{v}{A} \right) \right) (s_0, t^{n+1})$$

with

$$A(s_0, t^{n+1}) = A_0,$$

and

$$\partial_s \left( \frac{v}{A} \right) (s_0, t^{n+1}) = \frac{\left( \frac{v}{A} \right)_1^{n+1} - \left( \frac{v}{A} \right)_0^{n+1}}{\frac{\Delta s_1}{2}}.$$

The outer force term  $\mathbf{q}_s$  is approximated as follows:

$$\begin{aligned} (\mathbf{q}_s)_i^{n+1} &:= \frac{1}{\Delta s_i} \frac{1}{\Delta t^{n+1}} \int_{t^n}^{t^{n+1}} \int_{s_{i-1}}^{s_i} \mathbf{q}_s(s_i, t) ds dt \\ &\simeq \mathbf{q}_s(s_{i-1/2}, t^{n+1}) = \left( 0, \frac{1}{\text{Fr}^2} A_i^{n+1} \right). \end{aligned} \quad (3.25)$$

The resulting discretized Eq. (3.21) is given for the nodes  $i = 1, \dots, N$ . Since at time  $t^{n+1}$  the fiber changes its length by  $\Delta s_{N+1} = L(t^{n+1}) - s_N$ , Eq. (3.17) has to be approximated at the node  $N + 1$  in a special way.

The last node  $N + 1$  is a boundary node, therefore we use Eqs. (3.19)-(3.20) for the approximation of Eq. (3.17). Further, we note that there are no outgoing fluxes at the last node. Thus at the last node  $N + 1$ , we have

$$(\boldsymbol{\psi}_s)_{N+1}^{n+1} \Delta s_{N+1} - (\mathbf{f}_{si})_N^n \Delta t^{n+1} + (\mathbf{f}_{sv})_N^{n+1} \Delta t^{n+1} = \Delta s_{N+1} \Delta t^{n+1} (\mathbf{q}_s)_{N+1}^{n+1}, \quad (3.26)$$

where the approximation of the flux functions  $\mathbf{f}_{si}$ ,  $\mathbf{f}_{sv}$  and the outer force  $\mathbf{q}_s$  are already given in Eqs. (3.22), (3.23) and (3.25).

Looking at the grid of Fig. 3.2, the reader may ask why the outer force term  $\mathbf{q}_s$  in the last node for Eq. (3.26) has not been approximated by the correct cell area  $(1/2)\Delta s_{N+1}\Delta t^{n+1}$ . An attempt to answer this question is made later (see Remark 3.2).

Thus, the discretized Eqs. (3.21) and (3.26) are  $2N + 2$  equations for the  $2N + 3$  unknowns  $(\boldsymbol{\psi}_s)_1^{n+1}, \dots, (\boldsymbol{\psi}_s)_{N+1}^{n+1}$  and the length  $\Delta s_{N+1}$  of the new cell. In order to close the discrete system we need one more equation which we derive in the following.

Here, we use the discrete mass equation, in particular the first component of the vector Eq. (3.26)

$$A_{N+1}^{n+1} \Delta s_{N+1} - v_N^n \Delta t^{n+1} = 0 \quad (3.27)$$

for the approximation of the length  $\Delta s_{N+1}$ . Thus, we still need an additional equation for the cross-sectional area  $A_{N+1}^{n+1}$  at the last node  $N + 1$ . This can be done by linearly interpolating  $A_N^{n+1}$  and  $A_{end}$

$$(\Delta s_N + 2\Delta s_{N+1})A_{N+1}^{n+1} - (\Delta s_{N+1}A_N^{n+1} + (\Delta s_N + \Delta s_{N+1})A_{end}) = 0, \quad (3.28)$$

where  $A_{end} = 1$  is the cross-sectional area at the end of the fiber.

Now, the discretized algebraic Eqs. (3.21), (3.26) and (3.28) are closed with  $2N + 3$  equations for the  $2N + 3$  unknowns, i.e.  $(\boldsymbol{\psi}_s)_1^{n+1}, \dots, (\boldsymbol{\psi}_s)_{N+1}^{n+1}$  and the cell length  $\Delta s_{N+1}$ . The procedure to solve these equations is explained in Algorithm 3.1.

The motivation for this form of approximation of length  $\Delta s_{N+1}$  by Eq. (3.27) and the cross-sectional area at the last node  $A_{N+1}^{n+1}$  by Eq. (3.28) is explained in Remark 3.3.

**Remark 3.2** We answer here the question of why the outer force term  $\mathbf{q}_s$  in the last node Eq. (3.26) has not been approximated by the correct cell area, i.e.  $(1/2)\Delta s_{N+1}\Delta t^{n+1}$ . We take into account the discretized mass and momentum Eq. (3.26) in the inviscid limit with  $(1/2)\Delta s_{N+1}\Delta t^{n+1}$  as an approximation for the outer source term. After some simple algebraic transformations we have the following expression:

$$\frac{u_{N+1}^{n+1} - u_N^n}{\Delta t^{n+1}} = \frac{1}{2\text{Fr}^2}. \quad (3.29)$$

From Eq. (3.29), we see that the acceleration of the particle in the last node is  $(1/2\text{Fr}^2)$ . But, the particle in the last node should move with the uniform acceleration  $1/\text{Fr}^2$ . Therefore, we chose the cell area  $\Delta s_{N+1}\Delta t^{n+1}$ .

**Remark 3.3** Although Eq. (3.26) has been derived through simplification by using Eq. (3.20) the number of unknowns is not reduced. With ongoing time, the length of the fiber increases by one cell length. In every new time step, the length of this new cell is always one of the unknowns of the system. In the model, this information is described by Eq. (3.20). Therefore, it seems to be natural to construct a discretize equation for the length  $\Delta s_{N+1}$  from Eq. (3.20) by using Eq. (3.19).

This can be done either implicitly or explicitly. The implicit approximation yields

$$\Delta s_{N+1} = \Delta t^{n+1} \left( \frac{v}{A} \right)_{N+1}^{n+1}. \quad (3.30)$$

By plugging Eq. (3.30) into Eq. (3.26), one can see that in the inviscid limit ( $\text{Re} \rightarrow \infty$ ) leads after some algebraic manipulation to

$$(Au)_{N+1}^{n+1} = (Au)_N^n, \quad \text{and} \quad u_{N+1}^{n+1} = u_N^n + \frac{1}{\text{Fr}^2}\Delta t^{n+1}.$$

This means the mass flux between the cells  $N$  and  $N+1$  is constant, while the velocity is increasing. Thus  $A$  is decreasing between these cells. This is unreasonable, because the cross section has to grow up to  $A_{\text{end}} = 1$ . Therefore we do not follow this way.

By approximating Eq. (3.20) explicitly, we have

$$\Delta s_{N+1} = \Delta t^{n+1} \left( \frac{v}{A} \right)_N^n. \quad (3.31)$$

By plugging Eq. (3.31) into the first component of the vector Eq. (3.26), one can see that

$$A_{N+1}^{n+1} = A_N^n. \quad (3.32)$$

As a consequence of our initialization this leads to the mean value  $A_{N+1}^{n+1} = 1$  for the cross-sectional area in the last cell. This approximation is reasonable, but it slightly over-estimates the cross-sectional area in the last node, since we expect  $A_{N+1}^{n+1} < A_{\text{end}} = 1$ .

To overcome this problem we have computed the length of the new cell by the discretize mass equation (first component of Eq. (3.26)) and  $A_{N+1}^{n+1}$  by the linear interpolation formula Eq. (3.28), that is more precise than Eq. (3.32).

**Remark 3.4** The discrete method conserves mass.

The total mass of the fiber in the given length from 0 to  $L(t)$  at time  $t$  in the non-dimensional form is given by

$$M(t) = \int_0^{L(t)} A(s, t) ds.$$

The rate of change of mass in  $[0, L(t)]$  in time gives

$$\begin{aligned} \partial_t M(t) &= \frac{\partial}{\partial t} \int_0^{L(t)} A(s, t) ds & (3.33) \\ &= \int_0^{L(t)} (-\partial_s(Au)) ds + (Au)(L(t), t) \quad (\text{using Eqs. (3.9) and (3.13)}) \\ &= (Au)(0, t) \end{aligned}$$

In the following we will show that the discretized Eqs. (3.21) and (3.26) preserve the mass.

Let  $M^n = \sum_{i=1}^N A_i^n \Delta s_i$  and  $M^{n+1} = \sum_{i=1}^{N+1} A_i^{n+1} \Delta s_i$  be the total mass at time  $t^n$  and  $t^{n+1}$ , respectively. Then the rate of change of mass in time is,

$$\begin{aligned} \frac{M^{n+1} - M^n}{\Delta t} &= \frac{A_{N+1}^{n+1} \Delta s_{N+1}}{\Delta t^{n+1}} + \sum_{i=1}^N \frac{A_i^{n+1} - A_i^n}{\Delta t^{n+1}} \Delta s_i \\ &= v_N^n - \sum_{i=1}^N (v_i^n - v_{i-1}^n) \quad (\text{by the first component of Eqs. (3.21) and (3.26)}) \\ &= v_N^n - v_N^n + v_0^n = v_0^n = (Au)_0^{n+1} \end{aligned}$$

which is a discrete analogue of Eq. (3.33).

**Algorithm 3.1** The discretized algebraic Eqs. (3.21), (3.26) and (3.28) are closed with  $2N+3$  equations for the  $2N+3$  unknowns, i.e.  $(\psi_s)_1^{n+1}, \dots, (\psi_s)_{N+1}^{n+1}$  and the cell length  $\Delta s_{N+1}$ . The discretized mass equation, i.e. the first component of the vector Eq. (3.21) is an explicit one, but at the last two nodes, all equations are coupled implicitly with the cell length  $\Delta s_{N+1}$ . However, for the better performance of the solver, we treat Eq. (3.28) explicitly, and solve Eqs. (3.21) and (3.26) simultaneously. Thus, we first solve Eqs. (3.21) and (3.26) implicitly by using the MATLAB-6.5 *fsolve* routine. This routine uses a non-linear least-squares algorithm to solve a system of



non-linear equations. After obtaining solution from Eqs. (3.21) and (3.26), we solve Eq. (3.28) explicitly. Due to explicit discretization of the mass equation, a CFL (Courant-Friedrichs-Levy) condition (see e.g., [25]) is imposed on the size of the time step. Since the size of the cell lengths is not uniform we choose the time step  $\Delta t^{n+1}$  as the minimum of the ratios between grid length and velocity, i.e.

$$\Delta t^{n+1} = \min \left\{ \frac{\Delta s_i}{u_i^n} \right\} \quad \text{for } i = 1, \dots, N. \quad (3.34)$$

Thus the algorithm is the following:

**Initialize** time step

**Solve** Eqs. (3.26) and (3.28) to get the first cell length, and cross-sectional area and velocity at the first node.

**Update** time step by the CFL condition (3.34)

**repeat**

**Solve** Eqs. (3.21) (for the interior nodes) and (3.26) and (3.28) (for the boundary node and the new cell length)

**Update** time step

**until** the desired fiber length is reached

### 3.2.2 Simulation results and discussion

In this section some simulation results of the cross-sectional area, velocity and the tension on the fiber are presented at three different non-dimensional times  $t = 1.3, 2.6$  and  $3.9$ . In Figs. 3.3-3.5 the numerical results are given for the parameters  $\text{Re} = 2$  and  $\text{Fr} = 1$ . The growth of fiber length with time is also shown in Fig. 3.6. To run the simulation an initial non-dimensional time step  $\Delta t = 0.01$  is used.

- **Cross-sectional area:** In Fig. 3.3 the cross-sectional area is plotted against the arc-length at three different times. From this result we see that cross-sectional areas at the nozzle and at the end of the fiber are the same due to stress-free boundary condition (see Remark. 3.1). The cross-sectional area decreases slowly for the initial time periods, but the rate of the decrease becomes faster for ongoing time.
- **Velocity:** In Fig. 3.4 we plot velocity versus arc-length at three different times. This simulation result shows that the velocity increases both with time  $t$  and arc-length  $s$ . Near to the end of the fiber the velocity profile appears constant because the stress does not act at the end of the fiber.

- **Tension:** The tension, that is, in the integrated form  $(3/\text{Re})A\partial_s u$  is visualized against the arc-length  $s$  in Fig. 3.5. It shows that tension is approximately linear for small fiber lengths. When the fiber grows, the tension profile is not linear any more. However, in all cases the tension acting onto the fiber is strongest near the nozzle and decreases with growing distance from the nozzle.

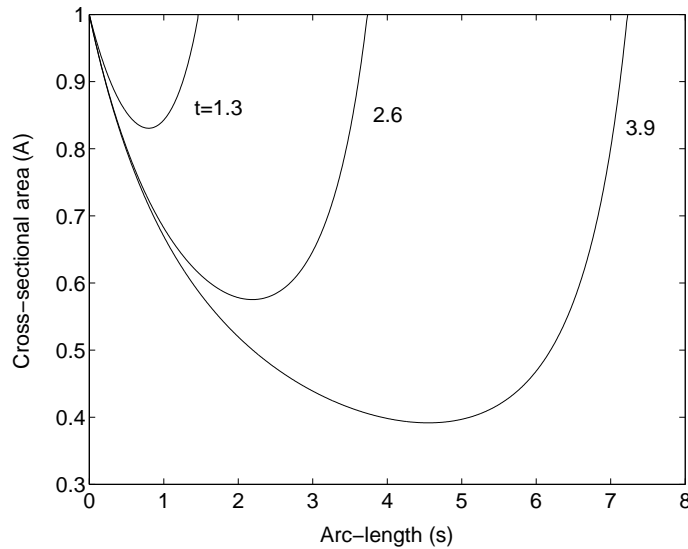


Figure 3.3: Cross-sectional area of a growing fiber at three different times.

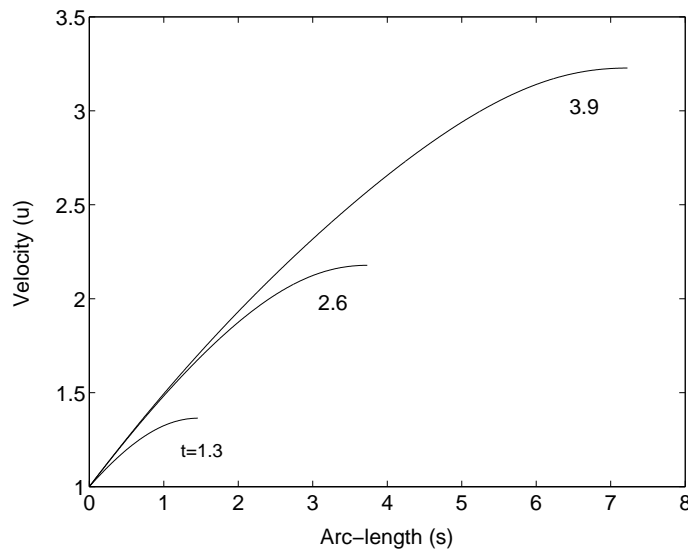


Figure 3.4: Velocity of a growing fiber at three different times.

- **Fiber length:** Fig. 3.6 depicts how the fiber length grows with respect to time. Initially, the fiber stretches slowly. It seems that viscous forces are dominant in the early stage of the fiber growth and do not allow the fiber to grow more rapidly. After this initial stage, the fiber length changes significantly.

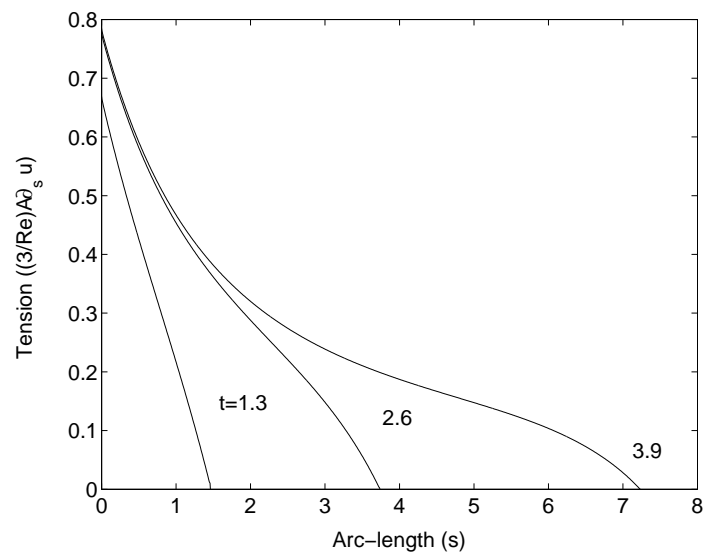


Figure 3.5: Tension on a growing fiber at three different times.

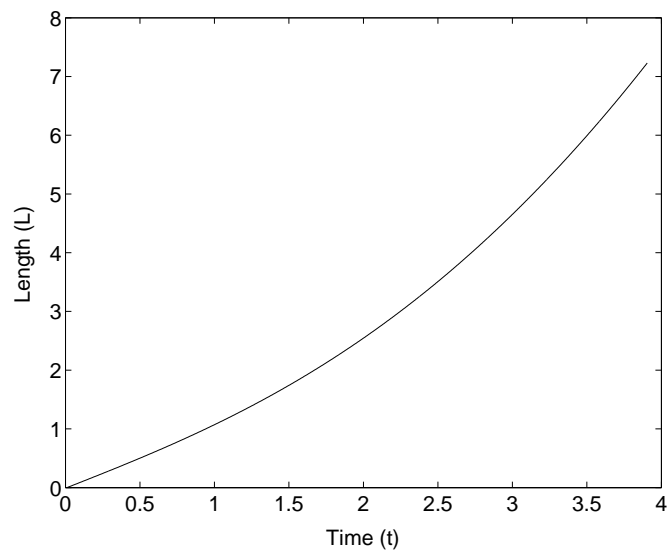


Figure 3.6: Fiber length versus time.

### 3.2.3 Industrial application of the straight fiber model

In industry, glass fibers are often produced by centrifugal forces. Here, the rotational speed of the rotating device is sufficiently high but the final fibers are very small in comparison to the radius of the rotating device. In this case the fiber seems to be nearly straight. This process is described in more detail with a realistic set of parameters in Chapter 5. However, at this stage it is sufficient to note that the gravitational and coriolis force have very little effect on the production of fibers. Hence, the fiber comes out due to the centrifugal force. Thus, instead of simulating the straight fiber model with a gravitational force, it would be of interest to simulate the model with a position dependent force, i.e. with a centrifugal force.

A position dependent force in dimensional form can be expressed as  $f_p^*(s^*) = \omega^2(L_0 + s^*)$ , where  $s^*$ ,  $L_0$  and  $\omega$  are the dimensional fiber arc-length, the radius and speed of the rotating device, respectively. By following the non-dimensional procedure as described in Section 2.3, the dimensional force  $f_p^*$  can be written as  $f_p(s) = (1/Rb^2)(1 + s)$ , where  $s$  is the dimensionless arc-length variable and  $Rb$  is the Rossby number. For the simulation we consider the discretized Eqs. (3.21), (3.26) and (3.28), but we replace the Froude number  $Fr$ , which is appearing in the body force term  $\mathbf{q}_s$  in Eqs. (3.21) and (3.26) by a position dependent force  $f_p$ .

In the previous section the results on cross-section, velocity, tension and length of the fiber for a different parameters are presented. In the following simulation results the parameters  $Re = 0.025$  and  $Rb = 0.001$  are taken from the industrial application data given in Chapter 5. Notice also that the parameters are very small and a minimum initial time step  $\Delta t = 0.0005$  is chosen for the simulation.

The simulation results of the cross-sectional area and length of the fiber are plotted in Figs. 3.7-3.8. One can see that the results are qualitatively identical to the results of the previous section, but some slight differences can be observed. For example, it can be noticed that the decrease rate of the cross-sectional area is very fast as we can see in Fig. 3.7. The cross-sectional area rapidly decreases at the nozzle and then stays almost constant. The numerical scheme has also the effect of reproducing boundary layer, which is evident in this figure. It can also be seen that the fiber now grows very fast due to the high centrifugal force into the problem.

In the present case the Reynolds number  $Re = 0.025$  is very small in comparison to the simulation parameter of the previous section. Smaller values mean that the viscous force is higher and opposes the fiber to fall quickly. Therefore, the initial growth of the fiber is very slow as it can be clearly seen in Fig. 3.8. But after this transient period the fiber accelerates rapidly.

The velocity profiles obtained from the simulation looks quite similar to Fig. 3.4. Therefore, simulation result for the velocity is not presented here again. In fact,

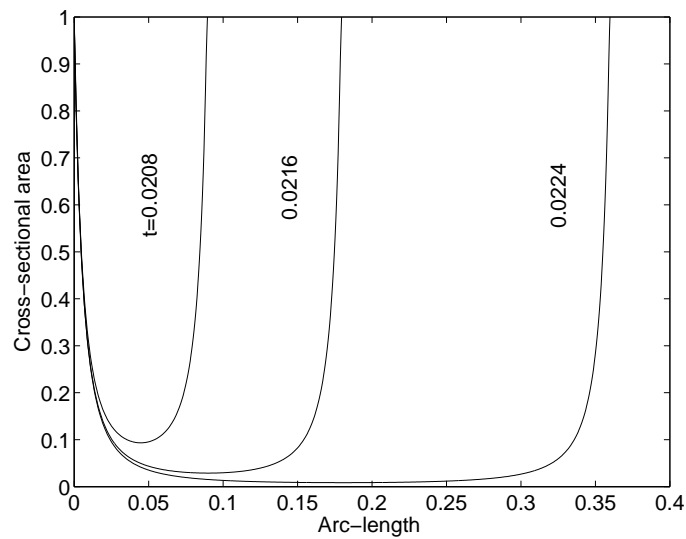


Figure 3.7: Cross-sectional area versus arc-length at three different times for the parameters  $Re = 0.025$  and  $Rb = 0.001$ .

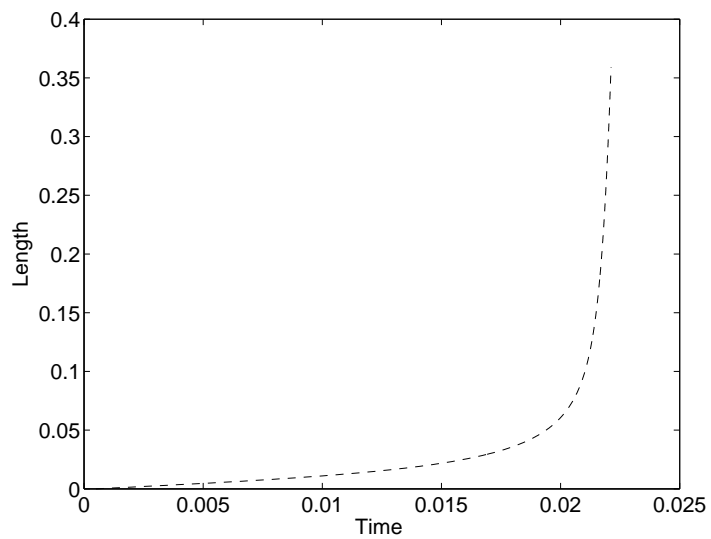


Figure 3.8: Fiber length versus time for the parameters  $Re = 0.025$  and  $Rb = 0.001$ .

velocity always increases with time. Moreover, it increases rapidly in this problem as the cross-sectional area shown in Fig. 3.7 decreases very fast. But on the other hand, the tension on the fiber is always higher at the nozzle and then decreases faster, and approaches to zero. As a consequence, when the tension goes near to zero the fiber simply fall with the outer force, and it can be visualized (Fig. 3.8).

The application of the straight fiber model to the production of glass fibers by a centrifugal spinning process is purely based on the fact that such fibers are nearly straight. The obtained results for the cross-sectional area and the length of the fiber are quite reasonable and provide some insight into the real problem, however the model cannot predict the whole fiber profile. Thus, Section 3.3 deals with curved fibers.

**Remark 3.5** The numerical results produced by the scheme are reasonable from a physical point of view. For example, the velocity increases and the cross-sectional area decreases with time. It is also important to see that the scheme has the effect of reproducing boundary layer at the end of the cross-sectional area of the fiber, which is consistent with the framework of the model. However, an important question always arises about the specification of the initial time step. Experience shows that this time step should be equal to the revolution period of the rotating device. This means that the starting time should be at least one or two orders less than the Rossby number. In particular, for gravity driven flow it should be at least one or two orders less than the Froude number.

### 3.2.4 Convergence tests

The problem as formulated in Section 3.2 is suitable for solution by using the proposed numerical scheme in Section 3.2.1. We have used this scheme to solve the equations of the straight fiber model. To demonstrate the convergence of our numerical scheme with respect to the decreasing initial time step, we consider the fiber length. An analysis of convergence with increasing cell number has been performed.

Table 3.1 gives some results for fiber length  $L_{\Delta t}$  at final time  $t = 1$  for different values of the initial time step  $\Delta t$ . The used parameters are  $\text{Re} = 1$  and  $\text{Fr} = 2$ . The corresponding values of  $L_{\Delta t}$  show convergence to first order, and this is quite reasonable as the proposed scheme is of first order. To calculate the relative error, i.e.  $\Delta L_{\Delta t} = (L_{\Delta t} - L_{\Delta t^*})/L_{\Delta t^*}$ , the reference solution  $L_{\Delta t^*} = 1.001563$  is taken for the smallest time step  $\Delta t^* = 0.0015625$ .

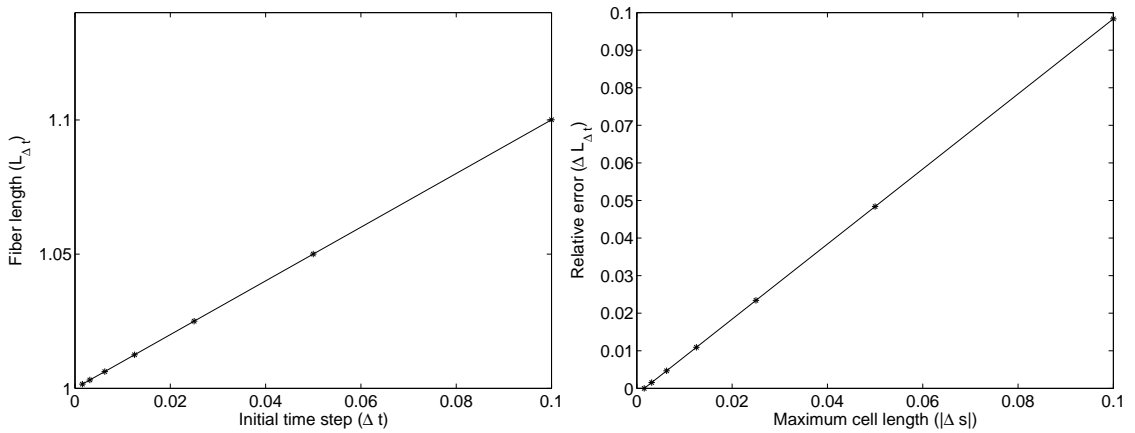
It is interesting to note that when we decrease the initial time step by half, the computational time approximately doubles as we can see in the first and third columns

Initial time step $\Delta t$	Max. cell length $ \Delta s $	No. of time steps	Fiber length $L_{\Delta t}$	Relative error $\Delta L_{\Delta t}$
0.1	0.100000	12	1.100049	0.047640
0.05	0.050000	22	1.050025	0.024402
0.025	0.025000	42	1.025012	0.012351
0.0125	0.012500	82	1.012506	0.006214
0.00625	0.006250	162	1.006253	0.003117
0.003125	0.003125	322	1.003126	0.001560
* 0.0015625	0.001562	642	* 1.001563	0

Table 3.1: Fiber length at  $t=1$ .

of the Table 3.1. Since fluid velocity is always maximum at the end of the fiber, the time step governed by the CFL condition (3.34) always depends on the last cell. This makes the cells are almost equal in length.

To show this more clearly, the data given in Table 3.1 is plotted in Fig. 3.9. In the left panel of Fig. 3.9 fiber length versus initial time step is given. This shows that the fiber length is linearly increasing with the increase of initial time step. In the right panel of the Fig. 3.9 the error is plotted versus maximum cell length. Since the numerical scheme is linear, the relative error also increases linearly with the increase of maximum cell length.

Figure 3.9: Error plot, Left: Fiber length at time  $t = 1$  versus initial time step. Right: Relative error versus maximum cell length.

### 3.3 Curved fiber (2D center-line)

In this section we will analyze the model Eqs. (3.1)-(3.8) numerically for a non-stationary viscous fiber emerging from a rotating device. In this situation the center-line of the fiber is curved due to rotational and gravitational forces. The fiber formation is of course supported by the aerodynamic forces which can also curve the fiber path. However, the present discussion is restricted to rotational and gravitational forces.

In the real problem concerning the manufacture of glass fibers, rotational forces are much stronger than gravitational ones. Thus, it is appropriate to neglect the gravity force, and as a consequence we can drop the fiber coordinate in the direction of gravity. As a result the three-dimensional fiber problem with respect to the fiber center-line is reduced to a two-dimensional problem. With respect to the coordinate configuration (see Fig. 3.1), we drop the coordinate  $\gamma_2$  and thus  $\boldsymbol{\gamma}$  and  $\tilde{\mathbf{v}}$  are two-dimensional vectors given by

$$\boldsymbol{\gamma} = (\gamma_1, \gamma_3) \quad \text{and} \quad \tilde{\mathbf{v}} = (\tilde{v}_1, \tilde{v}_3).$$

Hence, the outer force term Eq. (3.8) reads

$$\tilde{\mathbf{f}} = \frac{2}{\text{Rb}} (-\tilde{v}_3, \tilde{v}_1) + \frac{1}{\text{Rb}^2} (\gamma_1, \gamma_3). \quad (3.35)$$

Moreover, the initial position and direction of the center-line  $\boldsymbol{\gamma}$  are  $\boldsymbol{\gamma}_0 = (1, 0)$  and  $\boldsymbol{\tau}_0 = (1, 0)$ .

To solve this problem, described by Eqs. (3.1)-(3.8), a numerical scheme similar to that of the straight fiber model is proposed in the following section.

#### 3.3.1 Numerical scheme for the curved fiber

The finite volume scheme developed for the particular problem of a straight fiber has been successfully implemented in the previous section. We will now extend this approach for the numerical solution of the derived asymptotic model with rotational forces. Matters are however not completely straightforward, since the center-line is one of the additional unknowns of the problem, and for this reason the coupling and constraint equations (see Eqs. (3.3)-(3.4)) need special treatment in the discretization. This is described in more detail as follows:

For the numerical implementation of the model we first simplify the equations by introducing an angle function  $\theta$ , which is a function of  $s$  and  $t$ . We set

$$\partial_s \boldsymbol{\gamma} = (\partial_s \gamma_1, \partial_s \gamma_3) = (\cos(\theta), \sin(\theta)) = \mathbf{e}_\theta. \quad (3.36)$$



Additionally, the function  $\theta$  meets the following condition at the nozzle

$$\theta(0, t) = 0.$$

It may be noted here that with the introduction of the angle function  $\theta$ , the second-order derivative (with respect to arc-length) term for  $\gamma$ , appearing in the viscous term of the momentum Eq. (3.2) is reduced to a first-order term in  $\theta$ . Furthermore, Eq. (3.36) automatically satisfies the constraint condition (3.4).

Now, by introducing auxiliary variables

$$\mathbf{w} = (w_1, w_3) = (A\tilde{v}_1, A\tilde{v}_3) \quad \text{and} \quad \mathbf{w}^\perp = (-w_3, w_1),$$

the model Eqs. (3.1)-(3.4) for  $s \in [0, L(t))$  can be rewritten as

$$\partial_t \boldsymbol{\psi}_c + \partial_s \mathbf{f}_{ci}(u\boldsymbol{\psi}_c) - \partial_s \mathbf{f}_{cv}(\boldsymbol{\psi}_c, \mathbf{e}_\theta, \partial_s u) = \mathbf{q}_c(\boldsymbol{\psi}_c, \gamma) \quad (3.37)$$

$$\partial_t \gamma + u \mathbf{e}_\theta = \frac{\mathbf{w}}{A} \quad (3.38)$$

$$\partial_s \gamma = \mathbf{e}_\theta, \quad (3.39)$$

where  $\boldsymbol{\psi}_c$ ,  $\mathbf{f}_{ci}$ ,  $\mathbf{f}_{cv}$  and  $\mathbf{q}_c$  are the vector of primitive variables, the inviscid and viscous flux functions, and the source term, respectively. They are given by

$$\begin{aligned} \boldsymbol{\psi}_c &= (A, \mathbf{w}), \quad \mathbf{f}_{ci} = u\boldsymbol{\psi}_c, \\ \mathbf{f}_{cv} &= \left(0, \frac{3}{\text{Re}} A \mathbf{e}_\theta \partial_s u\right) \quad \text{and} \quad \mathbf{q}_c = \left(0, \frac{2}{\text{Rb}} \mathbf{w}^\perp + \frac{1}{\text{Rb}^2} A \gamma\right). \end{aligned}$$

Thus, by adding a new variable  $\theta$  to the system, the number of equations is increased by one. Thus, Eqs. (3.37)-(3.39) form a closed model for the seven unknowns  $\boldsymbol{\psi}_c$ ,  $u$ ,  $\gamma$  and  $\theta$ .

The boundary conditions at the nozzle are

$$\begin{aligned} \boldsymbol{\psi}_c(0, t) &= (\boldsymbol{\psi}_c)_0, \quad u(0, t) = u_0 \\ \gamma(0, t) &= \gamma_0, \quad \partial_s \gamma(0, t) = (1, 0) \\ \theta(0, t) &= 0. \end{aligned} \quad (3.40)$$

The symbol  $(\boldsymbol{\psi}_c)_0$  appearing in Eq. (3.40) is equal to  $(A_0, \mathbf{w}_0)$  with  $\mathbf{w}_0 = A_0 u_0 \boldsymbol{\tau}_0$ . This relation can be seen from Eq. (3.38).

The boundary condition at the end of the fiber are

$$\partial_s u(L(t), t) = 0, \quad (3.41)$$

$$\text{with} \quad \frac{dL(t)}{dt} = u(L(t), t), \quad L(0) = 0. \quad (3.42)$$

To solve the equations of the straight fiber model, the finite volume method is employed on a non-uniform grid. In the present problem the model equations are a set of PDEs with differential constraint. Thus, our main interest in the discretization lies in mass as well as constraint preserving. This can be achieved by a staggered grid method (see e.g., [17, 34]).

Let us discretize the fiber length using a staggered non-uniform grid as shown in Fig. 3.10. In the grid, the variables  $\psi_c$ ,  $u$  and  $\theta$  are located in the cell centers and the fiber center-line  $\gamma$  in the cell faces. Following the notations of Section 3.2.1, we take the set of non-equidistant grid points  $s_i$ ,  $i = 0, 1, \dots, N$  with  $0 = s_0$  and  $s_i < s_{i+1}$  at time level  $t^n$ ,  $n = 0, 1, \dots$ . The length of the  $i$ th cell is denoted by  $\Delta s_i = s_i - s_{i-1}$ . The symbol  $\Delta t^{n+1} = t^{n+1} - t^n$  stands for the time step. Again, the number of cells  $N$  grows with the time step, i.e.  $N(n) = n$ . As usual, we denote the cell average of  $\psi_c(s, t)$ ,  $u(s, t)$  and  $\theta(s, t)$  in the cell  $[s_{i-1}, s_i]$  at time  $t^n$  by  $(\psi_c)_i^n$ ,  $u_i^n$  and  $\theta_i^n$ . The approximated value of  $\gamma(s, t)$  at the cell faces  $s_i$  at time  $t^n$  is denoted by  $\gamma_i^n$ .

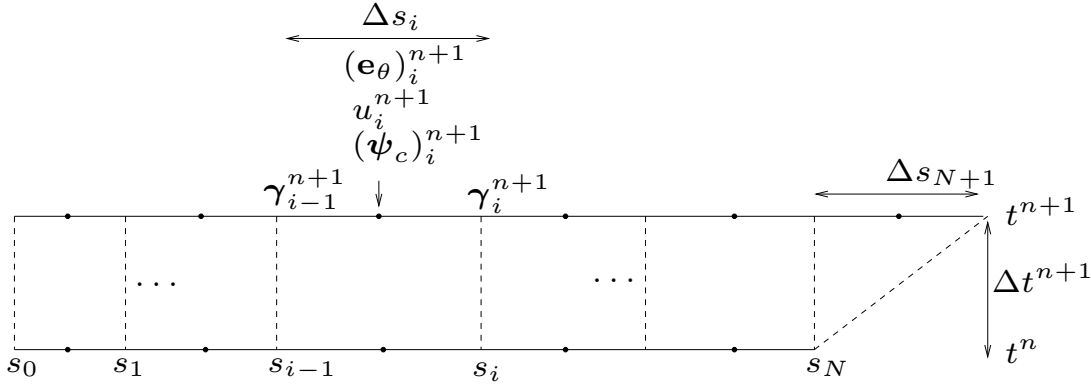


Figure 3.10: Staggered grid used for the curved fiber. Black dots and dashed vertical lines are marked for the nodal points and the cell faces.

Following the approximation procedure of Section 3.2.1, the inviscid flux is derived in an upwind sense, while the viscous flux and source terms are approximated implicit way.

Thus, the scheme as follows: From the known solutions  $(\psi_c)_i^n$ ,  $u_i^n$ ,  $\theta_i^n$  and  $(\gamma)_i^n$  at time level  $t^n$ , the solutions at next time level  $t^{n+1}$  can be derived after formal integration of Eqs. (3.37)-(3.39) over the interval  $[s_{i-1}, s_i] \times [t^n, t^{n+1}]$ . Thus, for nodes  $i = 1, \dots, N$  we obtain,

$$\begin{aligned}
 & [(\psi_c)_i^{n+1} - (\psi_c)_i^n] \Delta s_i + [(\mathbf{f}_{ci})_i^n - (\mathbf{f}_{ci})_{i-1}^n] \Delta t^{n+1} - \\
 & [(\mathbf{f}_{cv})_i^{n+1} - (\mathbf{f}_{cv})_{i-1}^{n+1}] \Delta t^{n+1} = \Delta s_i \Delta t^{n+1} (\mathbf{q}_c)_i^{n+1}
 \end{aligned} \tag{3.43}$$

$$\frac{1}{2} [(\gamma_{i-1}^{n+1} - \gamma_{i-1}^n) + (\gamma_i^{n+1} - \gamma_i^n)] + u_i^{n+1} (\mathbf{e}_\theta)_i^{n+1} \Delta t^{n+1} = \left(\frac{\mathbf{w}}{A}\right)_i^{n+1} \Delta t^{n+1}, \quad (3.44)$$

$$(\gamma_i^{n+1} - \gamma_{i-1}^{n+1}) = \Delta s_i (\mathbf{e}_\theta)_i^{n+1}, \quad (3.45)$$

where the discrete flux functions  $(\mathbf{f}_{ci})_i^n$ ,  $(\mathbf{f}_{cv})_i^{n+1}$  and the source term  $(\mathbf{q}_c)_i^{n+1}$  are given by

$$(\mathbf{f}_{ci})_i^n = (u \boldsymbol{\psi}_c)_i^n, \quad (3.46)$$

$$(\mathbf{f}_{cv})_i^{n+1} = \left(0, \frac{3}{\text{Re}} A \mathbf{e}_\theta \partial_s u\right) (s_i, t^{n+1}), \quad (3.47)$$

and

$$(\mathbf{q}_c)_i^{n+1} = \left(0, \frac{2}{\text{Rb}} (\mathbf{w}^\perp)_i^{n+1} + \frac{1}{2\text{Rb}^2} A_i^{n+1} (\gamma_{i-1}^{n+1} + \gamma_i^{n+1})\right). \quad (3.48)$$

As it has been stated before (see Eq. 3.24), the values of  $A$  and  $\mathbf{e}_\theta$  at the cell faces have to be derived by a weighted average

$$A(s_i, t^{n+1}) \simeq \frac{1}{\Delta s_i + \Delta s_{i+1}} (\Delta s_{i+1} A_i^{n+1} + \Delta s_i A_{i+1}^{n+1})$$

$$\mathbf{e}_\theta(s_i, t^{n+1}) \simeq \frac{1}{\Delta s_i + \Delta s_{i+1}} (\Delta s_{i+1} (\mathbf{e}_\theta)_i^{n+1} + \Delta s_i (\mathbf{e}_\theta)_{i+1}^{n+1})$$

since the length of the cells is non-uniform. The velocity gradient at the cell faces is approximated by

$$\partial_s u(s_i, t^{n+1}) \simeq \frac{u_{i+1}^{n+1} - u_i^{n+1}}{\frac{\Delta s_{i+1}}{2} + \frac{\Delta s_i}{2}},$$

and at the point  $s_0$ , we have

$$\partial_s u(s_0, t^{n+1}) \simeq \frac{u_1^{n+1} - u_0^{n+1}}{\frac{\Delta s_1}{2}}.$$

The model Eqs. (3.37)-(3.39) are so far discretized for the nodes  $i = 1, \dots, N$ . For the change of fiber length  $\Delta s_{N+1} = L(t^{n+1}) - s_N$  at time  $t^{n+1}$ , a new node  $N + 1$  is created. We discretize Eqs. (3.37)-(3.39) at this new node according to the following considerations.

The new node  $N + 1$  is also the last node, so the approximation of Eq. (3.37) is done in a way similar to Eq. (3.26). For the approximation of the coupling condition Eq. (3.38), the time derivative term  $(\partial_t \boldsymbol{\gamma})$  is approximated by the linear interpolation between  $\partial_t \boldsymbol{\gamma}(s_{N-1}, t^{n+1})$  and  $\partial_t \boldsymbol{\gamma}(s_N, t^{n+1})$ . The motivation behind this approximation is that the discrete curved fiber model may lead to the straight fiber model under the assumptions that the flow of the material is driven by gravity alone.

Finally at node  $N + 1$ , we have

$$\begin{aligned} (\boldsymbol{\psi}_c)_{N+1}^{n+1} \Delta s_{N+1} - (\mathbf{f}_{ci})_N^n \Delta t^{n+1} + \\ (\mathbf{f}_{cv})_N^{n+1} \Delta t^{n+1} = \Delta s_{N+1} \Delta t^{n+1} (\mathbf{q}_c)_{N+1}^{n+1} \end{aligned} \quad (3.49)$$

$$a_1 (\gamma_{N-1}^{n+1} - \gamma_{N-1}^n) + a_2 (\gamma_N^{n+1} - \gamma_N^n) + u_{N+1}^{n+1} (\mathbf{e}_\theta)_{N+1}^{n+1} \Delta t^{n+1} = \left(\frac{\mathbf{w}}{A}\right)_{N+1}^{n+1} \Delta t^{n+1} \quad (3.50)$$

$$(\gamma_{N+1}^{n+1} - \gamma_N^{n+1}) = \Delta s_{N+1} (\mathbf{e}_\theta)_{N+1}^{n+1}, \quad (3.51)$$

where

$$a_1 = -\frac{\Delta s_{N+1}}{2\Delta s_N} \quad \text{and} \quad a_2 = \left(1 + \frac{\Delta s_{N+1}}{2\Delta s_N}\right).$$

As it can be seen from the previous considerations, the number of equations in (3.43)-(3.45), (3.49)-(3.51) is  $7N + 7$ , whereas the number of unknowns is  $7N + 8$ . The unknowns are  $(\boldsymbol{\psi}_c)_1^{n+1}, \dots, (\boldsymbol{\psi}_c)_{N+1}^{n+1}, u_1^{n+1}, \dots, u_{N+1}^{n+1}, \gamma_1^{n+1}, \dots, \gamma_{N+1}^{n+1}, \theta_1^{n+1}, \dots, \theta_{N+1}^{n+1}$  and the length  $\Delta s_{N+1}$  of the new cell.

Now, to close this system we need an additional equation for  $\Delta s_{N+1}$ . This discretized equation can be deduced from Eq. (3.42). The possible approximation of Eq. (3.42) and its behavior with respect to the system have already been discussed in Section 3.2.1. Thus, we do not repeat any detail here. Again, we approximate  $\Delta s_{N+1}$  from the first component of the vector Eq. (3.49) and close the discretized equations by

$$(\Delta s_N + 2\Delta s_{N+1})A_{N+1}^{n+1} - (\Delta s_{N+1}A_N^{n+1} + (\Delta s_N + \Delta s_{N+1})A_{end}) = 0, \quad (3.52)$$

where  $A_{end}$  is the cross-sectional area at the end of the fiber.

The discretized algebraic Eqs. (3.43)-(3.45), (3.49)-(3.51) and (3.52) are now a closed set of  $7N + 8$  equations for the  $7N + 8$  unknowns. The implementation procedure for this scheme is similar to Algorithm 3.1 (Section 3.2.1).

In the following section we first validate the results obtained from the simulation by comparing them with the analytical solution of the inviscid problem. Then, numerical results for a wide range of Reynolds and Rossby numbers are discussed in Section 3.3.3.

**Remark 3.6** The reader may raise here the same question about the weight of the last cell as pointed out in Remark 3.2. This question may also be answered in a similar way as discussed there. To see it more clearly, a simulation result of the fiber trajectory for two different situations, i.e. with  $(1/2)\Delta s_{N+1}\Delta t^{n+1}$  and  $\Delta s_{N+1}\Delta t^{n+1}$  is plotted in Fig. 3.11.

This figure shows that the approximation of the source term with factor  $1/2$  for the cell area of the last cell leads to a total wrong direction of the fiber trajectory (left panel of Fig. 3.11).

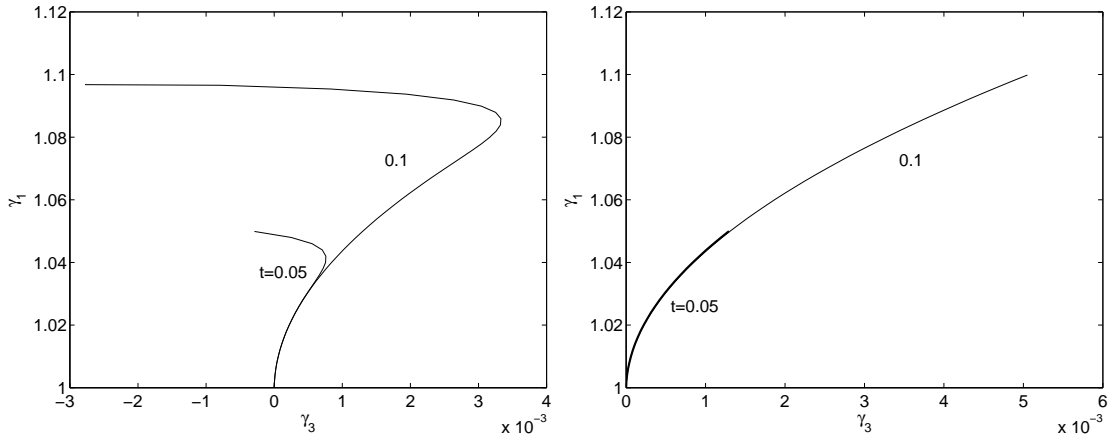


Figure 3.11: The fiber trajectory in the  $(\gamma_3, \gamma_1)$ - plane at two different times for  $\text{Re} = 6$  and  $\text{Rb} = 2$ , Left: With the  $(1/2)\Delta s_{N+1}\Delta t^{n+1}$  approximation of the outer source term , Right: With the  $\Delta s_{N+1}\Delta t^{n+1}$  approximation of the outer source term.

### 3.3.2 Validation of the numerical scheme

As a first validation of the numerical scheme proposed in Section 3.3.1 we compare the numerical results for a high Reynolds number with the analytical solutions of the inviscid problem. In the inviscid limit,  $\text{Re} \rightarrow \infty$ , the viscous term approaches zero. Thus, it is possible to drop the viscous term from the momentum equation. It should also be noted that the stress-free boundary condition (3.6) is not required any more to close the model equations, since the second order derivative term with respect to the arc-length variable  $s$  for the fluid velocity  $u$  disappears.

Consequently, to set up the equations of the inviscid fiber model, we consider the model Eqs. (3.1)-(3.5) and (3.7)-(3.8) but neglect the viscous term of the momentum Eq. (3.2), yielding

$$\partial_t A + \partial_s(Au) = 0 \quad (3.53)$$

$$\partial_t(A\tilde{\mathbf{v}}) + \partial_s(uA\tilde{\mathbf{v}}) = \tilde{\mathbf{f}}A \quad (3.54)$$

$$\tilde{\mathbf{v}} = \partial_t \boldsymbol{\gamma} + u \partial_s \boldsymbol{\gamma} \quad (3.55)$$

$$\| \partial_s \boldsymbol{\gamma} \| = 1 \quad (3.56)$$

with the boundary conditions at the nozzle,

$$A(0, t) = 1, \quad u(0, t) = 1 \quad (3.57)$$

$$\boldsymbol{\gamma}(0, t) = \boldsymbol{\gamma}_0, \quad \partial_s \boldsymbol{\gamma}(0, t) = \boldsymbol{\tau}_0$$

$$\tilde{\mathbf{v}}(0, t) = u_0 \boldsymbol{\tau}_0.$$

Additionally, the evolution of fiber length is given by

$$\frac{dL(t)}{dt} = u(L(t), t), \quad L(0) = 0. \quad (3.58)$$

The extra boundary condition given in Eq. (3.57) for the velocity  $\tilde{\mathbf{v}}$  at the nozzle  $s = 0$  is simply deduced from Eq. (3.55).

Since the developed numerical scheme is for the two-dimensional problem, the fiber center-line  $\gamma$  for the inviscid problem is also two-dimensional, and hence,  $\tilde{\mathbf{v}}$  is a two-dimensional vector. Moreover, the outer force  $\tilde{\mathbf{f}}$  appearing in Eq. (3.54) is the same as in Eq. (3.35).

To solve Eqs. (3.53)-(3.58) analytically, we formulate first the same problem in Lagrange coordinates. Then the solution obtained in Lagrange coordinates will be transformed back into the Eulerian system. Thus, for fixed time  $t$  and  $\tau \in [0, t]$ , the inviscid fiber problem in the Lagrange coordinates reads

$$\ddot{\boldsymbol{\chi}} = \tilde{\mathbf{g}}(\boldsymbol{\chi}, \dot{\boldsymbol{\chi}}) \quad (3.59)$$

with boundary conditions

$$\boldsymbol{\chi}(0) = \boldsymbol{\gamma}_0 \quad \text{and} \quad \dot{\boldsymbol{\chi}}(0) = \tilde{\mathbf{v}}_0, \quad (3.60)$$

where  $\boldsymbol{\chi}(\tau) = (\chi_1, \chi_3)(\tau)$  is the position of a material particle at time  $\tau$  and  $\tilde{\mathbf{g}}$  is the outer force, i.e.  $\tilde{\mathbf{g}} = (2/\text{Rb})(-\dot{\chi}_3, \dot{\chi}_1) + (1/\text{Rb}^2)(\chi_1, \chi_3)$ . The symbols  $\boldsymbol{\gamma}_0$  and  $\tilde{\mathbf{v}}_0$  are the initial position and velocity of the particle at the nozzle given in Eq. (3.57). The symbol  $(\cdot)$  refers to derivative with respect to the time variable  $\tau$ .

Equations (3.59)-(3.60) state a general initial value ODE problem. The analytical solution can be easily obtained by using any standard method. The solution of this ODE is given by

$$\boldsymbol{\chi}(\tau) = (1 + \tau)(\cos(c\tau), \sin(c\tau)) + c\tau(\sin(c\tau), -\cos(c\tau)),$$

where  $c = 1/\text{Rb}$ .

To describe the solutions of Eqs. (3.53)-(3.58) through  $\boldsymbol{\chi}$  in a parameterized way, we first introduce the following transformation.

For  $t > 0$  and  $\tau \in [0, t]$ , we define

$$S(\tau) = \int_0^\tau \|\dot{\boldsymbol{\chi}}\| d\tau'.$$

Assuming  $T$  to be the inverse function of  $S$ , the analytic solution of Eqs. (3.53)-(3.58) is given for  $s \in [0, S(t)]$  by

$$\begin{aligned} A(s, t) &= A_0 u_0 \partial_s T(s), & u(s, t) &= \frac{1}{\partial_s T(s)} \\ \boldsymbol{\gamma}(s, t) &= \boldsymbol{\chi}(T(s)), & \tilde{\mathbf{v}}(s, t) &= \dot{\boldsymbol{\chi}}(T(s)). \end{aligned} \quad (3.61)$$

Consequently, without calculating the inverse function  $T$  we are able to formulate a parametric solution. For  $\tau \leq t$ , it reads

$$\begin{aligned} A(S(\tau), t) &= \frac{A_0 u_0}{\|\dot{\boldsymbol{\chi}}(\tau)\|}, & u(S(\tau), t) &= \|\dot{\boldsymbol{\chi}}(\tau)\| \\ \boldsymbol{\gamma}(S(\tau), t) &= \boldsymbol{\chi}(\tau), & \tilde{\mathbf{v}}(S(\tau), t) &= \dot{\boldsymbol{\chi}}(\tau). \end{aligned} \quad (3.62)$$

One can easily check, that Eq. (3.61) satisfies the Eqs. (3.53)-(3.58) of the inviscid problem.

To compare the simulation result of the numerical scheme (Eqs. (3.43)-(3.45), (3.49)-(3.51) and (3.52)) with the analytical solution (Eq. (3.62)) of the inviscid model, we assume a sufficiently high Reynolds number, here  $\text{Re} = 3000$  in the viscous model. The comparison of the results for the fiber center-line, cross-sectional area and velocity is demonstrated in Figs. 3.12-3.14.

The results are shown at a certain fixed time  $t = 1.6102$ . A fixed Rossby number  $\text{Rb} = 2$  is considered for both the cases.

The comparison of the numerical results for the fiber center-line with the analytical solution is shown in Fig. 3.12. This figure shows that the solution of the numerical scheme agrees quite well with the analytical solution.

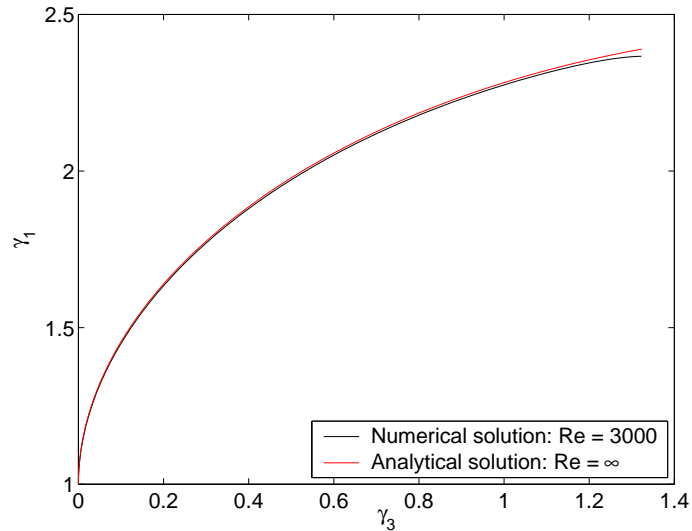


Figure 3.12: Comparison of the numerical results for the center-line (black curve) with the analytical solution (red curve).

A comparison between the numerical and analytical results for the cross-sectional area is given in Fig. 3.13. From this figure, we see that the numerical results match the analytical ones quite well, but they differ at the end. The developed numerical scheme is defined for the viscous model. The simulation results for high Reynolds

number approach to the inviscid one. However, there still remains a small viscosity in the fluid. As a result, a boundary layer at the end of the cross-sectional area develops in the case of viscous fluid.

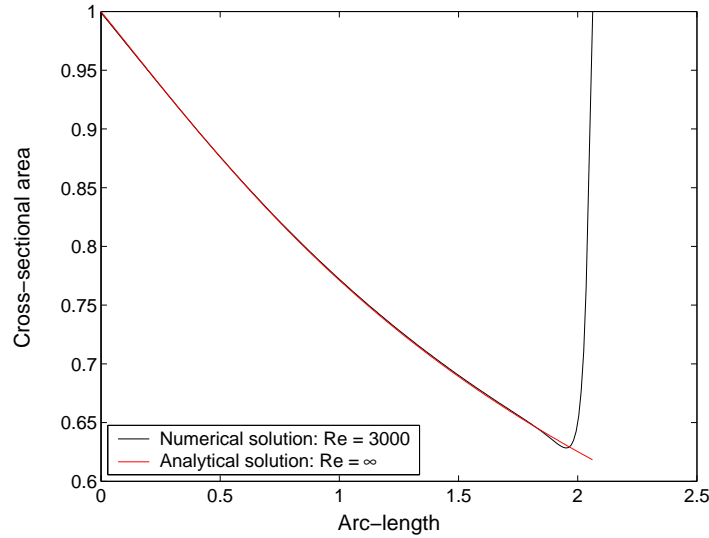


Figure 3.13: Comparison of the numerical results for the cross-sectional area (black curve) with the analytical solution (red curve).

The numerical results for the velocity and the analytical ones are compared in Fig. 3.14. They are nearly the same. The small difference at the end of the velocity profile is due to the prescribed stress-free boundary condition of the scheme.

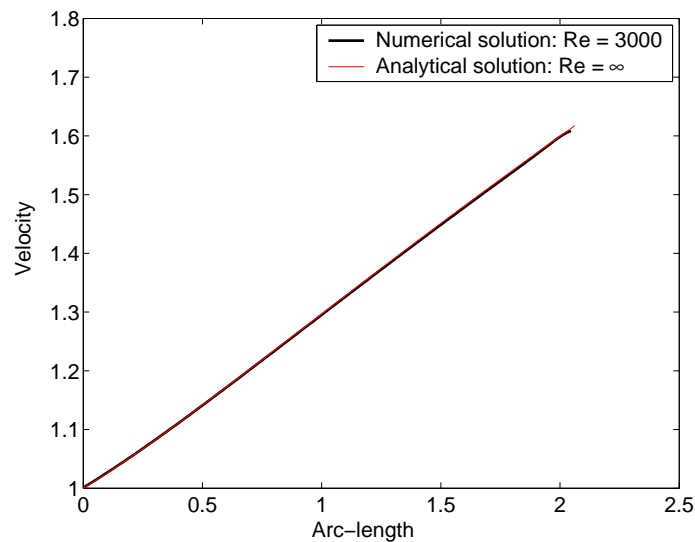


Figure 3.14: Comparison of the numerical results for the velocity (black line) with the analytical solution (red line).



### 3.3.3 Simulation results and discussion

In the previous section we validated the results of the numerical scheme with the analytical solution in the inviscid limit. In this section, to see the effects of viscosity and rotation on the center-line of the fiber and on the cross-sectional area, a number of simulations are performed for a wide range of Reynolds ( $Re$ ) and Rossby ( $Rb$ ) numbers. In particular, the simulation results are compared for the different parameters. For this purpose, numerical results for a fixed number of computational cells are used. Therefore, the results can be compared at different times.

In Fig. 3.15 we analyze the effects of viscosity on the evolution of the fiber by varying the Reynolds number, i.e. by changing the viscosity of the fiber and keeping the Rossby number constant. The simulation results for two sets of parameters,  $Rb = 4$ ,  $Re = 1$  and  $Rb = 4$ ,  $Re = 10$ , are given in Fig. 3.15.

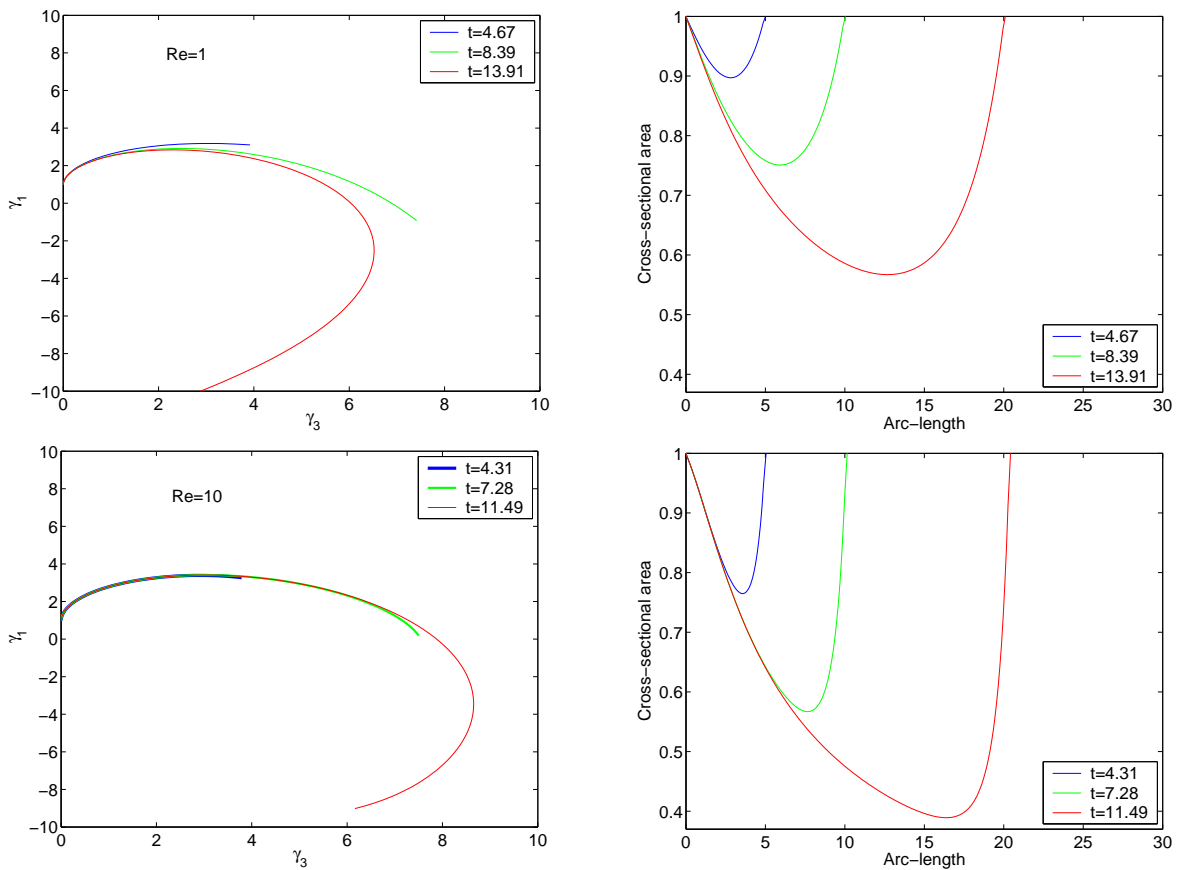


Figure 3.15: Evolution of the fiber center-line and cross-sectional area. Top and bottom left panels: The center-line in the  $(\gamma_3, \gamma_1)$ -plane, Top and bottom right panels: Cross-sectional areas versus fiber arc-length, Top panel:  $Rb = 4$  and  $Re = 1$ , Bottom panel:  $Rb = 4$  and  $Re = 10$ .

By comparing the top and bottom left panels of Fig. 3.15 we can see that with increasing Reynolds number the fiber center-line becomes less coiled. As it can also be seen from the left panels of this figure, the center-line with high viscosity has a larger curvature and takes a longer processing time to evolve. We further notice that with increasing Reynolds number the change of the center-line dynamics becomes smaller. Similarly, the comparison of the results displayed in the top and bottom right panels of Fig. 3.15 shows that with increasing Reynolds number the cross-sectional area decreases faster with respect to the fiber arc-length.

In Fig. 3.16 we show a similar comparison but we now keep the Reynolds number constant while varying the Rossby number, i.e. we perform simulations for different rotational forces. Again, two sets of data are considered,  $Re = 4$ ,  $Rb = 10$  and  $Re = 4$ ,  $Rb = 1$ .

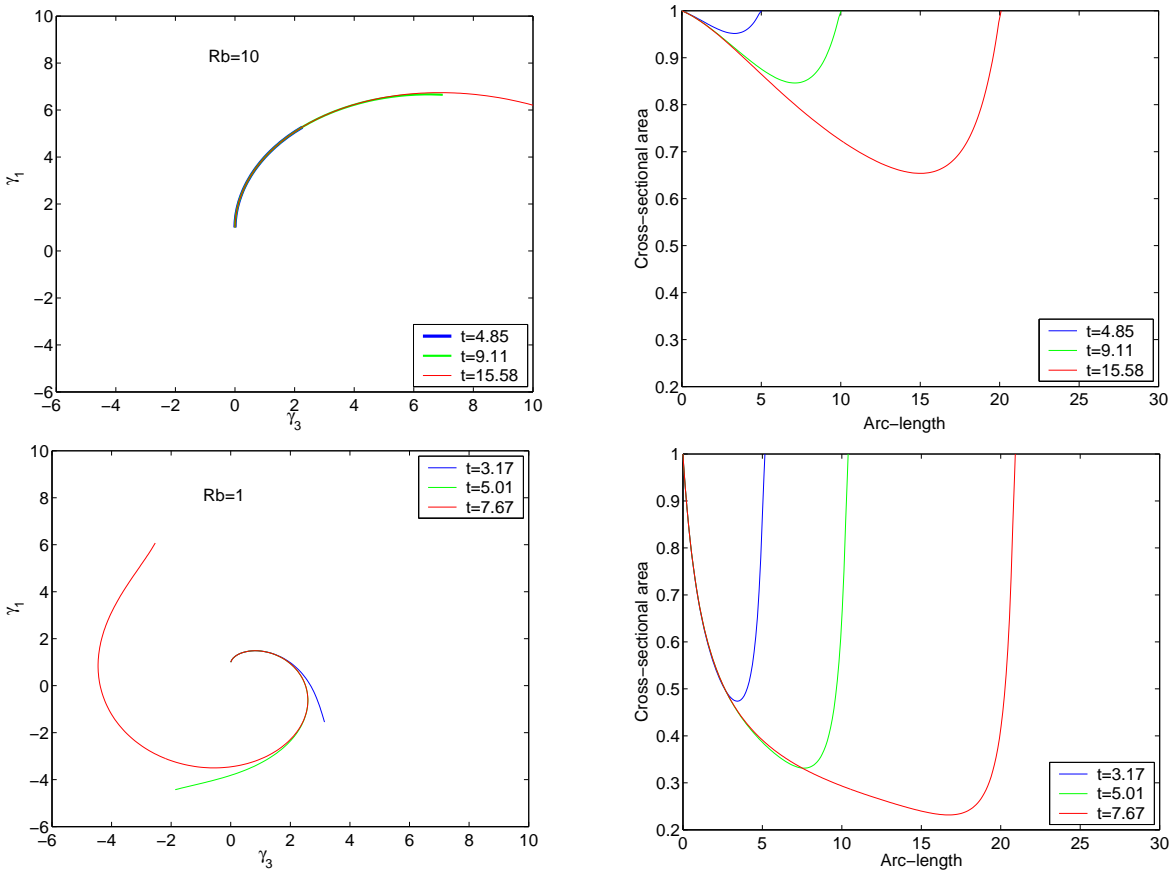


Figure 3.16: Evolution of the center-lines and cross-sectional areas. Top and bottom left panels: The center-line in the  $(\gamma_3, \gamma_1)$ -plane, Top and bottom right panels: Cross-sectional areas versus fiber arc-length. Top panel:  $Re = 4$  and  $Rb = 10$ , Bottom panel:  $Re = 4$  and  $Rb = 1$ .

By comparing the top and bottom left panels of Fig. 3.16, we see that when the Rossby

number decreases the center-line coils more rapidly. Furthermore, we notice that for large Rossby numbers the center-line dynamics does not change significantly in time. Similarly, the results of the comparison of the top and right panels of Fig. 3.16 show that with decreasing Rossby number, cross-sectional area also decreases faster with growing length of the fiber.

It is also interesting to analyze the differences between the profiles of the inviscid and viscous fibers. As it can be seen from Fig. 3.17 this difference is quite significant. The inviscid fiber goes away from the device whereas the viscous one stays nearer, and has a higher curvature.

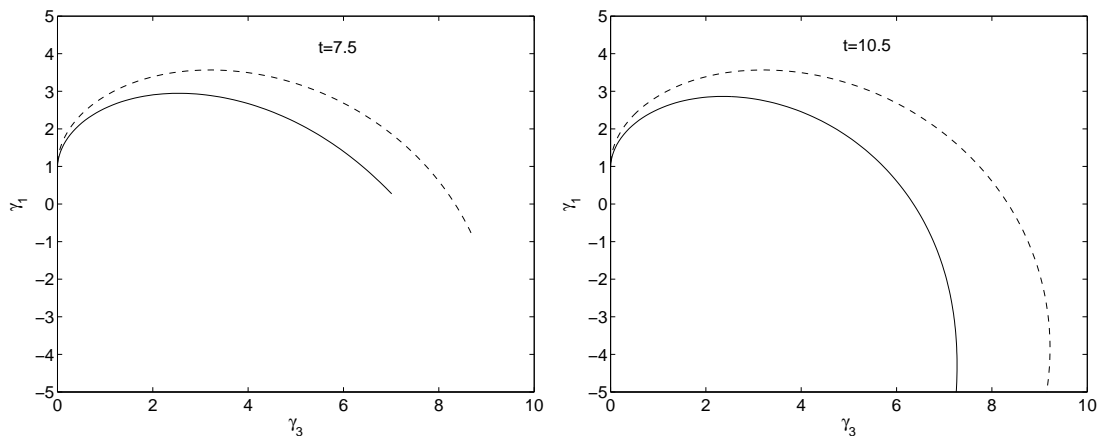


Figure 3.17: Evolution of viscous and inviscid fibers at two different times. The solid curves represent the center-line for  $Re = 1$ , the dashed curves for  $Re = \infty$ .

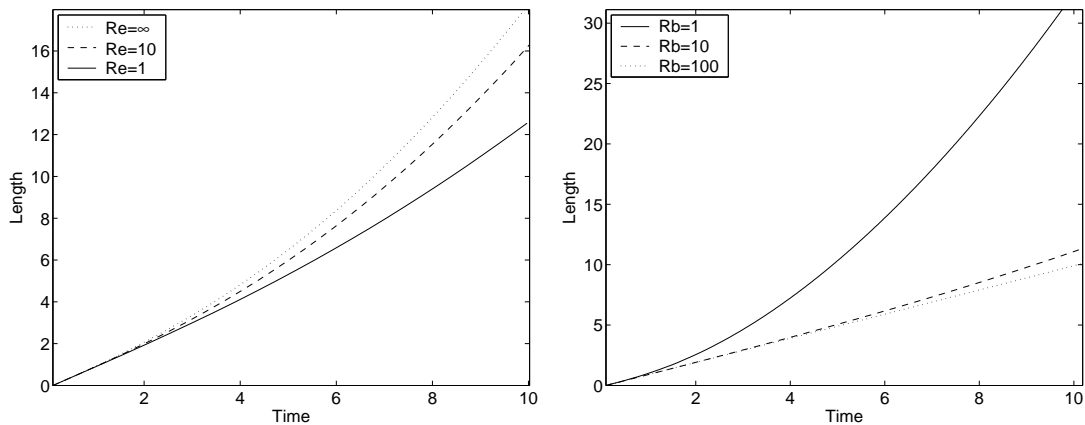


Figure 3.18: Effects of viscosity and rotation speed on the evolution of the fiber length. Left: Fiber length versus time for various Reynolds numbers at a fixed Rossby number  $Rb = 4$ . Right: Fiber length versus time for various Rossby numbers at a fixed Reynolds number  $Re = 4$ .

The effect of viscosity and rotation on evolution of the fiber length is described in Fig. 3.18. In the left panel of Fig. 3.18, the fiber length is plotted against time for

different values of Reynolds numbers, while the Rossby number is kept constant. In agreement with previous results, we see that fiber length increases more rapidly with increasing Reynolds numbers. The evolution of the fiber length in the inviscid limit is different from the viscous case for small Reynolds numbers only. However, it can be observed that the rotational speed also substantially influences the dynamics of the fiber length. In particular, a rapid increase for small Rossby numbers is evident in the right panel of Fig. 3.18.

### 3.4 Curved fiber (3D center-line)

The dynamics of the fiber center-line has been studied in Section 3.3 under the assumption that rotational forces are much stronger than gravity. However, there are situations where rotational forces are small or comparable to the gravitational force. In order to focus on a more general situation it is important to consider gravity. Therefore, in this section we additionally incorporate gravity into the problem.

To study the influence of rotational and gravitational forces on the center-line of the fiber we consider our full model Eqs. (3.1)-(3.8). More generally, with the inclusion of gravity into the problem, the center-line of the fiber lies no longer in a plane and as a consequence it is a three-dimensional vector, i.e.  $\boldsymbol{\gamma} = (\gamma_1, \gamma_2, \gamma_3)$ . Hence,  $\tilde{\mathbf{v}}$  is also a three-dimensional vector.

We follow the staggered approach as described in Section 3.3.1 for the discretization of Eqs. (3.1)-(3.4). However, due to the increase of the dimension of the center-line  $\boldsymbol{\gamma}$ , two angular functions  $\alpha$  and  $\beta$ , which are functions of both  $s$  and  $t$  are introduced. They define the tangent vector as

$$\partial_s \boldsymbol{\gamma} = (\partial_s \gamma_1, \partial_s \gamma_2, \partial_s \gamma_3) = (\sin(\alpha) \cos(\beta), \cos(\alpha), \sin(\alpha) \sin(\beta)) \quad (3.63)$$

with

$$\alpha(0, t) = \frac{\pi}{2} \quad \text{and} \quad \beta(0, t) = 0.$$

It can easily be seen that Eq. (3.63) automatically fulfills the constraint (3.4). Due to the introduction of the angle functions  $\alpha$  and  $\beta$ , the number of unknowns of the system is increased by two. Therefore, Eq. (3.63) is used to close the model equations. It should be pointed out that inclusion of the gravity does not introduce any problem in the discretization of the equations. Similar numerical procedures as described in Section 3.3.1 are applied. For this reason we do not repeat the details of these procedures. However, the results obtained by the numerical simulation are shown below.

### 3.4.1 Simulation results and discussion

The effect of rotational, viscous and gravitational forces on the fiber center-line and its cross-sectional area are described in the simulation results. The model parameters  $Re = 8$ ,  $Rb = 1$  and  $Fr = 2$  are considered for the simulation. Here, we have chosen these parameters of the same order to see the combined effects of all the forces.

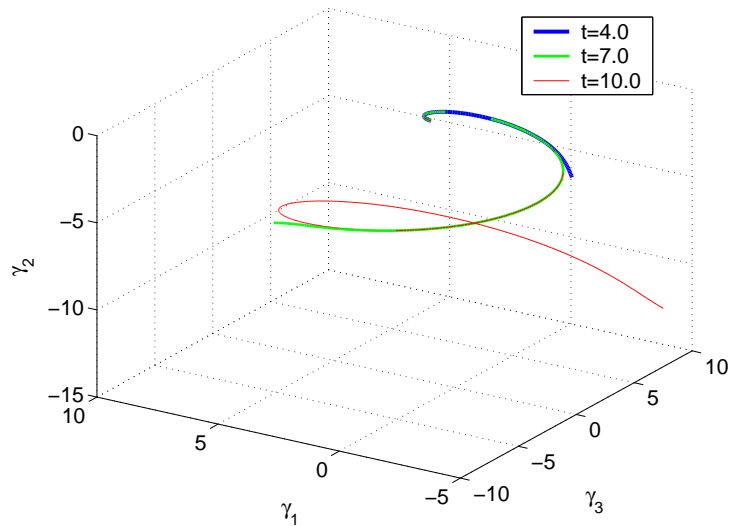


Figure 3.19: Evolution of the fiber center-line under the influence of rotational and gravitational forces.

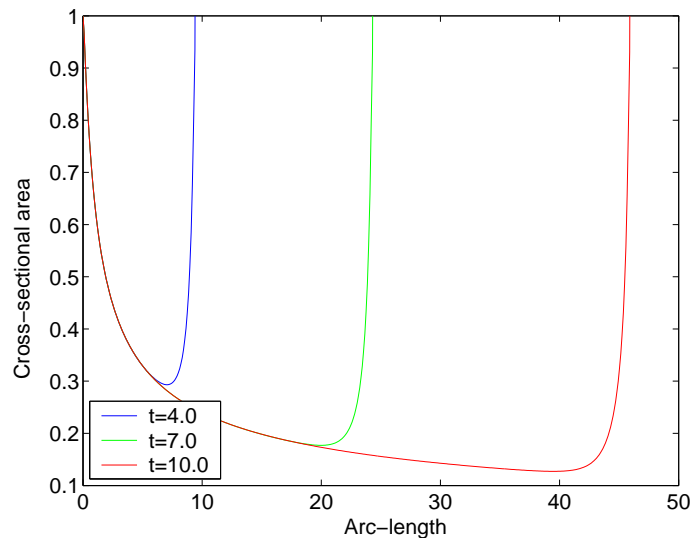


Figure 3.20: Cross-sectional area versus fiber arc-length at three different times.

Figure 3.19 shows the fiber center-line at various times. This figure clearly depicts the evolution of the viscous fiber under the influence of gravitational and rotational forces. We see that the fiber center-line forms a helical shape with growing time.

Due to the action of gravity it is falling down whereas the rotational forces curve the center-line. The cross-sectional area at three different times is shown in Fig. 3.20. The cross-sectional area is monotonically decreasing with increasing time.

The developed numerical scheme for the simulation of the fiber evolution process produces reasonable results. However, the numerical scheme has a certain limitation. In order to simulate the fiber model for small Rossby numbers, which are of order  $O(10^{-1})$  or less, experience reveals that a starting time at least two orders of magnitude less than the Rossby number is required. Moreover, for small Rossby numbers, the velocity increases very rapidly and the CFL criterion imposes even smaller time steps. Thus, the computational time is very high and it is difficult to perform a simulation even for a very small fiber length. For these reasons our scheme needs to be modified in future to include the case of smaller Rossby numbers.

### 3.5 Summary

In this chapter, we have analyzed the non-stationary fiber model. A finite volume code has been developed for the solution of the time dependent fiber problem. Simulation results are shown for a wide range of Reynolds, Rossby and Froude numbers. In particular, the simulation results are validated by comparing them against the analytical results of the inviscid problem.

Furthermore, the simulation results show that the length of the fiber increases with time but its center-line varies slowly. This leads to analyze the stationary situation of the fiber model in the following chapter of this thesis.

## Chapter 4

# Numerical Simulation of the Steady State Fiber Model

The evolution process of the fibers under the influence of viscous, rotational and gravitational forces has already been investigated in Chapter 3. The simulation results show that the length of the fiber varies with time but its trajectory varies slowly. Thus, the observation reveals that although the glass wool production process is inherently complex and time-dependent, in certain situations the process can be described as a stationary process.

In the stationary fiber problem the fiber center-line and the dependent variables like velocity, cross-sectional area, etc. as well as boundary conditions are independent of time. However, one can also simulate a time dependent fiber model for the generation of the fiber for a long time and then asymptotically reach steady-state with stationary boundary conditions. For the analysis of the steady-state we must consider a fiber of infinite length, which is unlike in reality, where the fiber breaks at a certain point and is thus limited to a finite length. Hence, only a part of the fiber needs to be considered for the discussion of the stationary problem. This means that the shape of the fiber and the dependent variables will be observed for a finite fiber length only.

In the light of the above discussion it is useful to study the steady-state fiber model. Such a model will be presented in the following section.

A brief outline of this chapter is as follows. In the first section we present the steady-state equations of the asymptotic model. Section 4.2 proposes a numerical scheme to solve the model equations. Moreover, the simulation results of the steady and unsteady process are compared. Furthermore, a projection approach is introduced in Section 4.3 to solve the problem even for very small Rossby numbers. Finally, a summary of the results is given in Section 4.4.

## 4.1 Steady state fiber model

We will work with the equations of the non-dimensional asymptotic model given in Section 2.7. Since we consider the time-independent problem, all variables depend only on the arc-length parameter  $s$ . We solve the system for  $s \in [0, L]$ , where  $L$  is considered to be a finite length of the fiber. After dropping the terms associated with the time derivative we get the following set of equations.

*Conservation of mass and momentum,  $s \in [0, L]$*

$$\partial_s(Au) = 0 \quad (4.1)$$

$$\partial_s(uA\tilde{\mathbf{v}}) = \frac{3}{\text{Re}}\partial_s(A\partial_s u\partial_s\boldsymbol{\gamma}) + \tilde{\mathbf{f}}A \quad (4.2)$$

*Coupling condition*

$$\tilde{\mathbf{v}} = u\partial_s\boldsymbol{\gamma} \quad (4.3)$$

*Arc-length parameterization*

$$\|\partial_s\boldsymbol{\gamma}\| = 1 \quad (4.4)$$

*Boundary conditions at the nozzle,  $s = 0$*

$$\begin{aligned} A(0) &= 1, & u(0) &= 1 \\ \boldsymbol{\gamma}(0) &= \boldsymbol{\gamma}_0, & \partial_s\boldsymbol{\gamma}(0) &= \boldsymbol{\tau}_0 \end{aligned} \quad (4.5)$$

*Boundary condition at  $s = L$*

$$\partial_s u(L) = 0 \quad (4.6)$$

The non-dimensional body forces are

$$\tilde{\mathbf{f}} = \frac{1}{\text{Fr}^2}\mathbf{e}_g - \frac{2}{\text{Rb}}(\mathbf{e}_\omega \times \tilde{\mathbf{v}}) - \frac{1}{\text{Rb}^2}(\mathbf{e}_\omega \times (\mathbf{e}_\omega \times \boldsymbol{\gamma})) \quad (4.7)$$

The symbols  $A$ ,  $u$  and  $\boldsymbol{\gamma}$  denote the cross-sectional area of the fiber, the fluid velocity and the center-line of the fiber, respectively. The body force  $\tilde{\mathbf{f}}$  include the force of gravity and the rotational forces. The dimensionless parameters in these equations are the Reynolds number  $\text{Re}$ , the Froude number  $\text{Fr}$  and the Rossby number  $\text{Rb}$ . The choice of scales and definitions of all non-dimensional parameters are already given in Chapter 2.

Following similar considerations as given in Section 3.1, the fiber position at the nozzle is equal to  $\boldsymbol{\gamma}_0 = (1, 0, 0)$ . For the tangent vector  $\boldsymbol{\tau}_0$ , we set  $\boldsymbol{\tau}_0 = (1, 0, 0)$ . Considering the simple setting for the rotating device as shown in Fig. 3.1, the vector  $\mathbf{e}_g$  and  $\mathbf{e}_\omega$  of Eq. (4.7) are equal to  $\mathbf{e}_g = (0, -1, 0)$  and  $\mathbf{e}_\omega = (0, 1, 0)$ . Further, by introducing the components of the vectors  $\boldsymbol{\gamma} = (\gamma_1, \gamma_2, \gamma_3)$  and  $\tilde{\mathbf{v}} = (\tilde{v}_1, \tilde{v}_2, \tilde{v}_3)$ , the outer force Eq. (4.7) can be rewritten as

$$\tilde{\mathbf{f}} = \left( -\frac{2}{\text{Rb}}\tilde{v}_3 + \frac{1}{\text{Rb}^2}\gamma_1, -\frac{1}{\text{Fr}^2}, \frac{2}{\text{Rb}}\tilde{v}_1 + \frac{1}{\text{Rb}^2}\gamma_3 \right). \quad (4.8)$$



**Remark 4.1** In the time-dependent fiber problem the so-called stress-free boundary condition is applied at the end of the fiber. But, in the steady case the end of the fiber is not known. However, the highest order derivative of the system Eqs. (4.1)-(4.4) is second order for the fluid velocity  $u$ . In addition to the boundary condition at the nozzle Eq. (4.5) an extra boundary condition is required to close the model equations. Therefore, this stress-free boundary condition Eq. (4.6) is again imposed at the given length of the fiber. Moreover, it should be noted that in the unsteady model, this boundary condition always produces a layer at the end of the cross-sectional area of the fiber, while this will not be observed in the steady model since the model equations will be solved for a given finite length of the fiber.

In the following section we present a numerical scheme for solving the steady-state fiber model. The following scheme is quite similar to the one developed in Section 3.3.1 for the unsteady problem.

## 4.2 Numerical procedure

Before we introduce the numerics, we first simplify the equations of the steady-state fiber model. Notice, that in the stationary situation we have only one velocity  $u$ . So writing the coupling condition explicitly has no meaning. It simply increases the number of unknowns of the system. Of course, one can consider  $\tilde{\mathbf{v}}$  as one of the unknowns of the problem, but for simplicity we eliminate  $\tilde{\mathbf{v}}$  from Eq. (4.2) in order to obtain ordinary differential equations for  $u$  and  $\boldsymbol{\gamma}$ . Furthermore, Eq. (4.1) provides constant mass flux along the fiber. By using Eq. (4.5), we get  $Au = 1$ . Therefore, we can write the equations either in terms of  $A$  or  $u$ . Here, we write then, in terms of  $u$ . Thus, the model now consists of the momentum and the constraint equation:

$$\partial_s(u\partial_s\boldsymbol{\gamma}) = \frac{3}{\text{Re}}\partial_s\left(\frac{1}{u}\partial_s u\partial_s\boldsymbol{\gamma}\right) + \tilde{\mathbf{f}}\frac{1}{u}, \quad (4.9)$$

and

$$\|\partial_s\boldsymbol{\gamma}\| = 1. \quad (4.10)$$

Indeed, it is helpful to simplify the above equations even further by introducing two angles  $\alpha$  and  $\beta$  as functions of the arc-length parameter  $s$  such that

$$(\partial_s\gamma_1, \partial_s\gamma_2, \partial_s\gamma_3) = (\sin(\alpha)\cos(\beta), \cos(\alpha), \sin(\alpha)\sin(\beta)) = \mathbf{e}_{\alpha,\beta}. \quad (4.11)$$

Moreover, at the nozzle  $s = 0$ , we have

$$\alpha(0) = \frac{\pi}{2} \quad \text{and} \quad \beta(0) = 0. \quad (4.12)$$

Eq. (4.12) is the consequence of Eq. (4.5).

Finally, substituting Eq. (4.11) into Eq. (4.9), we obtain

$$\partial_s(u\mathbf{e}_{\alpha,\beta}) = \frac{3}{\text{Re}}\partial_s\left(\frac{1}{u}(\partial_s u)\mathbf{e}_{\alpha,\beta}\right) + \tilde{\mathbf{f}}\frac{1}{u}, \quad (4.13)$$

The arc-length constraint Eq. (4.10) can be expressed as the following differential equation

$$\partial_s\boldsymbol{\gamma} = \mathbf{e}_{\alpha,\beta}. \quad (4.14)$$

Eqs. (4.13)-(4.14) are a simplified system of six equations for the six unknowns,  $u$ ,  $\alpha$ ,  $\beta$  and  $\boldsymbol{\gamma}$ . The momentum equation (4.13) is still in divergence form. Therefore, it is natural to discretize these equations by finite volumes. Moreover, we again use an up-winding differencing scheme to treat the convective term.

For the numerical solution of the unsteady fiber problem, a finite volume method has been used on a non-uniform staggered grid. For the present problem we consider a staggered grid of uniform cell lengths. Let us divide the length of the fiber into  $N$  fixed cells of equal length  $\Delta s$  as shown in Fig. 4.1. To approximate the model equations we average  $u$  and  $\mathbf{e}_{\alpha,\beta}$  over the cell  $[s_{i-1}, s_i]$ . The center-line  $\boldsymbol{\gamma}$  is approximated at the cell faces. Let  $u_i$  and  $(\mathbf{e}_{\alpha,\beta})_i$  denote the numerical approximation of the cell average solution in the control cell  $[s_{i-1}, s_i]$ , and let  $\boldsymbol{\gamma}_i$  be the approximation of  $\boldsymbol{\gamma}$  at the cell face  $s_i$ .

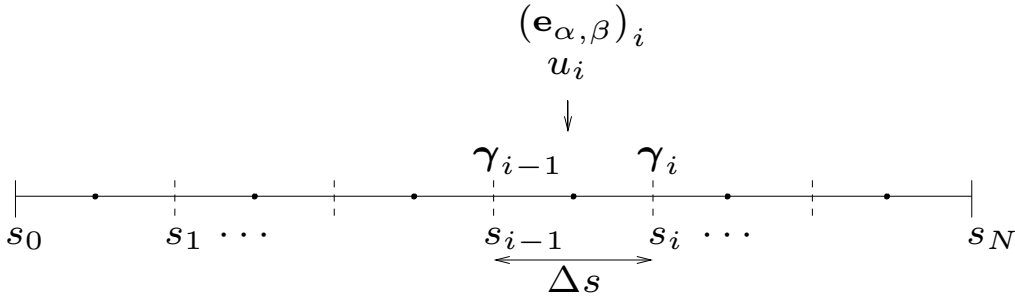


Figure 4.1: Grid type used for the steady-state model. Black dots and small vertical dashed lines represent nodes and cell faces.

By integrating the governing Eqs. (4.13)-(4.14) over the control cell  $[s_{i-1}, s_i]$ , we get the following discretized equations.

$$(u\mathbf{e}_{\alpha,\beta})_i - (u\mathbf{e}_{\alpha,\beta})_{i-1} = \mathbf{h}_i - \mathbf{h}_{i-1} + \Delta s \tilde{\mathbf{f}}_i \frac{1}{u_i}, \quad (4.15)$$

$$\boldsymbol{\gamma}_i - \boldsymbol{\gamma}_{i-1} = \Delta s (\mathbf{e}_{\alpha,\beta})_i, \quad (4.16)$$

where  $\mathbf{h}_i$  is given by

$$\mathbf{h}_i = \mathbf{h}(s_i) = \frac{3}{\text{Re}} \left( \frac{1}{u} \partial_s u \mathbf{e}_{\alpha,\beta} \right) (s_i),$$

with

$$\begin{aligned} u(s_i) &= \frac{u_i + u_{i+1}}{2}, \\ (\mathbf{e}_{\alpha,\beta})(s_i) &= \frac{(\mathbf{e}_{\alpha,\beta})_i + (\mathbf{e}_{\alpha,\beta})_{i+1}}{2}, \end{aligned}$$

and

$$(\partial_s u)(s_i) = \frac{u_{i+1} - u_i}{\Delta s}.$$

At the boundary nodes,  $i = 1$  and  $N$ , the function  $\mathbf{h}$  is approximated in a special way. Using the boundary condition Eq. (4.5), the approximation of  $\mathbf{h}$  at  $s_0$  is given by

$$\mathbf{h}_0 = \mathbf{h}(s_0) = \frac{3}{\text{Re}} \left( \frac{1}{u} \partial_s u \mathbf{e}_{\alpha,\beta} \right) (s_0)$$

with

$$u(s_0) = 1, \quad (\mathbf{e}_{\alpha,\beta})(s_0) = \boldsymbol{\tau}_0,$$

and

$$(\partial_s u)(s_0) = \frac{(u_1 - u_0)}{\frac{\Delta s}{2}}.$$

Similarly, by using Eq. (4.6), the approximation of  $\mathbf{h}$  at grid point  $s_N$  reads

$$\mathbf{h}_N = \mathbf{h}(s_N) = \mathbf{0}.$$

The approximation of the body force  $\tilde{\mathbf{f}}$  yields

$$\tilde{\mathbf{f}}_i = \left( -\frac{2}{\text{Rb}} u_i (e_{3,\alpha,\beta})_i + \frac{(\gamma_1)_{i-1} + (\gamma_1)_i}{2\text{Rb}^2}, -\frac{1}{\text{Fr}^2}, \frac{2}{\text{Rb}} u_i (e_{1,\alpha,\beta})_i + \frac{(\gamma_3)_{i-1} + (\gamma_3)_i}{2\text{Rb}^2} \right),$$

where  $e_{1,\alpha,\beta}$  and  $e_{3,\alpha,\beta}$  represent the first and third component of the vector  $\mathbf{e}_{\alpha,\beta}$ .

Now, we will look at methods available to solve the non-linear discretized Eqs. (4.15)-(4.16). These are  $6N$  equations for the  $6N$  variables,  $u_1, \dots, u_N, \alpha_1, \dots, \alpha_N, \beta_1, \dots, \beta_N$  and  $\gamma_1, \dots, \gamma_N$ .

For the numerical solution of the time dependent problem iterations based on the least-square method are used to achieve a solution through a sequence of steps from a starting state to a final converged state. For the solution of the steady-state problem a similar iteration method is used. Of course, the iteration steps resemble a dynamic process but do not correspond to a realistic time-dependent behavior. Here we will advance the solution by slowly increasing the viscosity of fluid and the speed of the rotating device. This type of procedure is also used in [21] in a different context to solve equations for an electrically forced jet. The details of the implementation are presented in Algorithm 4.1. The simulation results are discussed in the following subsection.

**Algorithm 4.1** The coupled non-linear Eqs. (4.15)-(4.16) are solved implicitly using a Newton or a modified Newton method [24]. The initial guess is given by a straight fiber of constant cross sectional area and uniform velocity. We then slowly increase the rotational speed and the viscosity of the fluid till we reach the desired rotation speed and viscosity. The previously calculated solution is used as the initial guess for the next step. Thus, the algorithm is the following:

**Initialize** the fiber as straight line with uniform cross-sectional area and velocity  
**repeat**  
    **Increase** linearly rotational speed and viscosity  
    **Solve** Eqs. (4.15)-(4.16) for velocity and fiber position  
    **Update** initial fiber position  
**until** the desired rotational speed and viscosity

**Remark 4.2** Although the equations of the stationary and non-stationary model are discretized by using a finite volume method, the nature of the systems is quite different. The governing equations of the time dependent model are a set of PDE with the arc-length constraint. On the other hand, the steady-state model Eqs. (4.13)- (4.14) are simply ODEs. Both the systems are closed with similar boundary conditions. In particular, the stress-free boundary condition produces a layer in the unsteady case, while this is not true in the steady model. Thus, the discretized system that arise from the steady model is less stiff in comparison to the unsteady one. Hence, the non-linear discrete equations are solved using a simple Newton or a modified Newton iterations scheme.

### 4.2.1 Comparison of the simulation results

In this section some comparisons of the numerical results of the steady and unsteady state are presented. We consider first the solution of the unsteady problem at a certain time  $t$ . Then the steady problem is solved over the length produced by the unsteady problem. For the comparison, we first start with a rather low viscosity of the fiber. Here, we consider  $Re = 8$ . The Rossby and Froude number are chosen to be  $Rb = 1$  and  $Fr = 2$ . The unsteady solution is considered at the non-dimensional time  $t = 10$ .

A comparison of the fiber center-lines is given in Fig. 4.2. The steady center-line shown in this figure seems to be quite close to the unsteady one. Fig. 4.3 displays a similar comparison for the cross-sectional area of the fiber. This figure shows that both simulation results agree quite well. The difference at the end is produced by the mentioned boundary layer.

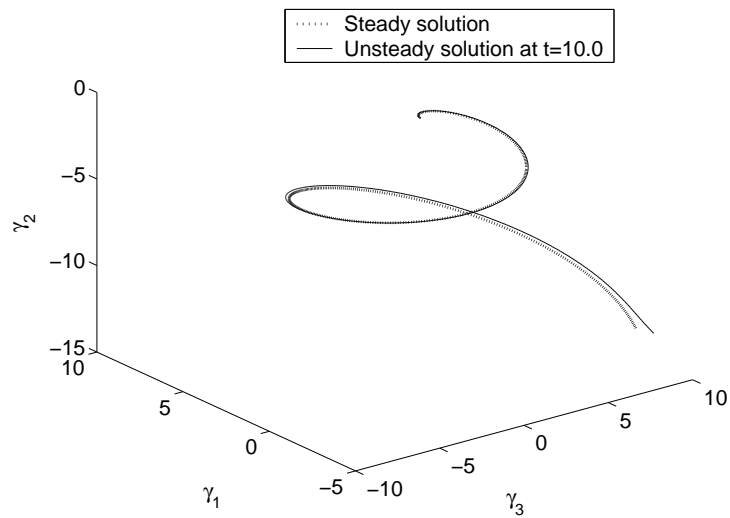


Figure 4.2: Comparison of the fiber center-line in the steady and unsteady case for the parameters  $Re = 8$ ,  $Rb = 1$  and  $Fr = 2$ . The dashed curve represents the unsteady fiber, while the dotted curve corresponds to the steady solution.

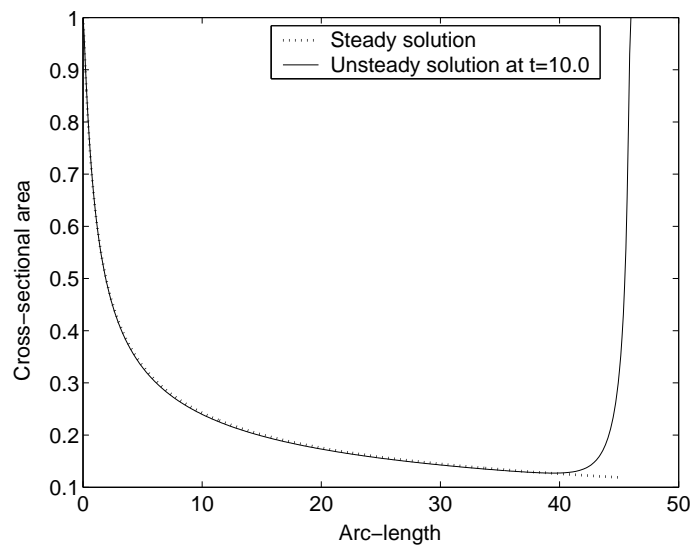


Figure 4.3: Comparison of the cross-sectional area of the fiber in the steady and unsteady case for the parameters  $Re = 8$ ,  $Rb = 1$  and  $Fr = 2$ . The dashed curve represents the cross-sectional area of the unsteady fiber, while the dotted curve corresponds to the steady solution.

The results compared above for a fiber with low viscosity illustrates that the unsteady process may be regarded as a stationary process. It is also interesting to see how the results differ for a more viscous fiber. Hence, we choose again  $Rb = 1$  and  $Fr = 2$  but decrease now the Reynolds number to  $Re = 3$ . The comparison of the results with respect to the fiber center-line and cross-sectional area are shown in Figs. 4.4-4.5.

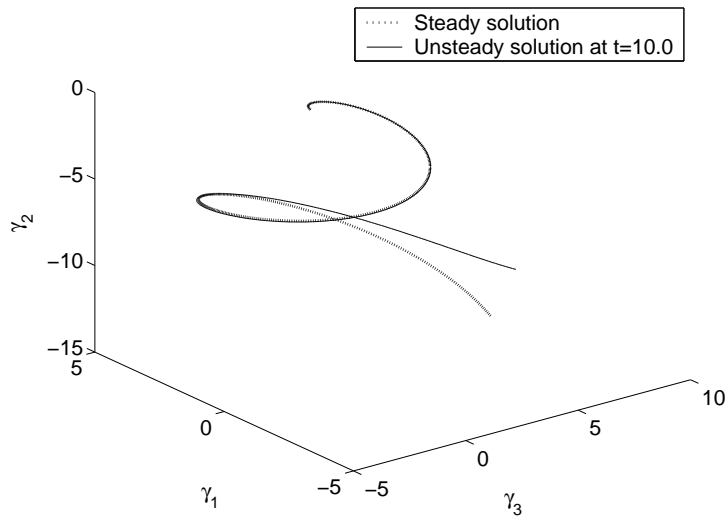


Figure 4.4: Comparison of the fiber center-line in the steady (dotted) and unsteady (dashed) simulation for the parameters  $Re = 3$ ,  $Rb = 1$  and  $Fr = 2$ .

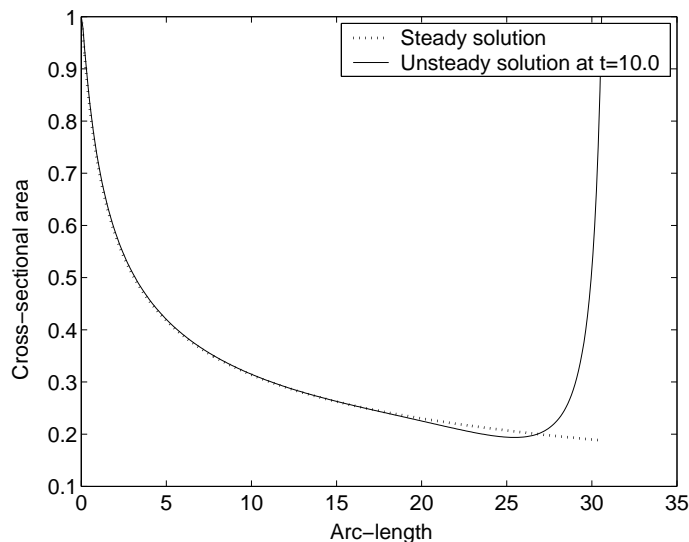


Figure 4.5: Comparison of the cross-sectional area of the fiber in the steady (dotted) and unsteady (dashed) simulation for the parameters  $Re = 3$ ,  $Rb = 1$  and  $Fr = 2$ .

The comparisons show that the change in the cross-sectional area at the end of the fiber is very small but the difference at the end of the center-line is quite significant. In this case, the fluid in the fiber is more viscous due to decrease of the Reynolds number. As we see from Fig. 4.3 and Fig. 4.5 the fiber arc-length decreases as the Reynolds number decreases and the boundary layer at the end of the cross-sectional area is slightly smear out, while this is sharp in the low viscous case. The differences at the end of the fiber are also produced by the boundary layer. However, the comparison agrees quite well up to a long distance from the nozzle.

In principle a similar comparison can be made for unsteady and steady solutions for different Rossby numbers while keeping Reynolds and Froude numbers constant. However, from the unsteady results, (see top and bottom left panels of Figs. 3.16), it can be concluded that the change of the fiber trajectory is small. Thus, with respect to the underlying assumptions the process can be described as a stationary process.

The numerical scheme introduced in Section 4.2 to solve the equations of the steady-state fiber model is producing reasonable results. In particular, the results are validated by comparisons with the numerical results of the unsteady model. However, the scheme has a certain limitation. The convergence is slow and it does not even converge for the small Rossby numbers. This problem has also been pointed out in the time-dependent numerical scheme. We try to solve this problem in the following section by projecting the model equations to local coordinates.

### 4.3 Projection approach

The model Eqs. (4.1)-(4.7) are described in a Cartesian coordinate system. We have observed that the model equations in this system are not well suited for numerics, especially for small values of the non-dimensional parameters. To overcome this problem we first project the model equations onto a local system of tangential and normal coordinates. The resulting equations are then solved numerically. In order to define the projection, we first introduce the basis vectors of the local coordinate system.

We first define the tangent vector

$$\mathbf{e}_t(\alpha, \beta) = \partial_s \boldsymbol{\gamma} = (\sin(\alpha) \cos(\beta), \cos(\alpha), \sin(\alpha) \sin(\beta)).$$

Now, the derivative of  $\mathbf{e}_t(\alpha, \beta)$  with respect to the arc-length parameter  $s$  can be written as

$$\partial_s \mathbf{e}_t(\alpha, \beta) = (\partial_s \alpha) \mathbf{e}_n(\alpha, \beta) + (\sin(\alpha) \partial_s \beta) \mathbf{e}_b(\alpha, \beta),$$

where the vectors  $\mathbf{e}_n$  and  $\mathbf{e}_b$  are given by

$$\begin{aligned}\mathbf{e}_n(\alpha, \beta) &= (\cos(\alpha) \cos(\beta), -\sin(\alpha), \cos(\alpha) \sin(\beta)) \\ \mathbf{e}_b(\alpha, \beta) &= (-\sin(\beta), 0, \cos(\beta)).\end{aligned}$$

Indeed, it can be easily verified that the vectors  $\mathbf{e}_t$ ,  $\mathbf{e}_n$  and  $\mathbf{e}_b$  are orthonormal and they express basis vectors of the local coordinate system.

After some simplification, the momentum Eq. (4.9) can be written in terms of the local coordinate components. They are:

$$\partial_s u = \frac{3}{\text{Re}} \partial_s \left( \frac{\partial_s u}{u} \right) + \frac{1}{u} \left( \frac{\sin(\alpha)}{\text{Rb}^2} (\gamma_1 \cos(\beta) + \gamma_3 \sin(\beta)) - \frac{1}{\text{Fr}^2} \cos(\alpha) \right) \quad (4.17)$$

$$u \partial_s \alpha = \frac{3}{\text{Re}} \left( \frac{\partial_s u}{u} \right) \partial_s \alpha + \frac{1}{u} \left( \frac{\cos(\alpha)}{\text{Rb}^2} (\gamma_1 \cos(\beta) + \gamma_3 \sin(\beta)) + \frac{1}{\text{Fr}^2} \sin(\alpha) \right) \quad (4.18)$$

$$\begin{aligned}u \sin(\alpha) \partial_s \beta &= \frac{3}{\text{Re}} \left( \frac{\partial_s u}{u} \right) \sin(\alpha) \partial_s \beta + \\ &\quad \frac{1}{u} \left( \frac{1}{\text{Rb}^2} (-\gamma_1 \sin(\beta) + \gamma_3 \cos(\beta)) + \frac{2}{\text{Rb}} u \sin(\alpha) \right).\end{aligned} \quad (4.19)$$

The constraint Eq. (4.10) can be expressed as

$$\begin{aligned}\partial_s \gamma_1 &= \sin(\alpha) \cos(\beta) \\ \partial_s \gamma_2 &= \cos(\alpha) \\ \partial_s \gamma_3 &= \sin(\alpha) \sin(\beta).\end{aligned} \quad (4.20)$$

The boundary conditions are the same as in Eqs. (4.5)-(4.6), with  $\alpha(0) = \pi/2$  and  $\beta(0) = 0$ . Eqs. (4.17)-(4.20) are ordinary differential equations for the unknowns  $u$ ,  $\alpha$ ,  $\beta$ ,  $\gamma_1$ ,  $\gamma_2$  and  $\gamma_3$ .

We now see that the divergence form of Eq. (4.9) is lost by projecting onto local coordinates. Therefore, the finite volume method may not be appropriate for the discretization of the resulting equations. For the numerical treatment, we discretized these equations using a finite difference method. Moreover, we approximate the second derivative (dissipative term in Eq. (4.17)) with a three-point central difference scheme. For the first derivative we use a backward difference method. The non-linear algebraic problem arising from the discretization of Eqs. (4.17)-(4.20) is solved implicitly using a Newton method. The numerical implementation follows similar steps as outlined in Algorithm 4.1. Although stability analysis of the numerical scheme is not discussed here, the simulations reveal that this scheme is more stable and predicts the results even in a few iterations for small Rossby numbers. Simulation results for Rossby, Reynolds and Froude numbers are presented in Chapter 5 to illustrate the performance of this scheme.



## 4.4 Summary

The steady-state fiber problem is analyzed for a fiber of finite length. A numerical scheme based on a finite volume method is developed. A comparison of results from the unsteady and steady-state model yields that the transient behavior in the unsteady case is quite similar to the steady one. Observing the convergence problem in the finite volume code for small Rossby numbers, a projection approach is presented for suitable numerical solutions by means of a finite difference method.



# Chapter 5

## Application

### 5.1 Introduction

The present chapter focuses on the application of the asymptotic model derived in Chapter 2 to describe the flow of a incompressible Newtonian fluid in the glass wool production process. During the production process, hot molten material from a furnace is transferred into a rotating device, and fibers are produced as centrifugal forces extrude the material through many small holes. More details of the production process have already been explained in Chapter 1. A typical diagram of the process is also shown in Fig. 1.1.

Although the process is non-isothermal and involves numerous physical properties, we have limited ourselves in the derivation of the model to the isothermal situations. The physical effects of surface tension and aerodynamics forces are not considered in the model. The analysis of the model is also restricted to the first phase of the production process, during which the glass fibers emerge from the spinner. So any subsequent breaking of the fibers, while falling down to the conveyor, is not discussed in this thesis. However, the physical effects of inertia, viscosity, gravity and rotation are included in the fiber model. The model describes the dynamics of the fiber center-line as well as the internal variables of the fiber, e.g. cross-sectional area, velocity and tension. Moreover, with the underlying considerations, the non-stationary process can be regarded as a stationary one, as explained in Chapter 4. Hence, the steady-state version of the model is used to predict the shape of the fiber center-line and its internal variables via simulation based on industrial data provided by the Fraunhofer ITWM, Kaiserslautern.

## 5.2 Industrial data

The material used for the simulation is glass. The properties of the glass and the process parameters are tabulated below.

Parameter	Notation	Unit	Value
Density	$\rho$	$kg\ m^{-3}$	2500
Dynamic viscosity	$\mu$	$N\ s\ m^{-2}$	100
Radius of the drum	$L_0$	$m$	0.1
Radius of the nozzle	$a$	$m$	0.0001
Drum rotation rate	$\omega$	$rad\ s^{-1}$	100
Fiber exit velocity	$V$	$m\ s^{-1}$	0.01

Table 5.1: Typical process parameters.

By considering the typical length of the fiber as the radius of the rotating device ( $L_0$ ), and gravity  $g = 10\ m\ s^{-2}$ , the non-dimensional numbers are calculated and given below.

Non-dimensional numbers	Value
$Re = (\rho V L_0) / \mu$	0.025
$Rb = V / (\omega L_0)$	0.001
$Fr = V / (\sqrt{g L_0})$	0.01

Table 5.2: Non-dimensional numbers.

### A note on industrial data

By reasons of confidentiality, the tabulated data are slightly modified one but within the range of real industrial production process. In fact the viscosity of the material may not be constant, but depends upon temperature. Since we assume the temperature distribution along the length of the fiber is constant, the value of viscosity is calculated at a given high temperature.

### Observation

By Eq. (2.19) the value of the slenderness parameter  $\epsilon$  turns out to be of order  $O(10^{-3})$ . Thus, the glass wool production process described above fits to the setting of the asymptotic approximation of the Navier-Stokes equation with its free surface boundary conditions. Further, the orders of magnitude of the non-dimensional parameters in the problem are:  $Re \sim O(10^{-1})$ ,  $Rb \sim O(10^{-3})$  and  $Fr \sim O(10^{-2})$ . This

indicates that the centrifugal force, that is of order of magnitude  $O(1/Rb^2) \sim (10^{+6})$ , is dominant over the viscous, coriolis and gravitational forces which are of orders  $O(1/Re) \sim (10^{+1})$ ,  $O(1/Rb) \sim (10^{+3})$  and  $O(1/Fr^2) \sim (10^{+4})$ , respectively. Due to the observed orders of magnitudes of forces one can guess that fiber movements are dominated by the centrifugal force. This observation is demonstrated graphically below.

### 5.3 Simulation results

Considering the simple setting for the rotating device as shown in Fig. 3.1, the steady-state model described by the projection approach given in Sec. 4.3 is solved. The simulation results of the shape of the center-line, cross-sectional area, velocity and the tension on the fiber are shown in Figs. 5.1-5.5. In the real production process the length of the wool fibers are very small within the range 0.03 to 0.04 meters. Hence, for the computational purpose a part of the fiber of length 0.035 meters is considered.

The steady center-line is shown in Fig. 5.1. The length scale of the axes is in meters. From this figure we see that the scale of the  $\gamma_2$  and  $\gamma_3$  coordinates are of orders  $O(10^{-8})$  and  $O(10^{-3})$ , respectively. This implies that gravity and coriolis forces have very little effect on the formation of the fibers. To see it more clearly, a projection of the three-dimensional center-line is plotted in Fig. 5.2 onto the  $(\gamma_3, \gamma_1)$ -plane.

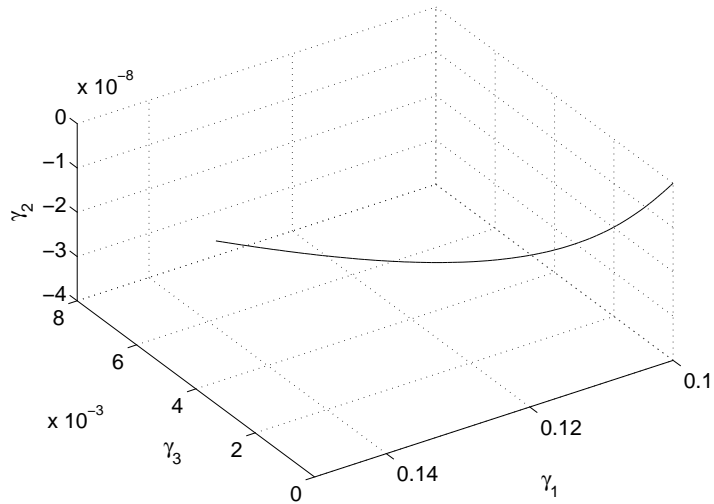


Figure 5.1: Steady-state center-line profile.

Fig. 5.2 shows that the fiber is nearly straight. Thus, the above observation is fairly in good agreement with the numerical results. In particular, this results confirms the validity of the industrial application of the straight fiber model given in Section 3.2.3.

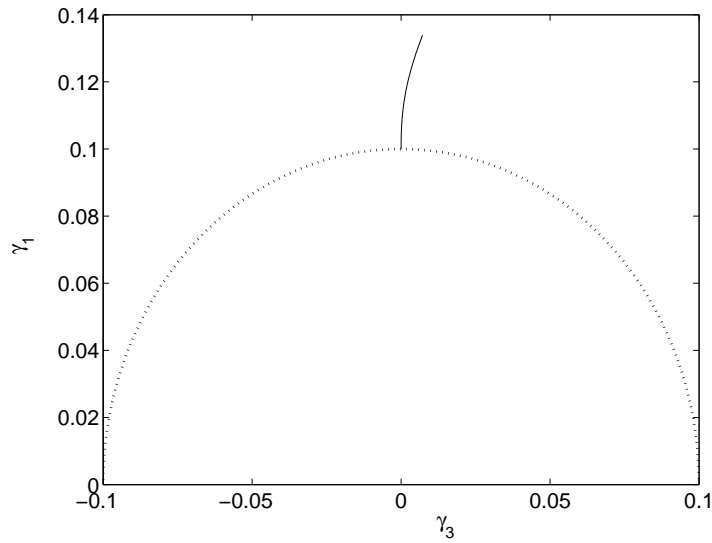


Figure 5.2: Projection of the plot given in Fig. 5.1 in the  $(\gamma_3, \gamma_1)$ -plane. The dotted line shows half of the rotating device. The solid line represents the center-line of the fiber.

The maximum decrease of the cross-sectional area as shown in Fig. 5.3 takes place near the nozzle. Then it stays almost constant. The maximum decrease of cross-sectional area results in a maximum increase of velocity as we can see in Fig. 5.4.

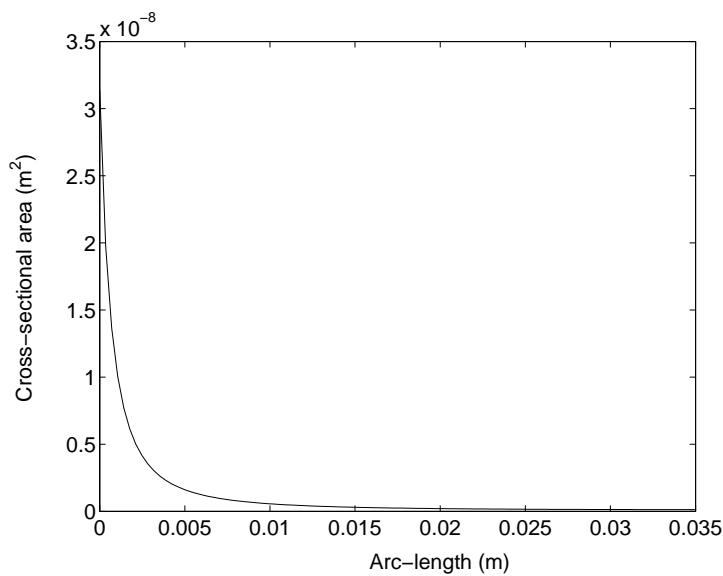


Figure 5.3: Cross-sectional area versus arc-length along the fiber.

Due to high rotational speed of the device the fluid accelerates rapidly after it comes out of the nozzle. As a result, the velocity gradient is maximum at the nozzle position and the tension on the fiber is highest at that point (see Fig. 5.5). The tension then

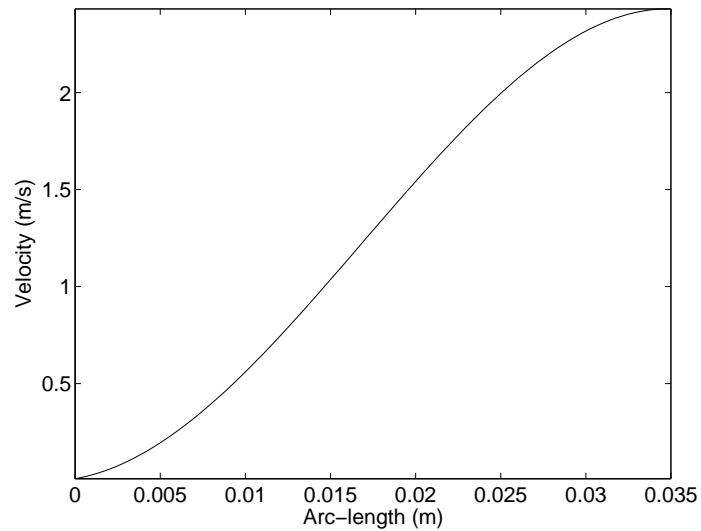


Figure 5.4: Velocity versus arc-length along the fiber.

decreases faster to a very small value with growing distance from the nozzle. Finally, at the end of the fiber the tension is zero due to the stress-free condition.

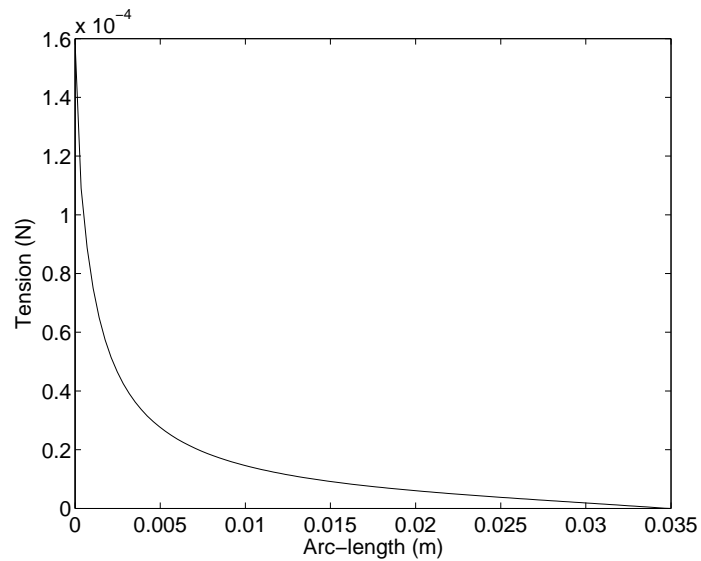


Figure 5.5: Tension versus arc-length along the fiber.

The computational results show that the derived model has the ability to predict the expected behavior of the fiber. Moreover, the projection approach to the steady-state model appears to produce quite good results. A test of the accuracy of the numerical results needs further works, like inclusion of temperature and aerodynamic force into the model.





# Chapter 6

## Conclusions

In the present thesis, a dynamic model for a single viscous fiber emerging from a rotating device under the influence of inertia, viscous, gravity and rotational forces has been developed. The underlying physical behavior of such a fiber is described by the incompressible Navier-Stokes equations in combination with free surface boundary conditions. An asymptotic analysis with respect to the thickness of the fiber leads to a simple one-dimensional model with that it is relatively easy to analyze the steady and dynamical behavior of the problem.

The derivation of the numerical schemes for the unsteady and steady state fiber model by finite volume method and their simulations for a wide range of parameters including realistic parameters based on industrial data have provided a deeper understanding of the mechanism involved in this process. However, a number of extensions can be made in future works investigating questions like stability, consistency and convergency of the schemes.

The derived model provides a basis for the mathematical description of the fiber spinning process. It will hopefully play a helpful role in the optimization of current industrial fiber production. It can be further extended by incorporating the temperature, surface tension and aerodynamic effects. Although glass wool production is the main focus of this thesis, the derived asymptotic model and the developed finite volume code are applicable to a wide range of problems concerning slender Newtonian fluids driven by gravity and centrifugal forces.



# APPENDIX

## Notations

Throughout this thesis we have denoted scalar-valued quantities by normal size letters ( $p$ ), vectors by lower-case bold face symbols ( $\mathbf{v}$ ) and second order tensors by bold face upper-case symbols ( $\mathbf{S}$ ). Furthermore, some of the used notations are listed below.

### Variables and coordinates

$t$	time variable
$s$	arc-length parameter
$\rho$	density
$\mu$	coefficient of viscosity
$\sigma$	coefficient of surface tension
$p$	pressure
$u$	intrinsic velocity
$\omega$	speed of the rotating device
$w$	speed of the free surface
$\kappa$	curvature
$\varkappa$	mean curvature
$\lambda$	torsion
$\epsilon$	slenderness paramter
$A$	cross-sectional area
$V$	mean velocity
$L_0$	characteristic length
$L$	fiber length
$R$	radius function
$\mathbf{r}$	space coordinates
$\mathbf{x} = (x_1, x_2, s)$	scaled curvilinear coordinates
$\mathbf{v}$	velocity
$\mathbf{f}$	body forces
$\check{\mathbf{r}}$	coordinate transformation map
$\check{\mathbf{x}}$	inverse of $\check{\mathbf{r}}$
$\gamma$	center-line
$\boldsymbol{\tau}$	tangent vector
$\boldsymbol{\eta}$	normal vector

<b>b</b>	binormal vector
<b>S</b>	stress tensor
<b>I</b>	identity tensor
<b>F</b>	coordinate transformation matrix
<b>G</b>	inverse of <b>F</b>
<i>J</i>	determinant of <b>F</b>

### Set and spaces

$\mathbb{R}^+$	set of positive real numbers
$\emptyset$	empty set
$\Omega$	fiber domain
$\Gamma_{fr}$	free surface of the fiber
$\Gamma_{in}$	inflow domain
$\Gamma_{lat}$	lateral surface of the fiber
<b>Lin</b>	set of linear transformation
$\mathcal{C}^1$	space of 1-times continuous differentiable function

### Non-dimensional parameters

Re	Reynolds number
Fr	Froude number
Rb	Rossby number

### Operators and functions

$d/dt$	total derivative with respect to time $t$
$\partial_t$	partial derivative with respect to time $t$
$\partial_s$	partial derivative with respect to arc-length parameter $s$
$\mathbf{A}^T$	transpose of the matrix <b>A</b>
$\text{tr}(\mathbf{A})$	trace of <b>A</b>
$\det(\mathbf{F})$	determinant of <b>F</b>
$\ \cdot\ $	Euclidean norm
$ \cdot $	measure of a set
$\nabla$	gradient operator

### Mathematical symbols

The following mathematical notations used in Chapter 2 are based on Einstein summation convention. The notations are mostly chosen according to [1]. Latin indices such as  $i$ ,  $j$  and  $k$  take the values from 1 to 3.

$$\begin{array}{llll}
 \mathbf{a} \cdot \mathbf{b} & = & a_i b_i & (\mathbf{a} \otimes \mathbf{b})_{ij} & = & a_i b_j \\
 (\nabla \mathbf{a})_{ij} & = & \partial_i a_j & (\nabla \cdot \mathbf{a}) & = & \partial_i a_i \\
 (\nabla \mathbf{A})_{ijk} & = & \partial_i A_{jk} & (\nabla \cdot \mathbf{A})_{ij} & = & \partial_i A_{ij} \\
 (\mathbf{A} : \mathbf{B}) & = & \text{tr}(\mathbf{A} \cdot \mathbf{B}^T) & (\mathbf{a} \cdot \mathbf{A})_k & = & a_i A_{ik} = (\mathbf{A}^T \cdot \mathbf{a})_i
 \end{array}$$

# Bibliography

- [1] S. S. ANTMAN. *Nonlinear Problems of Elasticity*. Springer-Verlag, 1995.
- [2] S. E. BECHTEL, J. Z. CAO, and M. G. FOREST. Practical application of a higher order perturbation theory for slender viscoelastic jets and fibers. *Jr. Non. Fluid. Mech.*, 41:201–273, 1992.
- [3] R. L. BISHOP. There is more than one way to frame a curve. *Amer. Math. Month.*, 82(3):246–251, 1975.
- [4] J. D. BUCKMASTER and A. NACHMAN. The buckling and stretching of viscida ii- effects of surface tension. *Qrartly Jr. of Mech. and Appl. Math.*, 31:157–168, 1978.
- [5] J. D. BUCKMASTER, A. NACHMAN, and L. TING. The buckling and stretching of viscida. *Jr. Fluid. Mech.*, 69:1–20, 1975.
- [6] L. J. CUMMINGS and P. D. HOWELL. On the evolution of non-axisymmetric viscous fibres with surface tension inertia and gravity. *Jr. Fluid. Mech.*, 389:361–389, 1999.
- [7] S. P. DECENT, A. KING, and I. M. WALLWORK. Free jets spun from a prilling tower. *Journal of Eng. Mathematics*, 42:265–282, 2002.
- [8] S. P. DECENT, M. SIMMONS, E. PARAU, D. WONG, A. KING, and L. PARTRIDGE. Liquid jets from a rotating orifice. In *Proceedings of the 5th International Conference on Multiphase Flow, ICMF' 04*, Yokohama, Japan, May 2004.
- [9] J. DEWYNNE, J. R. OCKENDON, and P. WILMOTT. On a mathematical model for fiber tapering. *SIAM Jr. APP. MATH.*, 49(4):983–990, 1989.
- [10] J. N. DEWYNNE, P. D. HOWELL, and P. WILMOTT. Slender viscous fibers with inertia and gravity. *Qrartly Jr. of Mech. and Appl. Math.*, 47:541–555, 1994.

- 
- [11] J. N. DEWYNNE, J. R. OCKENDON, and P. WILMOTT. A systematic derivation of the leading-order equations for extensional flows in slender geometries. *Jr. Fluid. Mech.*, 244:323–338, 1992.
- [12] F. DIAS and J. M. VANDEN-BROECK. Flows emerging from a nozzle and falling under gravity. *Jr. Fluid. Mech.*, 213:465–477, 1990.
- [13] M. P. DO CARMO. *Differential Geometry of Curves and Surfaces*. Prentice-Hall, 1976.
- [14] J. EGGERS. Nonlinear dynamics and breakup of free surface flows. *Rev. Mod. Phy.*, 69(3), 1997.
- [15] V. M. ENTOV and A. L. YARIN. The dynamics of thin liquid jets in air. *Jr. Fluid. Mech.*, 140:91–111, 1984.
- [16] M. FEISTAUER. *Mathematical Methods in Fluid Dynamics*. Longman Scientific and Technical, 1993.
- [17] C. A. J. FLETCHER. *Computational Techniques for Fluid Dynamics VOL II*. Springer-Verlag, 1988.
- [18] M. G. FOREST and H. ZHOU. Unsteady analyses of thermal glass fibre drawing process. *Euro. Jr. of Applied Mathematics*, 12:479–496, 2001.
- [19] F. T. GEYLING and G. M. HOMSY. Extensional instabilities of the glass fiber drawing process. *Glass Technology*, 21(2):95–102, 1980.
- [20] M. E. GURTIN. *An Introduction to Continuum Mechanics*. Academic Press, 1981.
- [21] M. M. HOHMAN, M. SHIN, G. RUTLEDGE, and M. P. BRENNER. Electrospinning and electrically forced jets. ii. applications. *Physics of Fluids*, 13(8):2221–2236, 2001.
- [22] P. D. HOWELL. *Extensional Thin Layer Flows*. PhD thesis, St. Catherine’s College, Oxford, 1994.
- [23] S. KASE and T. MATSUO. Studies on melt spinning. i.fundamental equations on the dynamics of meltspining. *Journal of Polymer Science: PART A*, 3:2541–2554, 1965.
- [24] D. KINCAID and C. WARD. *Numerical Analysis: Mathematics of Scientific Computing*. Brooks Cole, 1996.
- [25] R. J. LEVEQUE. *Finite Volume Methods for Hyperbolic Problems*. Cambridge University Press, 2002.

- 
- [26] H. LUO and T. R. BEWELY. On the contravariant form of the navier-stokes equations in time-dependent curvilinear coordinates system. *Jr. Comput. Phys.*, 199:695–701, 2004.
- [27] M. A. MATOVICH and J. R. A. PEARSON. Spinning a molten threadline. *I. and E. C. Fundamentals*, 8(3):512–520, 1969.
- [28] Y. T. SHAH and J. R. A. PEARSON. On the stability of non isothermal fiber spinning. *Ind. Eng. Chem. Fundam.*, 11(2):145–149, 1972.
- [29] J. H. SPURK. *Fluid Mechanics*. Springer-Verlag, 1997.
- [30] Y. M. STOKES and E. O. TUCK. The role of inertia in extensional fall of a viscous drop. *Jr. Fluid. Mech.*, 498:205–225, 2004.
- [31] Y. M. STOKES, E. O. TUCK, and L. W. SCHWARTZ. Extensional fall of a very viscous fluid drop. *Qrartly Jr. of Mech. and Appl. Math.*, 53(4):565–582, 2000.
- [32] F. R. S. TROUTON. On the coefficient of viscous traction and its relation to that of viscosity. *Proc. Roy. Soc.*, A77:426–440, 1906.
- [33] J. M. VANDEN-BROECK and J. B. KELLER. Jets rising and falling under gravity. *Jr. Fluid. Mech.*, 124:335–345, 1982.
- [34] H. K. VERSTEEG and W. MALALASEKERA. *In Introduction to Computational Fluid dynamics: The Finite Volume Method*. Longman, 1995.
- [35] I. M. WALLWORK, S. P. DECENT, A. C. KING, and R. M. S. M. SCHULKES. The trajectory and stability of a spiralling liquid jet. part 1. inviscid theory. *Jr. Fluid. Mech.*, 459:43–65, 2002.
- [36] Z. U. A. WARSI. Conservation form of the Navier-Stokes equations in general non-steady coordinates. *AIAA Journal*, 19(2):40–42, 1980.





CURRICULUM VITAE  
**Satyananda Panda**

- 02.05.1969            Born in Mahulpara, Orissa, India
- Jun. 1973  
—May 1980            Mahulpara primary and middle school
- Jun. 1980  
—May 1983            Mahulpara secondary school
- Jul. 1983  
—Jun. 1988            Bachelor studies at the government college, Bhawanipatna
- Jul. 1988  
—Aug. 1990            Master studies at the university of Sambalpur, School of  
Mathematical Sciences
- Sep. 1992  
—May 2000            Junior Lecturer in Mathematics, Vikram Deb college, Jey-  
pore, Orissa.
- Oct. 2000  
—Sep. 2002            Master studies in the programme Mathematics Interna-  
tional with specialization in Industrial Mathematics at  
the Technical University of Kaiserslautern, Department of  
Mathematics
- Jan. 2003  
—Mar. 2006            Doctorate studies at the Technical University of Kaiser-  
slautern, Department of Mathematics